6-1-2016

Layered double hydroxides-biopolymer nanocomposites for the controlled delivery of vitamins

Raghda El-Said El-Dessouky

The American University in Cairo

School of Sciences and Engineering

Layered Double Hydroxides-Biopolymer Nanocomposites for the Controlled Delivery of Vitamins

A thesis submitted in partial fulfillment of the requirements for the degree of
Master of Science in Chemistry

By Raghda El-Said El-Dessouky

Under the supervision of
Prof. Adham Ramadan

Spring 2016

The American University in Cairo

Layered Double Hydroxides-Biopolymer Nanocomposites for the Controlled Delivery of Vitamins

A Thesis submitted by

Raghda El-Said El-Dessouky

To the Chemistry Graduate Program

Spring 2016

A thesis submitted in partial fulfillment of the requirements for the degree of

Master of Science in Chemistry

Thesis Committee Supervisor /Chair: Dr. Adham R. Ramadan

Affiliation: Professor of Chemistry and Dean of Graduate Studies, the American University in Cairo.

Thesis External Examiner: Dr. Omaima N. El Gazayerly

Affiliation: Professor of the Pharmaceutics and Industrial Pharmacy Department, Faculty of Pharmacy, Cairo University.

Thesis Internal Examiner: Dr. Mayyada El Sayed.

Affiliation: Assistant Professor of Chemistry, Chemistry Department, School of Sciences and Engineering, the American University in Cairo.

Thesis Committee Moderator: Dr. Michael Kontominas

Affiliation: Professor and Director of the Chemistry Graduate Program, Chemistry Department, School of Sciences and Engineering, the American University in Cairo.

Program Director	Date	Dean	Date

ABSTRACT

In this investigation, vitamin B6- and folic acid-intercalated zinc-aluminum layered double hydroxides ($Zn^{2+}/Al^{3+} = 3$), were successfully prepared by coprecipitation (B6-LDH and Fa-LDH, respectively). Both vitamin-intercalated LDHs were characterized by XRD and FTIR analyses and compared to control pristine LDHs synthesized following the same method. The XRD analysis confirmed the structural crystallinity of the synthesized LDHs, which are typical of hydrotalcite-like materials, and confirmed the intercalation of both vitamins through the observed expansion in the LDH interlayer spacing. The FTIR analysis confirmed the presence of the vitamins in the LDH layers by observing the peaks pertaining to the vitamin-specific functional groups. The shifts of some of the peaks in the vitamin-loaded LDH from their positions in the pure vitamin's spectrum were attributed to the existence of host-guest interactions between the vitamin and the brucite-like sheets. Such interactions are mostly hydrogen bonding and van der Waals interactions for vitamin B6, as it is expectedly intercalated in neutral form. Whereas, for folic acid, electrostatic forces are also present, since it is intercalated in its anionic form. The loading percentages were calculated to be 31.5% (w/w) for B6-LDH and 65% (w/w) for Fa-LDH. Both vitamin-intercalated LDHs were entrapped in calcium alginate matrix by the ionotropic gelation of 2.5% (w/v) sodium alginate solution comprising dispersed LDHs, in a 5% (w/v) $CaCl_2$ solution. The gelation process produced regular spherical beads. The beads were prepared at three alginate:LDH ratios for both vitamins, which are 16:1, 10:1 and 4:1 (in order of increasing LDH content). These were labeled: B6-A/L16, B6-A/L10 and B6-A/L4 for vitamin B6 and Fa-A/L16, Fa-A/L10 and Fa-A/L4 for folic acid. The entrapment efficiency of the composite beads was evaluated indirectly by measuring the concentration of the vitamin leached in the $CaCl_2$ solution post-gelation using UV spectroscopy. It was found that the increase in the LDH content was associated with higher entrapment efficiency of the composite beads for the vitamins, as they act as reservoirs protecting the vitamin from diffusing into the alginate matrix and leaching into the gelling solution during the curing time. XRD plots of the vitamin-loaded composite beads do not exhibit any crystalline features belonging to either the vitamin or the LDHs. The LDHs were possibly mostly de-laminated during their dispersion and gelation with alginate. The FTIR analysis of the vitamin-loaded beads was inconclusive due to the overlap of the peaks from the different components in the composite systems. The FTIR analysis of the control composite beads (A/L16, A/L10 and A/L4) and plain calcium alginate beads (A0) demonstrates the presence of the alginate-specific peaks, and the increase in the LDH-related features as the LDH content per bead increases. The broadening of the peaks belonging to the LDH's lattice vibrations and the sharpening of the carboxylate stretching vibrations peak were attributed to the possible existence of polymer-clay interactions. Nitrogen sorption analysis of the control composite beads, the plain calcium alginate beads and the pristine LDHs characterized the texture of such materials as mesoporous. The BJH desorption average pore diameter of the pristine LDH is 18.19 nm.

The increase in the LDH content per bead was found to be associated with a general decrease in porosity. The BJH desorption average pore diameter was found to decrease from 7.03 nm in A/L16 to 5.30 nm in A/L4. The decrease in pore diameter as LDH content increases in the composite beads is attributed to the possibility that the cationic LDH layers play a role in cross-linking the alginate polymer chains along with Ca^{2+} ions during gelation. The swelling behavior of the vitamin-loaded beads was investigated in Biorelevant simulated intestinal fluid of pH 6.5 under the same conditions used for the *in-vitro* release experiment. The vitamin-loaded beads were swollen appreciably and the LDH content was shown to have an influence on the swelling trend: the increase in the LDH content was associated with a decrease in the degree of bead swelling. It was proposed that such trend is due to the engagement of the cationic brucite-like sheets in a crosslinking reaction with alginate's ionized carboxylate groups screening their repulsive forces and reducing their swelling. The *in-vitro* release studies were conducted so as to simulate the passage of the vitamin-loaded composite beads along the gastrointestinal tract: 2 hours in Biorelevant simulated gastric fluid (BioSGF, pH 1.6) followed by 24 hours in Biorelevant simulated intestinal fluid (BioSIF, pH 6.5). Both vitamin-loaded composite beads exhibited a substantial improvement in their stability on exposure to the acidic conditions of BioSGF, when compared to the vitamin-intercalated LDHs alone. The release profiles of the B6-loaded composite beads in BioSGF showed that increasing the LDH content per bead was associated with an increase in the relative release with time. This was attributed to the proneness of the LDHs in such beads to acid attack and their subsequent weathering, being more accessible than those comprising higher alginate content. In BioSIF, the situation was reversed, and it was shown that the release was mainly governed by the degree of bead swelling, being the least for the beads with the highest LDH content. Another factor that possibly played a role is the increased tortuosity in the composites comprising higher density of LDHs per bead. The release profiles of the folic acid-loaded composite beads in BioSGF showed that increasing the LDH content per bead was associated with a decrease in the relative release with time. Unlike B6, folic acid being less soluble in the acidic medium, its dissolution becomes the limiting factor, and the release of the dissolved folate ions becomes dominated by their diffusivity in the alginate matrix. The LDH layers endow the matrix with barrier properties, and the bulky folate ions have to adopt longer and more tortuous pathways in order to be released, explaining the reduced relative release with time as the LDH content increases per bead. In BioSIF, the beads of the highest LDH content show the highest relative release with time, owing to the repulsive forces between the ionized folate and alginate's carboxylates in basic conditions, which are more pronounced in the high LDH content (and thus folate) beads. We believe that samples B6-A/L16 and Fa-A/L4 show the most promising features of efficient oral controlled-release drug delivery systems, with satisfactory sustained release properties.

Acknowledgements

Having come as far as finalizing my research work and submitting my thesis, marks one of the most astounding milestones in my entire life. This wonderful journey would not have been possible if it were not for my husband Amgad, who encouraged me to join the program in the first place and has always had faith in me. I am truly grateful for having him in my life, surrounded by his sincere love and support. There are not enough words in this world to express my whole-hearted appreciation and gratitude for my dear parents. I would have never been what I am and where I am today if it were not for their unconditional love, support and prayers. I owe them a lot and I hope that I can always make them proud. I am also thankful to my lovely sister Dalia, and to my dear grandparents for their love and sincere prayers. It is a blessing to have them in my life.

One of the main reasons that my experience at the AUC turned out to be an exceptional one, is having had Dr. Adham Ramadan as a teacher and an advisor. I am quite fortunate to have learnt the basics of nanotechnology from him, and I am extremely grateful and proud that he accepted me as one of the students in his research team. It is not everyday that one finds a professor in his knowledge and stature who is as passionate about science and education, and is willing to dedicate all his time and effort for the benefit of his mentees. I am truly honored to have worked under the supervision of such a great person and I hope I have made him proud.

I would like to thank Dr. Nahed Yacoub for her great effort conducting the nitrogen-sorption analysis and for her continuous willingness to share her knowledge whenever needed.

I would also like to express my sincere gratitude and appreciation to the people who made my experience on campus the best and the smoothest it can be. Many thanks to Ms. Hoda Saad, who always made sure to provide the support and information needed in all matters. I am very thankful to Mr. Victor, for his efforts to always make available all the resources I needed to complete my work. I am sincerely grateful to the best team of lab specialists there can be. Ahmed Omaya, for being such a great big brother, always providing his full support and selfless efforts in all aspects of my research work. Mr. Emad Farag, for his great dedication to ensure the execution of my samples in a timely manner. Mr. Mahmoud Abdel-Moez, for his tremendous efforts and dedication, and being the backbone of the chemistry department labs.

Last but not least, I would like to express my deepest gratitude and appreciation to my dear friends and lab colleagues who showered me with their love and all kinds of support throughout my master's journey. Special thanks to my dear friend Nada, who has put me on track at the beginning of my lab work, and has given me a great friendship that is for life. I would also like to thank Marwa for her tremendous help and guidance, and Zahraa for her great work on LDHs that has paved the way for us to follow through.

List of Abbreviations

5ASA	5- aminosalicylic acid
BET theory	Brunauer, Emmett, and Teller theory
BioSGF	Biorelevant Simulated Gastric Fluid
BioSIF	Biorelevant Simulated Intestinal Fluid
BJH method	Barrett, Joyner, and Halenda method
CMC	Carboxymethyl Cellulose
CR-DDS	Controlled-release drug delivery system
EE	Entrapment Efficiency
FaSSIF, FeSSIF & FaSSGF	Fasted and Fed State Simulated Intestinal and Stomach Fluids
FTIR	Fourier transform infrared spectroscopy
HTlc	Hydrotalcite-like compounds
IUPAC	International Union of Pure and Applied Chemistry
LDHs	Layered double hydroxides
MMT	Montmorillonite
NSAIDs	Non-steroidal anti-inflammatory drugs
PLGA	poly(DL-lactide-co-glycolide)
PSD	Pore size distribution
SA	Sodium Alginate
SEM	Scanning Electron Microscopy
UV/Vis	Ultraviolet/visible spectroscopy
XRD	X-ray diffraction

Table of Contents

List of Figures

List of tables

Chapter 1. Introduction

1.1 Bionanocomposites and Controlled Release Drug Delivery Systems (CR-DDSs)

Research in pharmaceutical technology has been mainly focused on the development of state-of-the-art drug carriers that can maximize the efficiency, safety and convenience of therapy for patients. Despite being considered as the most popular and extensively used route of administration, oral delivery of drugs is challenged by problems such as poor bioavailability, dose dumping, fluctuating drug levels in the blood, premature enzymatic degradation, and the need for frequent dosing, which compromises patient compliance [1-3]. In order to tackle such challenges, novel strategies based on knowledge from multiple disciplines have been used to improve the oral drug delivery properties of conventional dosage forms, by the development of controlled-release drug delivery systems (CR-DDSs). These are based on platforms that host the drug through various types of interactions, depending on their physicochemical nature, enabling the modulation of drug release inside the body. Such systems are designed so as to release the drug at a predetermined rate (e.g. delayed-release and/or sustained-release), aiming to maintain its dose within the therapeutic window at the site of absorption/action for the desired period of time. CR-DDSs offer superior therapeutic efficiency, minimal side effects and improved patient compliance relative to conventional drug dosage forms [4, 5].

A wide range of platforms were investigated for their applicability as efficient drug carriers. Nanomaterial-based platforms were proven to show extraordinary promise in that area owing to their unique properties. They have a high surface area-to-volume ratio, which maximizes their drug loading capacities, their interaction with the surrounding environment, and their surface reactivity allowing for their functionalization with cell-targeting moieties. When contained in a nano-sized carrier, the drug's solubility is enhanced and its release behavior can be regulated. Nanostructures were found to manage to penetrate successfully and generously into tissues. They are uptaken by cells via endocytosis, such uptake mechanism was discovered to be around 15-250 times of higher efficiency than the uptake of micro-structures in the size range of 1-10 μm: an advantage that translates to improved bioavailability [1, 6, 7].

Layered double hydroxides (LDHs) -also referred to as hydrotalcite-like materials or anionic clays- comprise an emerging class of inorganic host-guest layered nanostructures that have been recently investigated and utilized for many applications. Unlike most inorganic nanomaterials that need pre-treatment to allow for their biological use and for drug loading, LDHs are biocompatible and possess structural features that allow for direct drug loading, enhanced cellular uptake and controlled release [2, 8]. Their interlayer region serves as a nano-vessel that can host drug molecules, maintaining their integrity and protecting them from their external environment. The arrangement of drug molecules in the LDH's interlayer space is the key to their controlled release properties. When inside the body, the drug is

released by 'de-intercalation' from the LDH layers via exchange with the anions present in the biological fluids in a controlled manner [9]. LDHs have basic properties, and they undergo dissolution in acidic media at pH < 4. When administered orally, their fast dissolution in the stomach releases the intercalated drug in a soluble absorbable form and thus improves its bioavailability, which is quite useful especially in the cases of poorly soluble drugs [10]. LDHs possess high specific surface area, which allows for high drug loading capacities. Moreover, their surface can be easily functionalized with cell-targeting moieties for targeted drug delivery. LDHs are biocompatible: their positively charged layers facilitate their cellular uptake, they exhibit low cytotoxicity and posses viscoelastic features that render them similar to gastric mucin and hence may protect the mucosal membrane by mimicking the protective role of gastric mucus. Many of the LDH component metal cations are vital minerals, such as Zn^{2+}, Mg^{2+} and Ca^{2+}: a fortunate coincidence that offers an extra benefit and motivation for their use as CR-DDSs [2, 11-15].

The use of LDHs as oral drug delivery vehicles is challenged by their basic nature, as they will dissolve in the stomach's environment (pH ~ 1.2), making the utilization of their benefit in controlling drug release quite inefficient for intestinally absorbed drugs [10]. Overcoming this problem can be achieved by dispersing LDHs in an acid-stable biopolymeric matrix, which can slow down/alleviate their decomposition in the stomach's environment. Alginate, a natural polysaccharide, is an excellent candidate for this purpose. Alginate has a hydrogel-forming ability: when dropped into an aqueous solution of multivalent cations, easily handled hydrogel beads are formed. In addition to its biocompatibility, biodegradability, mucoadhesive properties and low cost, alginate is a pH-sensitive hydrogel: it shrinks in acidic media and swells in neutral and basic ones. Such a property makes it ideal for the delivery of intestinally absorbed drugs, as it would minimize their release while in the stomach, but as the pH increases distally along the gastrointestinal tract, it swells and releases its cargo. Its mucoadhesive properties serve to localize the drug-of-interest at its absorptive surface, improving its bioavailability, in addition to protecting the gastro-mucosal wall from drug-induced irritation [16]. Moreover, on swelling, alginate hydrogels form a hydrocolloidal layer, of which high viscosity serves as a diffusion barrier that slows down the release of the loaded drug: a property that is exploited for the purpose of controlling drug release [17]. However, there are two main disadvantages associated with using plain alginate polymer beads as drug-delivery matrices: the leaching of the drug through the pores of the alginate beads during the gelling process, subsequently reducing the drug entrapment efficiency, and the fast breakdown of the polymeric matrix on exposure to a basic medium (e.g. intestinal medium) leading to undesired burst release of the drug. Combining an inorganic material such as LDH with a biopolymer such as alginate in a bionanocomposite should circumvent the limitations of each component on its own. Polymer-clay nanocomposites were shown to exhibit improved mechanical, physicochemical and drug-release control properties. Such improved properties can be harnessed in favor of the development of successful CR-DDSs [16, 18-23].

1.2 Layered Double Hydroxides (LDHs)

1.2.1 Structure and characterization

The term 'layered double hydroxides' (LDHs) refers to a class of natural and synthetic compounds that belongs to the wide family of 'anionic clays'. LDHs are structurally and chemically relevant to the mineral hydrotalcite, a hydroxycarbonate of magnesium and aluminum $[Mg_6Al_2(OH)_{16}]^{2+}.CO_3^{2-}.4H_2O$, and thus are interchangeably referred to as hydrotalcite-like compounds (HTlc). The basic structure of LDHs can be described through the structure of the mineral brucite $Mg(OH)_2$. In brucite, each Mg^{2+} cation is coordinated to six hydroxyl groups in an octahedral arrangement. Multiple octahedral units share edges forming infinite sheets that stack upon one another, resulting in brucite's three-dimensional structure. LDHs are based on a brucite-like framework, except that a fraction of the divalent metal cations (M^{II}) in each layer is replaced with isomorphous trivalent metal cations (M^{III}), thus imparting a positive charge on the brucite-like sheets. The whole structure is neutralized by the incorporation of anionic species in between the cationic sheets along with water molecules, each serves to hold together and stabilize the layered framework through electrostatic interactions and hydrogen bonding, respectively [24-26].

The crystal structure of each brucite-like sheet can be described in terms of a hexagonally close-packed configuration of hydroxyl groups, with the metal cations situated within their octahedral holes. The planes of hydroxyl anions can stack upon one another in different symmetries giving rise to various polytype structures. Most synthetic LDHs belong to the rhombohedral 3R polytype, in which each unit cell comprises three layers of brucite-like sheets. The unit cell is described by its lattice parameters *a* and *c*, where *a* is the nearest intralayer cation-cation (M-M) distance (which is the same as that between same-side O atoms of the hydroxyl groups) and *c* is a multiple of the basal spacing between two layers (denoted as *d*). In the 3R polytype, $c = 3d$ [2, 24, 27]. The basic structure of LDH is depicted in figure 1-1.

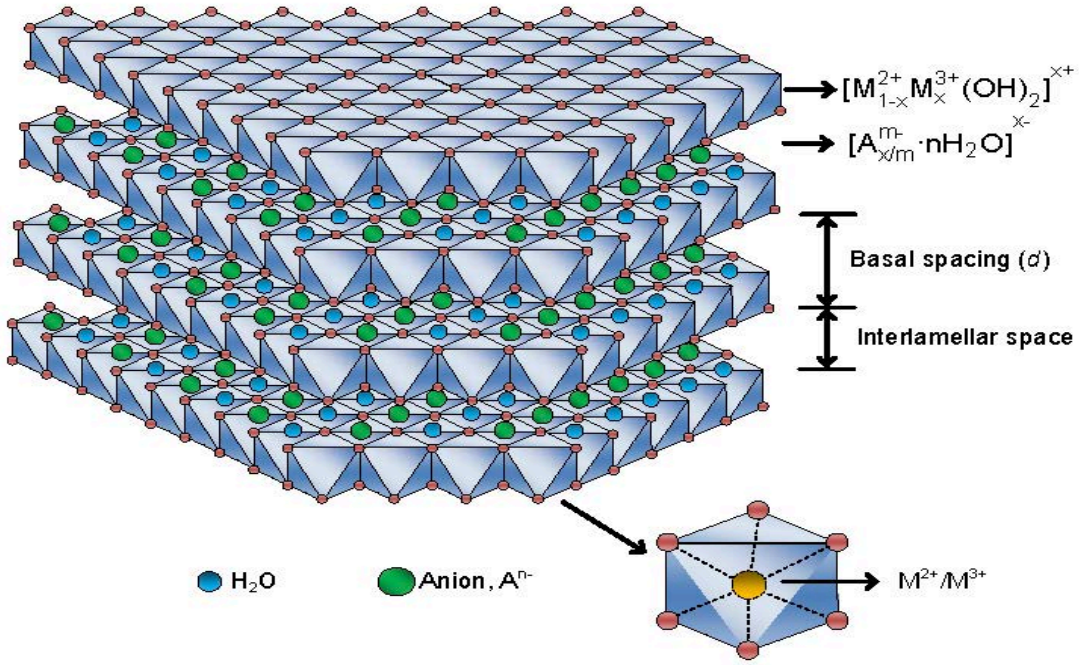

Figure 1-1. Schematic representation of the LDH structure [28].

The general chemical formula for most LDH compounds is:

$$\left[\boldsymbol{M^{II}_{1-x}\,M^{III}_{x}\,(OH)_2}\right]^{x+}\,[\boldsymbol{A^{m-}}]_{\boldsymbol{x/m}}\cdot\boldsymbol{nH_2O}$$

x is the trivalent metal mole fraction ($x = M^{III}/M^{II} + M^{III}$), A is the anionic species with charge m, and n is the number of moles of interlayer water molecules [26].

A range of M^{II} and M^{III} ions can be accommodated in the brucite-like sheets. This is basically dictated by the comparability of their ionic radii to that of Mg^{2+} ions and by the magnitude of the difference between the M^{II} and M^{III} ionic radii. As shown in the LDH general formula, the value of x determines the charge of the brucite-like sheets and thus affects the concentration and distribution of the interlayer anions and water molecules (which mostly fill the sites unoccupied by the anions). As long as they do not extract the metal cations from the hydroxylated sheets and possess sufficient charge density, a great variety of both organic and inorganic anions can be intercalated in LDHs. A complex network of hydrogen bonding exists between the polarized hydroxyl groups of the brucite-like sheets (especially those bonded to M^{III}) and interlayer anions and water molecules. Such bonds are in a continuous flux state rendering the distribution of interlayer species quite disordered. The size, charge, number and orientation of intercalated anions determine the interlayer distance [24, 25, 29, 30].

1.2.2 Synthesis methods

Numerous simple and inexpensive techniques were developed for the successful synthesis of LDHs on both laboratory and industrial scales. Generally speaking, the main approaches to the preparation of LDHs are either based on direct synthesis of the layered structure by the nucleation and growth of the hydroxide layers in the presence of the desired metal cations and anions, or post-synthesis treatments that tailor the desired LDH composition and structural features. The most commonly used techniques are coprecipitation, ion exchange and reconstruction.

1.2.2.a Coprecipitation

The term coprecipitation designates the simultaneous precipitation of both divalent and trivalent metal hydroxides from an aqueous precursor mixture of the metal salts containing the desired anions. The *x* value of the final product is determined by adjusting the molar ratio of the M^{II} and M^{III} ions in the precursor metal cations mixture. In order to achieve simultaneous precipitation, the reaction must take place at supersaturation conditions, which are mostly reached by controlling the pH using an alkali (most commonly sodium hydroxide and/or sodium bicarbonate). It is essential to carry out the reaction at a *constant* pH that is equal to or higher than that at which the more soluble hydroxide precipitates. Table 1-1 shows the pH values for the precipitation and re-dissolution of common M^{II} and M^{III} hydroxides used in LDHs [31].

Table 1-1. The pH values of precipitation and re-dissolution of common metal hydroxides used in LDHs [31].

Cation	Precipitation pH		Re-dissolution pH
	At 10^{-2} M	At 10^{-4} M	
Al^{3+}	3.9	8.0	9-12
Zn^{2+}	6.5	8.0	14
Cr^{3+}	5.0	9.5	12.5
Fe^{2+}	7.5	9.0	-
Mn^{2+}	8.5	10.0	-
Ni^{2+}	7.0	8.5	-
Co^{2+}	7.5	9.0	-
Cu^{2+}	5.0	6.5	-

The mechanism of coprecipitation is based on the condensation of hexa-aquo coordination complexes into brucite-like layers, comprising a uniform distribution of the cations and incorporating the interlayer solvated anions. A wide range of anions can be intercalated into LDHs through coprecipitation. The key for successful intercalation is for the desired anionic

species to have higher affinity and be present in excess as compared to the counter-ion in the precursor salt. It is necessary to perform the reaction under carbon dioxide-strict conditions when the desired anionic species is not carbonate ions, which have a relatively strong affinity to the hydroxylated layers and would compete for intercalation with the desired anion. A range of experimental parameters directly affects the degree of crystallinity of the final product. These include pH, temperature, concentrations of both the metal cations and alkaline solution, the flow rate of the reactants, and precipitate ageing. Less controllable parameters such as the hydrodynamics of the reaction medium affected by the stirring mechanism and the reactor's geometry, and electrolyte accumulation in the medium can also affect the coprecipitation process and hence the success of intercalation and the degree of product crystallinity [24, 25, 32, 33].

Coprecipitation can take place at either high or low supersaturation conditions. The setup for a low supersaturation coprecipitation process involves the slow and steady addition of the metal salts precursor mixture and the alkaline species into a reactor containing a vigorously stirred solution of the desired anionic species. The alkali flow rate is adjusted so as to maintain a constant pH value, either by manual monitoring or automatic titration. Nitrate and chloride salts are commonly used due to their relatively low affinity toward LDHs. On the other hand, a high supersaturation coprecipitation process involves the quick addition of the metal salts precursors mixture to a reactor containing both the alkali and the desired anion solution. This method has two main problems: it involves a high rate of nucleation and thus produces less crystalline LDHs, and the rather continuous change in pH during the reaction results in the formation of impurities of $M(OH)_2$ or $M(OH)_3$. Post coprecipitation, a thermal treatment process may be performed in order to raise the product yield and/or improve the crystallinity of poorly crystallized LDHs [24, 25, 32, 33].

1.2.2.b Anion exchange

In the anion exchange method, preformed LDHs with a weakly intercalated anion (e.g. nitrate or chloride ions) are stirred with a solution containing an excess of the desired anion. An exchange process takes place, where the guest anion replaces the already intercalated one. The anion exchange process is described by the following equation:

$$\mathbf{LDH.A^{m-} + X^{n-} \rightarrow LDH.(X^{n-})_{m/n} + A^{m-}}$$

A number of factors affect the extent of anion exchange. These include the affinity of the LDH for the incoming anion, the exchange environment, and the chemical composition of the layers. The affinity of guest anions to the positive hydroxylated sheets is determined by their charge and ionic radii: the smaller the ionic radius and the higher the charge, the stronger the affinity to LDHs. The affinity order of a range of commonly intercalated inorganic anions is: $CO_3^{2-} > HPO_4^{2-} > SO_4^{2-}$ for divalent anions, and $OH^- > F^- > Cl^- > Br^- > NO3^- > I^-$ for monovalent anions. The pH of the exchange medium must be well adjusted so

as to promote the exchange of ions as well as prevent the dissolution of the LDH particles [24, 32].

1.2.2.c Reconstruction

The method of reconstruction makes use of an interesting feature that LDHs possess namely the "structural memory effect". Briefly, the process starts by the calcination of the LDH, leading to the removal of interlayer water, anions and the hydroxyl groups, and the formation of a mixed metal oxide phase. Upon contact with an aqueous solution containing the desired guest anion, the calcined mixture is rehydrated, where water molecules reform the hydroxylated layers incorporating in between them more water molecules and the anions in solution: the original layered structure is 'reconstructed'. The memory effect is affected by the chemical composition of the LDH layers and the calcination temperature (a high calcination temperature reduces the memory effect). Such method is used when the intercalation of large organic guest molecules is needed. It also has the advantage of avoiding the competition between the counter-ions in the precursor metal salts and the anions intended for intercalation. The disadvantage of this method, though, is that it produces amorphous LDH products [32, 33].

1.3 Alginate Polymer

Alginate is a naturally occurring biopolymer. Commercially used alginate is either extracted from various species of the brown algae *Phaeophyceae* (*Laminaria hyperborean*, *Ascophyllum nodosum*, and *Macrocysis pyrifera*) or biosynthesized by the soil bacteria *Azotobacter vinelandii* and *Pseudomonas* species [14, 20]. Alginates comprise a group of linear, unbranched, anionic copolymers (polysaccharides), containing blocks of β-D-mannuronic acid (M) and its epimer α-L-guluronic acid (G) linked together through (1-4) glycosidic linkages. The polymer chain is composed of homopolymeric regions of either the G residues (G block) or M residues (M block), interrupted by regions containing alternating G and M residues, as shown in figure 1-2. The M/G content, the molecular weight, and the length and distribution of each block are variable depending on the source of alginate. The viscosity of alginate solutions is mainly a function of alginate's molecular weight. The solution's pH also affects its viscosity, where it increases as the pH decreases reaching a maximum at pH 3-3.5 [14, 15].

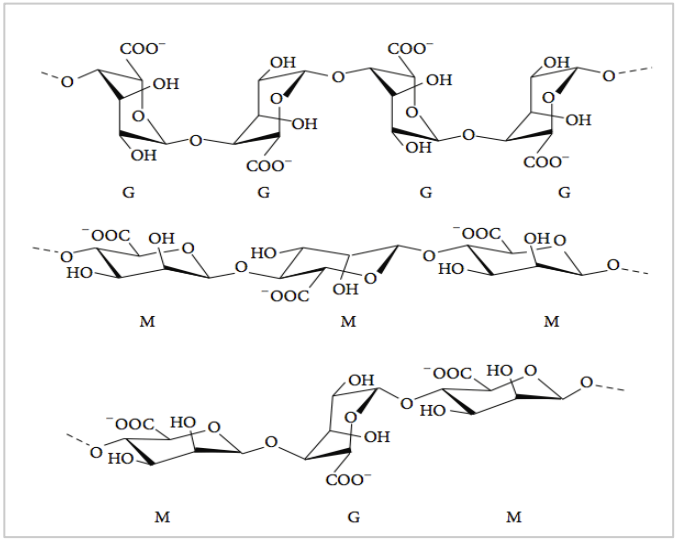

Figure 1-2. The molecular structure of alginate's building units: β -D-mannuronic acid (M) and α -L-guluronic acid (G) [20].

1.3.1 Gelation mechanism

One prominent feature of alginates is their ability to form hydrogels. Alginates can form two types of gels based on the gelling mechanism: acid gels and ionotropic gels. Acid gels form when alginate is exposed to a low pH environment, the charged carboxylate moieties of the monomer residues are protonated enough so that their interactions through hydrogen bonding overcome their electrostatic repulsive forces, leading to the formation of a physical gel [15, 34]. On the other hand, ionotropic gels form in presence of multivalent cations, such as Ca^{2+}, which is the most commonly used ion for alginate gelation. The gelation principle is based on the stereospecific and strong chelation of Ca^{2+} ions by the carboxylate moieties of the G blocks in adjacent polysaccharide chains. Cross-linked chains form double helices that further associate together to form an extended cohesive gel network. The guluronate blocks in the polysaccharide chains exhibit high selectivity coefficients for Ca^{2+} binding. This is attributable to the conformation of the guluronate sugar ring: the di-axial (1-4) glycosidic linkages impose restricted geometry upon the G block rendering it rather stiff. Consequently, the polyG polymer chains (over 20 residues in length) adopt a *zigzag* shape resulting in a regular periodic array of electronegative 'pockets' of size and geometry compatible with Ca^{2+} ions. Such arrangement is reminiscent of eggs sitting in the cavities of an egg carton, and thus the model that is proposed to describe the calcium alginate junction zones is referred to as the 'egg-box model', as depicted in figure 1-3 [20, 35-38].

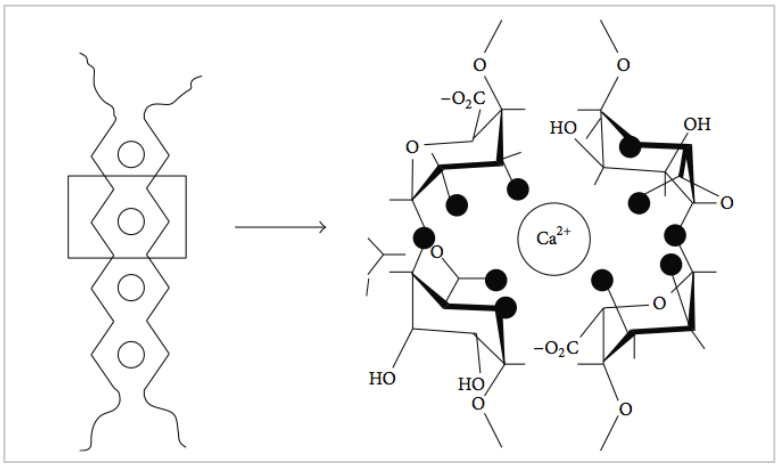

Figure 1-3. A depiction of the egg-box model describing the ionotropic gelation of alginates [34].

Alginate hydrogels can incorporate a wide variety of molecules during their gelling process and can be formulated into different forms such as fibers, films and block matrices, however they are more frequently processed in the form of spherical beads. Conventionally, alginate beads (>1 mm in diameter) are formed as a solution of sodium alginate (mixed with the desired species to be loaded) is extruded in a dropwise manner through needles/nozzles into a gently agitated dilute calcium chloride ($CaCl_2$) solution [34, 39]. It is worth mentioning that the alginate beads are not inert, but they are in dynamic interaction with their environment, and their transfer from one medium to another can induce a change in the equilibria that control the beads' structure. Therefore, well-studied control of the media the beads are stored/used in is crucial to ensure the maintenance of the desired bead stability and behavior [38]. The ionically cross-linked alginate beads are destabilized in the presence of chelating agents (such as EDTA, phosphates or citrates), which sequester the Ca^{2+} ions available for gelation, and in high concentration of ions such as Na^{+} and Mg^{2+}, which are exchanged with the Ca^{2+} in the alginate hydrogel causing its solubilization [15, 39, 40].

1.3.2 Properties of the Hydrogel Beads

The properties of the alginate hydrogel beads are influenced by inherent polymer properties such as its monomeric composition (M/G ratio and G content), the distribution of G, M and GM sequences, and the polymer's molecular weight. Because G residues are responsible for its crosslinking, gelation of alginate with high G status results in beads of increased stability and improved mechanical properties. It was empirically found by Martinsen *et al.* that alginates of G content > 70% and an average G block length > 15 are associated with the highest stability against monovalent cations, highest mechanical strength and lowest shrinkage [3, 20, 34, 41, 42]. The size of the produced hydrogel beads is a function of both the size of the needle used to extrude the alginate droplets and the alginate solution viscosity. Large diameter beads are formed by using large diameter needles and highly viscous alginate

starting solution. The shape of the beads is also affected by the alginate solution's viscosity where the higher its viscosity, the more spherical is the shape of the beads produced. The uniformity and the strength of the alginate beads were both found to be affected by the gelation kinetics. If the gelation process takes place rapidly, the hydrogel bead formation becomes poorly controlled, and therefore slowing the gelation rate, such as by reducing the temperature or using a poorly soluble form of Ca^{2+}, produces more uniform beads with higher mechanical and structural integrity. Other gelation conditions, such as the concentration of the alginate, and multivalent cation solutions, curing time, temperature and pH, were also found to play a crucial role in the final properties of the produced alginate gel beads [20, 43]. One of the key features of alginate gels is their pH-dependent swelling behavior. As the polymer chains encounter an aqueous medium, the thermodynamic advantage of exposing the carboxylate and hydroxyl anionic moieties to interact with the aqueous medium drives the polymer gel to swell and adopt an open structure to maximize such interactions [44]. Depending on its composition, the pKa of alginate lies in the range of 3.4 - 4.4. Below such pH the carboxylate groups of alginate are protonated rendering the polymer insoluble and the beads shrink due to reduced electrostatic repulsion. However, as the pH exceeds the pKa value, the carboxylate groups are ionized gradually, repelling one another and causing the polymer to hydrate and swell [38, 44-46].

1.4 The Vitamins: Chemistry and Functions

1.4.1 Vitamin B6

1.4.1.a Chemistry

Vitamin B6 is a water-soluble vitamin. The generic term refers to six chemical structures: the alcohol pyridoxine, the aldehyde pyridoxal, the amine pyridoxamine and their 5' phosphorylated forms. These compounds are metabolically interconvertible, and are claimed to possess equivalent biological activity. They are all based on 2-methyl-3-hydroxy-5-hydroxymethyl pyridine nucleus. The alcohol form pyridoxine (or pyridoxol) has a hydroxymethyl group ($-CH_2OH$) at position 4 of the pyridine ring, which is converted to an aldehyde group (-CHO) or aminoethyl group ($-CH_2NH_2$) in pyridoxal and pyridoxamine, respectively, via enzyme-catalyzed reactions [47, 48]. The chemical structure of pyridoxine is shown in figure 1-4.

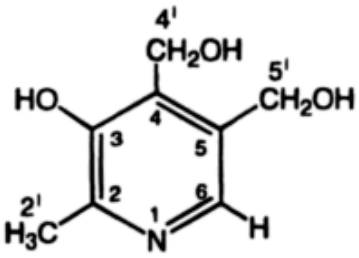

Figure 1-4. The chemical structure of pyridoxine (vitamin B6 molecule) [49].

Pyridoxine is more stable than pyridoxal and pyridoxamine and is thus the form used in pharmaceutical formulations and food fortification. Commercially available vitamin B6 is in the form of pyridoxine hydrochloride salt, which is a white crystalline powder of good water solubility (22 g/100 ml). The stability of vitamin B6 is pH-dependent: it is stable in acidic conditions but is less stable in neutral and alkaline conditions, especially under exposure to direct light [47, 48]. The pKa values of the pyridoxine molecule are 5 and 9 for the nitrogen of the pyridine ring and the phenolic OH, respectively. The pH-dependent molecular forms of pyridoxine are shown in figure 1-5 [50, 51].

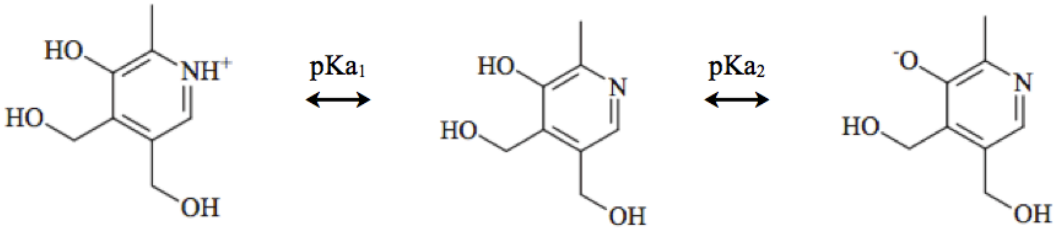

Figure 1-5. The pH-dependent molecular forms of pyridoxine ($pKa_1 = 5$ and $pKa_2 = 9$) [50, 51].

1.4.1.b Sources and biochemical role

The different forms of vitamin B6 are quite available in foods such as poultry, fish, eggs, liver, and to a lesser extent in meat and milk. Pyridoxine is mainly present in plant tissue, while pyridoxal and pyridoxamine are present more in animal tissues [47, 48, 52].

Vitamin B6, in its different forms, is absorbed by passive diffusion mainly in the jejunum and the ileum, which indicates a large capacity of absorption. Animals were found to absorb vitamin B6 in an amount of around 2-3 orders of magnitude more than their regular physiological needs. The biochemical role of vitamin B6 in the body is mainly through its biologically active form pyridoxal phosphate. It serves as a coenzyme for the metabolism of amino acids, in addition to modulating action of steroid hormones and regulating gene expression. Studies have shown that Vitamin B6 was, indirectly, involved in a number of

useful health effects. It was shown to positively affect the postnatal development of a learning-related glutamate receptor in the brain, and to be possibly associated with an improved immune function and lowered risk of colon cancer [52].
The recommended dietary intake of vitamin B6 is 2 mg for men and 1.6 mg for women, which increases by 0.6 mg for pregnant women and 0.5 mg for lactating ones. Vitamin B6 deficiency is quite uncommon. Low vitamin B6 intake may result in homocysteinemia, a condition that is associated with heightened risks of vascular occlusions, strokes, fractures, dementia, Alzheimer's disease and chronic heart failure. The vitamin's deficiency is also associated with a number of dermatologic changes and neurologic effects such as weakness, sleeplessness, peripheral neuropathies and impaired cell-mediated immunity. The administration of supra-nutritional doses of vitamin B6 provides pharmacological advantages in the management of a number of disorders such as sideroblastic anemia, sickle cell anemia, iron storage disease, schizophrenia, asthma, carpal tunnel syndrome, morning sickness premenstrual syndrome and to counteract the adverse effects of some drugs [47, 48].

1.4.2 Folic acid

1.4.2.a Chemistry

Folic acid belongs to the family of the water-soluble B vitamins (vitamin B9). Chemically, its structure is based on a pteridine heterocyclic ring linked to para-aminobenzoic acid (pABA). The carboxylic acid group of the PABA moiety is bonded to the amino group of glutamic acid via a peptide linkage as shown in figure 1-6 [47, 53].

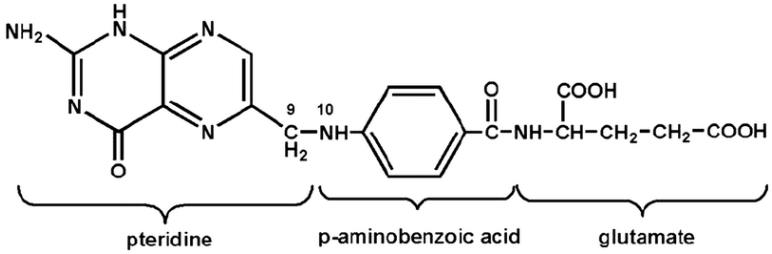

Figure 1-6. The chemical structure of folic acid [54].

Folic acid represents the basic chemical framework for the family of coenzymes/vitamers namely folates, which comprise tetrahydrofolate and its derivatives. In folates, the pteridine ring is fully reduced and is usually conjugated to multiple glutamate residues (typically 5-7 residues) via peptide linkages between γ carboxylic group of one glutamate and the α amino group of the adjacent one. This is in contrast to folic acid of which pteridine ring is fully oxidized and is only conjugated to one glutamic acid residue [47, 53]. In general, folic acid and its vitamers are minimally soluble in low pH solvents (pH = 2 - 4). Increasing the pH above such range increases the solubility as the anionic form increases in concentration. The pKa values of folic acid are 3.1 and 4.8 for the carboxylic acid groups of the glutamate

residue [55-57]. The pH-dependent molecular forms of folic acid are shown in figure 1-7.

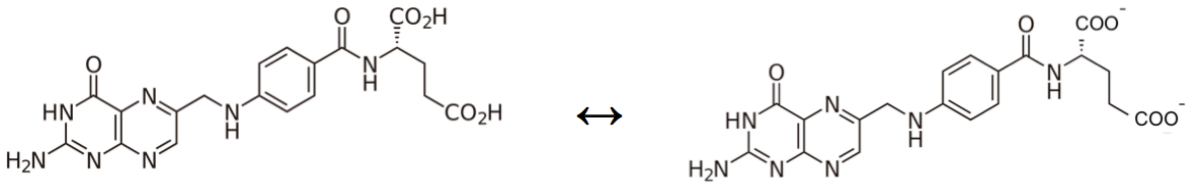

Figure 1-7. The pH-dependent molecular forms of folic acid (pKa_1 = 3.1 and pKa_2 = 4.8) [55-57].

Folates are stable in neutral and alkaline environments, however their stability is compromised when exposed to an oxidative environment, light, heat, and acidic pH changes (unstable at pH < 5). Such conditions are often encountered during storage, cooking or processing for food and pharmaceutical industrial purposes, and thus precautions must be established while handling folates in order to preserve their structural integrity [47, 48, 52, 53, 58].

1.4.2.b Sources and biochemical role

Folic acid does not occur in nature in appreciable amounts, unlike reduced folates, which occur in a wide variety of food sources of both animal and plant origins such as liver, legumes (peanuts, cowpeas and peas), leafy greens, citrus and other fruits. However, naturally occurring folates, which are in a polyglutamate form, when ingested orally, have to be converted to folic acid (monoglutamate) in order to be absorbed, and thus folic acid is considered the more bioavailable form of folates. Therefore, folic acid is the more commonly used form in pharmaceutical products and in food fortification. Folic acid absorption takes place via a carrier-mediated transport system. The extent of absorption of folic acid is the highest in the proximal jejunum. However, its is relatively poor in the distal jejunum, and not absorbed from the ileum, and therefore folic acid complete dissolution in the stomach is preferable before it misses its absorption window [47, 48, 52, 53, 58]. Folic acid serves as a precursor for many enzyme cofactors required for nucleic acid synthesis and amino acid metabolism [53]. Folate deficiency is one of the most prevalent vitamin deficiencies. It is attributable to malnutrition due to reduced consumption of fruits and vegetables, malabsorption conditions, and abnormal metabolism, in addition to the loss of a significant percentage of folates contained in the consumed food material due to poor storage, cooking or harsh processing conditions [58]. Folic acid intake has been linked to reduced risks of abnormalities in embryonic development, especially those in the brain and the spinal cord, referred to as neural tube defects. Folate deprivation was found to be associated with an increased risk of neoplastic transformations, leading to cancers of the colon, cervix, lung, mouth and pharynx, head and neck, gastrointestinal tract, and brain [52]. Severe deficiency

results in several disorders such as megaloblastic anemia, cardiovascular diseases, Alzheimer's disease, colon cancer and birth defects in the newly born. For adult men and women, the recommended daily allowances for folic acid are 200 and 180 μg, respectively. Since folic acid intake is quite critical during pregnancy for fetal growth and neural development, its recommended daily allowance is elevated up to 400 μg for pregnant women. Pre-conception folic acid intake is recommended as it was shown to lower the risk of neural tube defects. Folates are used pharmacologically at doses of 400 μg/day intramuscularly or 5 mg/day orally to treat megaloblastic anemia, and at doses < 1 mg/day they were found to be effective in reducing high/normal plasma homocysteine levels [47, 48].

1.5 Statement of Purpose

The aim of this research is to synthesize and characterize vitamin-loaded alginate/LDH bionanocomposites of different alginate:LDH ratios, and investigate their performance as CR-DDSs in conditions simulating the pH changes along the gastrointestinal tract. The model bioactive molecules used for this purpose are vitamin B_6 and folic acid. Both vitamins are prone to degradation on prolonged storage, and they are both absorbed in the small intestines. They would therefore benefit from a platform such as alginate/LDH bionanocomposite as a protective vehicle that can deliver their doses efficiently to their absorption site and sustain their release.

Chapter 2. Literature Review

2.1 Alginate in Drug Delivery Systems

Alginate has been used for over three decades to encapsulate a wide spectrum of bioactive molecules such as pharmaceutical and nutraceutical molecules, proteins, and nucleic acids [3]. Alginate is either used on its own or, more commonly, combined with other polymers or inorganic/organic fillers for the purpose of controlled drug release [58-63].

Yegin et al. reported the encapsulation of the water-insoluble NSAID (non-steroidal anti-inflammatory drug) sulindac in alginate beads, in an attempt to exploit alginate's gastroprotective properties against the NSAID's irritant nature. Effects of sodium alginate concentration and the size of the needle used for its extrusion into the gelling solution on the beads' properties were investigated. The particle size was found to increase with increasing needle size from 0.45 to 0.9 mm., but it was independent of the alginate solution concentration. The highest entrapment efficiency (94%) belonged to the sample with highest alginate concentration (2%) extruded through the 0.9 mm needle. Beads prepared with high alginate concentration exhibited a statistically significant decrease of the sulindac release rate in phosphate buffer of pH 6.8. The 1% alginate formulation resulted in a complete drug release in 2 hours, whereas the 2% formulation released 90% of its cargo in 4 hours. Evidence from *in-vivo* investigations on gastric and duodenal tissues from albino mice showed the significant mucoprotective effect of the NSAID-loaded alginate by the absence of evidences of hemorrhagic areas, both macroscopically and microscopically [64].

In another study, Sultana et al. developed a controlled release drug delivery system comprising the anti-tuberculosis drug isoniazid. The drug was entrapped in alginate microspheres, which were prepared by a modified emulsification method. Effects of different drug:polymer ratios, cross-linker and alginate solutions' concentration and cross-linking duration were studied and correlated to the properties and drug release behavior of the alginate microspheres. Increasing the concentration of the alginate and the cross-linker solutions and increasing the cross-linking time were found to increase the mean particle size of the microspheres. The highest entrapment efficiency of (91%) was associated with microspheres prepared with a drug polymer ratio of 1:5, a cross-linker solution of 7.5% and cross-linking time of 20 minutes. Optimized isoniazid-loaded alginate microspheres were found to exhibit good bioadhesive properties, which is reflected in their prolonged retention in the small intestines. Drug release from the optimized formulation was studied in simulated gastric and intestinal fluids: around 26% of isoniazid was released in the gastric fluid at pH 1.2 along 6 hours, whereas 71.25% was released in the intestinal fluid at pH 7.4 along 30 hours [65].

Namdeo et al. prepared theophylline-incorporated alginate microspheres by an emulsification method. Effects of the alginate and cross-linker solutions' concentration, and the

polymer:drug ratio on the properties of the produced microspheres were investigated. It was shown that the higher the polymer concentration, the more viscous its solution is, which produces larger droplets and consequently larger drug-encapsulated microspheres. Increasing the concentration of the cross-linker also increases the size of the microspheres. However, increasing the cross-linker concentration beyond 10% (w/v) resulted in beads of irregular shape. The entrapment efficiency ranged between 72.63 and 93.65 % for the different polymer:drug ratios, the highest belonging to the 4:1. *In-vitro* release studies, simulating the pH changes along the gastrointestinal tract, showed that the alginate microspheres did not disintegrate in the acidic stomach environment and delayed the release of theophylline until it reached the intestinal environment. Increasing the polymer:drug ratio was found to decrease the rate and extent of theophylline release, which can be explained by the increase in the density of the polymer matrix [66].

The anti-anginal drug Trimetazidine dihydrochloride was loaded in calcium alginate matrices by two methods: either into preformed beads, namely the sequential method, or loaded during gelation (simultaneous method). Parameters such as calcium chloride concentration, alginate concentration and drug:alginate ratio were varied to study their effects on the produced beads and compare the two preparation methods. The highest loading (about 62% w/w) was realized with the beads prepared by the sequential method with a $CaCl_2$ concentration of 3% (w/v), sodium alginate concentration of 2.5% (w/v) and drug solution concentration of 2% (w/v). In the sequential method, the entrapment efficiency increased with $CaCl_2$ and polymer concentration but decreased with higher drug concentration. Whereas in the simultaneous method, the entrapment efficiency increased with polymer and drug concentration, while it increased with $CaCl_2$ concentration up to a threshold value, then it decreased. The polymer concentration and the drug release behavior were shown to exhibit a directly proportional relationship for both methods. Increase in the $CaCl_2$ concentration decreased the rate of drug release in the sequential method up to a particular concentration. FTIR analyses revealed no interactions between the drug and the polymer matrix [67].

Singh et al. evaluated the performance of riboflavin-loaded alginate beads on changing their cross-linking time in ten samples between 15 minutes and 1 hour. It was shown that the drug entrapment efficiency is affected by the cross-linking time. The highest entrapment efficiency of about 74 % (w/w) belonged to the sample cross-linked for 15 minutes. Increasing the cross-linking time lead to slower drug release properties in 0.1 M HCl dissolution media: 64% of the drug was released from the sample cross-linked for 1 hour, compared to 80% drug release for the 15-minutes cross-linked sample [68].

Alginate was also used to contain and protect biological macromolecules such as enzymes, against the acidic environment of the stomach. Anifantaki et al. reported the encapsulation of the garlic-derived enzyme allinase in calcium alginate beads for that purpose. Allinase

enzyme catalyzes the production of allicin, which is the main ingredient responsible for most of the useful health benefits of garlic, from its precursor alliin. The concentration of the alginate solutions used for the beads' preparations was varied from 1.2 to 3.6% (w/v). Alginate concentration of 3.6% (w/v) showed the most promise in retaining the enzyme and maintaining its activity for prolonged periods. At such concentration, the polymer network is tight enough to limit the protein diffusion. The allinase-loaded beads were found to retain the enzyme and maintain their integrity on exposure to pH 1.2 simulating the acidic environment of the stomach [69].

Jelvehgari et al. reported the development of a colon-targeted drug delivery system based on piroxicam-loaded alginate beads. Piroxicam is an NSAID used to treat arthritis-caused pain and inflammatory symptoms. Piroxicam-alginate microspheres were prepared using multiple alginate concentrations resulting in different drug-polymer ratios of 1:2.5, 1:5 and 1:7.5. It was found that the 1:2.5 yielded the best results as compared to the other ratios, with about 29% (w/w) loading efficiency and about 83% (w/w) production yield (defined as the quantity of beads produced as a function of the amount of polymer and drug loaded). However, in the same study, the drug was entrapped in alginate-pectin matrices and was shown to produce better results. In general, the alginate and the alginate-pectin matrices offered mucoadhesive properties, protection of the drug in acidic medium and colon-targeted sustained drug release [70].

2.2 LDHs in Drug Delivery Systems

Along the span of the past two decades, there has been an increasing number of reports on the use of LDHs in biomedical applications in general, and in drug and gene delivery systems in particular. The earliest investigation on the use of LDHs in controlled release formulations was reported by Doi et al. in 1985, where the synthesis and the application of LDH in the controlled drug delivery of nifedipine, an antihypertensive drug, was described [71]. In this section, a literature summary on the use of LDHs in drug delivery, with particular focus on vitamins and antioxidants, of relevance to this current investigation, is presented.

2.2.1 Vitamins and antioxidants

Most vitamins are unstable when exposed to oxygen, light and high temperatures, which would eventually lead to their fast degradation and limit their application as active ingredients in food, pharmaceuticals and cosmetics. Over the past 15 years, a wide range of vitamins and antioxidants were successfully incorporated into LDHs benefiting from the LDHs' features as stabilizing and protective nano-vessels that maintain the structural integrity of their loaded species against harsh storage conditions and fast physiological degradation, in addition to controlling their release properties according to the physiological

needs.

Hwang et al. reported one of the earliest trials of intercalating a number of vitamin compounds in LDHs and zinc basic salts, these being: retinoic acid (vitamin A), ascorbic acid (vitamin C) and tocopherol succinate (vitamin E). The three vitamins, being of anionic nature, were successfully intercalated as evidenced by XRD analyses showing expansion in the LDH interlayer spacing [72].

Choy et al. further investigated the intercalation of vitamins C and E in LDHs and their controlled release properties. Pristine Zn-Al LDHs of M^{2+}/M^{3+} ratio of 2:1 were synthesized by direct co-precipitation. Vitamin C was loaded by anion exchange with the pristine LDHs at pH 7, whereas vitamin E was loaded by direct co-precipitation with a mixed metal solution of Zn^{2+} and Al^{3+} salt precursors of Zn/Al molar ratio of 3:1 at pH of 7.5. XRD analyses proved the intercalation of both vitamins based on the expansion in the basal spacing from 8.7 Å of pristine LDHs to 10.5 Å and 53.8 Å corresponding to monolayer and double-layer arrangements of vitamin C and vitamin E in the interlayer space, respectively. Vitamin loading percentages in the LDHs were estimated via chemical analyses to be about 23% (w/w) for vitamin C and about 61% (w/w) for vitamin E. The vitamins were shown to preserve their structural integrity, and their release was shown to be slowed down and controlled sufficiently by their intercalation in the Zn-Al LDH nanomatrices [73].

Gasser reported the successful intercalation of vitamin C in LDHs with Fe^{3+} as the trivalent cation. Pristine Zn-Fe and Mg-Fe LDHs ($M^{2+}/M^{3+} = 2$) were synthesized by co-precipitation reaction, then the vitamin was loaded by anion exchange with the pristine LDHs. Intercalation of vitamin C in both LDHs was confirmed by XRD analyses, demonstrated by expansions in the basal spacing values from 8.5 and 7.9 Å to 10.8 and 11.5 Å, for Zn-Fe and Mg-Fe LDHs, respectively. The well-defined (00*l*) peaks imply the preservation of the layered structure integrity after the anion exchange process. In the de-intercalation studies conducted in 0.5 M aqueous carbonate solution, it was shown that the Mg-Fe LDH is more effective as a drug release system than the Zn-Fe LDH, since the release rate of vitamin C from Mg-Fe LDH is relatively slower and the amount released increases gradually with time. Whereas the release of vitamin C from Zn-Fe LDH is very rapid in the first 15 minutes and then the release almost stops. This finding reflects a stronger interaction between the anionic vitamin C and the Zn-Fe LDH layers, which is attributable to the higher charge density of its layers as compared to Mg-Fe LDHs. Unlike prior studies, the release of vitamin C from LDHs prepared in this investigation was not complete even after 120 minutes, which reflects the possibility that the intercalated molecules are deeply embedded in the LDH host [74].

In a more recent study by Gao et al., the intercalation of vitamin C in Mg-Al and Mg-Fe LDHs ($M^{2+}/M^{3+} = 3$) by a calcination-rehydration (reconstruction) process was reported, in attempt to improve the loading percentage, and the amount released of the vitamin from its

LDH host, which did not exceed 50% in the previous studies. After the synthesis of the pristine LDHs by co-precipitation at pH 10, they were calcined at 500 °C for 5 hours in a muffle furnace into the oxide form and then rehydrated in a solution of excess vitamin. The release profile was indeed improved as compared to previously reported profiles. The percentage of vitamin released in the aqueous carbonate medium reached up to 60% for the Mg-Al LDH, which was shown to be a better release system than Mg-Fe LDH with higher release amount and release rate [75].

A novel drug delivery system for vitamin C comprising Ca-Al LDH (Ca^{2+}/Al^{3+} ratio = 2) was developed. Vitamin C was successfully intercalated by co-precipitation as evidenced by XRD, which showed an interlayer expansion corresponding to a vertical alignment of the vitamin molecules. The loading percentage was estimated to be 36.4% (w/w). The vitamin release behavior was tested in phosphate buffer of pH 7.4, and it exhibited an extended release profile, with a maximal release percentage of 80% of the total loaded drug [76].

Several reports on the incorporation of folic acid in LDHs for its controlled delivery were found in literature published throughout the past 8 years. Qin et al. attempted the intercalation of folic acid in Mg-Al LDHs (Mg^{2+}/Al^{3+} = 2) by co-precipitation and anion exchange. This was conducted at pH 10. Both methods succeeded in the intercalation of folic acid as evidenced by XRD analyses, resulting in an expansion in the basal spacing from 8.4 for the pristine Mg-Al LDHs to 15.3 Å and 16 Å for the co-precipitated and anion-exchanged samples, respectively. The interlayer distances were calculated to be shorter than folic dimensions, so they are attributed to a tilted longitudinal monolayer arrangement of the intercalated molecules. The loading percentages corresponded to about 19% (w/w) and 18% (w/w) for the co-precipitated and anion-exchanged samples respectively. Cytotoxicity studies showed that the LDH host is non-toxic to normal 293 T cells. The LDHs were also shown to exhibit a good buffering effect in acidic media, which makes LDHs ideal for the controlled delivery of drugs that may irritate the stomach [77].

An interesting study was reported by Xiao et al. in which they developed, for the first time, folic acid-intercalated LDHs of ternary nature: Mg/Zn/Al –LDHs. These LDHs were prepared and intercalated with folic acid by co-precipitation, using mixed metals precursor solutions of [total M^{2+}]/M^{3+} ratio = 3. The intercalated folic acid achieved a much-improved loading percentage of 45.2% (w/w) when compared to previously reported binary LDH systems. Such drug carrier exhibited a profound buffering capacity and an extended drug release profile [78].

Bashi et al. successfully intercalated folic acid in Ni-Al LDH (Ni^{2+}/Al^{3+} = 3) by coprecipitation and studied its release in carbonate, sulphate and phosphate dissolution media [79]. The application of folic acid-intercalated Mg-Al LDHs as novel antioxidant and anti-fatigue nutritional supplements was assessed *in-vitro* in a study by Qin et al. The results

showed great promise for such hybrid particles, which were demonstrated to possess obvious antioxidant activity and they exhibited increased endurance capacity in animal studies [80].

A recent study on folic-LDH hybrids was reported by Kim et al. In this study, a dual nutraceutical nanohybrid comprising folic acid-intercalated Ca-Al and Ca-Fe LDHs were prepared. Such nanohybrid serves simultaneously as a vitamin delivery vehicle and as a Ca^{2+} mineral supplement. Successful intercalation was demonstrated by XRD analyses on samples prepared by coprecipitation, ion exchange, solid phase reaction and exfoliation-reassembly processes. It was found that exfoliation-reassembly exhibited the most effective intercalation, and the loading percentage values were estimated to be 60% (w/w) and 72% (w/w) for Ca-Al and Ca-Fe LDHs respectively [81].

Reports on the successful intercalation of antioxidant drugs such as carnosine, gallic acid and vanillic acid in Zn-Al and Mg-Al LDHs were documented in literature. Their incorporation in LDHs was associated with superior antioxidant properties, in addition to exhibiting excellent controlled drug release behavior as reported by Kong et al. and Silion et al. [82, 83].

2.2.2 Therapeutic drugs

Kovanda et al. reported the intercalation of the analgesic and antipyretic paracetamol in Mg-Al LDHs of M^{2+}/M^{3+} molar ratio of 2:1. Being a non-ionic drug, it was preferably intercalated by reconstruction, where the co-precipitation-synthesized Mg-Al LDHs were calcined at 500 °C, and the produced Mg-Al mixed metal oxide was then rehydrated in aqueous paracetamol solution. Structural and chemical analyses, and molecular modeling were employed to confirm intercalation and study the interactions between the drug and the brucite-like sheets. It was shown that the drug was successfully intercalated in Mg-Al LDHs, and exhibited a pH-dependent and slower release when compared to the powdered pharmaceutical without incorporation in LDH [84].

The incorporation of anti-inflammatory drugs (especially NSAIDs) in LDHs is an extensively studied area of research, in attempt to improve their solubility and control their release, thus alleviating/minimizing the local and systemic side effects associated with most of them. Previous *in-vivo* studies in rodents have shown that incorporating such drugs in LDHs ensures a buffered environment and reduces the ulcerating effects of gastro-irritant drugs. Ketoprofen was intercalated by ion exchange into co-precipitated Zn-Al and Mg-Al LDHs of M^{2+}/M^{3+} molar ratio of 2:1, at a constant pH of 8.5 and 9.5 respectively. The intercalation was confirmed by XRD and FT-IR. The prominent finding in this study was the *in-vivo* experiment conducted on mice models, which demonstrated the protective role of LDHs on the gastrointestinal mucosa against NSAID-induced lesions. Moreover, the analgesic effect of ketoprofen intercalated in LDH was shown to be slightly higher and to be

of more prolonged effect when compared to ketoprofen alone. In this study, Mg-Al LDH exhibited superior properties when compared to the Zn-Al LDH in terms of the analgesic efficacy and the release sustainability [85].

An ocular diclofenac-LDH drug delivery system was developed and investigated by Cao et al. The challenge of most ophthalmic preparations is that the structure of the eye restricts the passage of drug molecules. In most cases, only 5% of administered drugs make it to the aqueous humor. Diclofenac was intercalated in Zn-Al LDHs (M^{2+}/M^{3+} = 2) at pH 7-8 by co-precipitation in water, and two different solvents: 10% Ethanol and 2% PEG 400 (polyethylene glycol), and were stable for 3 months at room temperature. The loading percentages were about 30%, 32% and 35% (w/w) for LDHs intercalated with diclofenac in water, 10% ethanol and 2% PEG 400, respectively. The intercalated products were dispersed in 4 types of formulations as ophthalmic drops that were maintained at pH of 7-7.4, and were tested for their *in-vivo* performance on albino rabbits. The bioavailability of diclofenac when intercalated in LDHs was improved greatly and its elimination slowed down, owing to the electrostatic interactions between the positively charged layers of LDHs and the eye surface [86].

In a study by Minagawa et al., LDHs were used to intercalate sulindac for the purpose of improving its dissolution profile, being a sparingly soluble drug. Mg-Al LDHs (M^{2+}/M^{3+} molar ratio = 2:1) were synthesized by co-precipitation at pH 8. One fraction of these LDHs (in nitrate form) was intercalated with the drug by ion exchange, and the other was calcined at 500 °C, then rehydrated by dispersion in a solution of the drug. An amount of sulindac was also intercalated by co-precipitation. The loading percentages of sulindac in LDHs varied according to the intercalation technique, being maximum in co-precipitation corresponding to a value of 45% (w/w), whereas loading ratios of 31% (w/w) and 20% (w/w) were calculated for ion-exchange and reconstruction-based intercalation respectively. It was shown that the solubility in simulated stomach dissolution media of co-precipitation-intercalated sulindac was improved by more than three times when compared to the drug without LDH. Around 80% of the intercalated sulindac was released in a controlled manner along a 3-hour period in the simulated intestinal dissolution media, whereas sulindac without LDH reached a maximum of 96% dissolution in the first 45 minutes. In addition to the improved drug solubility and the sustained release behavior, the LDH was shown to preserve sulindac against photodecarboxylation, enhance its thermal stability and its controlled release performance is expected to help demolish the gastrointestinal ulceration effects and cardiovascular toxicity [87].

Numerous studies on the intercalation of various anti-cancer agents were reported in literature. In the study by Chakraborty et al., methotrexate was intercalated in Zn-Al LDHs (Zn^{2+}/Al^{3+} = 2) by ion exchange at pH 8.5. Successful intercalation was confirmed by XRD

analyses, which showed an expansion in the basal spacing from 8.4 Å to 21.4 Å. The drug release profile, in phosphate buffer saline at pH 7.4, showed that ~ 50% of the loaded methotrexate was released in 6 hours, increasing linearly up to ~ 90% in 24 hours, and reaching 100% in 48 hours. The drug release was shown to be diffusion-controlled [88].

In another study by Chakraborty et al., methotrexate was successfully intercalated in Mg-Al LDHs as evidenced by XRD analysis showing an expansion of the basal spacing from 7.74 Å to 14.99 Å, and by FT-IR analysis. The loading percentage was calculated to be about 13% (w/w). Release studies in phosphate buffer saline at pH 7.4 showed that only about 50% of the intercalated drug was released in 15 hours, 90% was released in 95 hours and the release was complete in 190 hours. Such prolonged release profile inferred that that the drug release was governed by both crystal dissolution and diffusion. Such nanohybrid was found to have higher efficacy when tested on HCT-116 cell lines [89]. Modifications in the synthesis route of methotrexate-intercalated LDHs were applied and studied in two more reports. The choice of synthesis route influences the morphology and particle size of the nanohybrids, which finally reflects in the drug release profile [90, 91].

Etoposide (VP16), a semisynthetic derivative of podophyllotoxin, is an antitumor drug that is particularly used in treating gastric carcinomas. In a study by Qin et al., the intercalation of the VP16 in Mg-Al LDHs (Mg^{2+}/Al^{3+} = 3) was done in a two-step process. First, tyrosine was intercalated into the LDHs by co-precipitation at pH 10. Then the tyrosine-intercalated LDHs were ion exchanged with VP16 at pH 12. Intercalation was confirmed by XRD (basal spacing expanded from 0.84–1.18 nm) and FT-IR. The intercalated hybrids were shown to have a good buffering effect in gastric media and thus are ideal for administration of drugs that treat gastric irritation. The loading percentage was calculated to be 21.94%, and the drug exhibited a sustained release profile [92].

Li et al. reported the use of LDHs for the simultaneous delivery of 5-fluorouracil (5-FU) and Allstars Cell Death siRNA (CD-siRNA) for the effective treatment of cancer. The drug delivery system is based on intercalating 5-FU within the LDH layers by anion exchange, and loading the siRNA on the surface of the LDH nanoparticles. Such combined system proved to be an efficient platform for cancer therapy [93].

Barahuie et al. reported the intercalation of chlorogenic acid (CA) in Zn-Al LDHs (Zn^{2+}/Al^{3+} = 4) by co-precipitation and ion exchange. Both methods resulted in comparable loading percentages: about 43% and 45% (w/w) for the anion exchange and co-precipitated samples respectively. Successful intercalation was confirmed by XRD. Both hybrids were shown to sustain the release of the drug. It was found that the co-precipitated sample exhibited a lowered release rate than the anion-exchanged one. The release rate was generally slower at pH 7.4 than pH 4.8 for both samples due to their pH-dependent release mechanism [94].

Barahuie et al. reported the intercalation of another anticancer drug: protocatechuic acid in Zn-Al LDH (Zn^{2+}/Al^{3+} = 2) by co-precipitation and ion exchange methods, with loading percentages of 29.2% and 32.6% respectively. The sustained release behavior of the nanocarriers and their superior anti-tumor effects were demonstrated by *in-vitro* studies [95].

Al ali et al. reported the successful intercalation of the antihypertensive drug perindopril erbumine into Mg-Al LDH, and compared such nanohybrid with perindopril-intercalated-Zn-Al LDH reported in literature. The drug was intercalated by anion exchange. The loading percentage was reported to be about 37% (w/w). Perindopril exerts its antihypertensive action via inhibiting angiotensin-converting enzyme (ACE). The drug-loaded Mg-Al LDH hybrid was shown to exhibit a more controlled release behavior than Zn-Al LDH and was more efficient in inhibiting ACE enzyme [96].

Furosemide, an antidiuretic drug, has low water-solubility and low-permeability properties. Perioli et al. prepared furosemide-intercalated Mg-Al LDHs (Mg^{2+}/Al^{3+} = 2) in order to study their effect on improving gastric absorption of the drug. The nanohybrid had a final loading percentage of about 56% (w/w). *In-vitro* studies comprising pig gastric mucus showed that the intercalated drug exhibited enhanced gastric absorption properties [97].

2.3 LDH-Alginate Bionanocomposites in Drug Delivery Systems

Only very few publications reported the synthesis and the application of LDH-alginate bionanocomposites as drug delivery vehicles. Diclofenac sodium, a NSAID, was successfully incorporated into LDH-alginate bionanocomposites, and its release behavior investigated in two studies by Zhang et al and Hua et al. In the study by Zhang et al., pristine Mg-Al LDHs of x value ~ 0.34 were synthesized by co-precipitation at pH 10, and were loaded with the drug by anion-exchange and surface adsorption. Beads with multiple LDH:alginate ratios were prepared by the dispersion of predetermined amounts of the drug-loaded LDHs in 3% (w/v) sodium alginate solution and subsequent gelling in 5% (w/v) calcium chloride solution, followed by filtration and drying of the beads. The LDHs and the beads were characterized by FTIR and XRD to confirm drug intercalation and to investigate the interactions between the LDH, the alginate polymer and the drug. The percentage of LDH in the LDH-alginate composite was correlated to the swelling behavior of the composite beads, where the increase in LDH content was found to decrease the swelling properties of the hydrogel beads. The composite beads avoided almost any release of the drug in simulated gastric fluid, and sustained the drug release in simulated intestinal fluid. It was proposed that the positive brucite-like layers of LDHs minimize the repulsive forces between the COO^- groups of alginate, in addition to serving as inorganic cross-linkers restricting the mobility of the alginate polymer chains and thus reducing their swelling properties. Such effects were shown to result in improved controlled release behavior in addition to increased entrapment

efficiency of the drug as compared to the neat alginate beads [21]. In the study by Hua et al, Mg-Al LDHs and their alginate composites are prepared in the same way, except that before the loading of the drug, the LDH was calcined in a muffle furnace at 500 °C to convert it to the mixed oxide form and then the calcined LDH was mixed and loaded with the drug. The layered structure was reconstructed during the gelling step in the $CaCl_2$ solution. Such drug release system showed similar pH-sensitive swelling properties as Zhang et al.'s system. The calcined LDH, though, was found to result in a relative improvement in the maximum entrapment efficiency (for the 1:1 ratio composites) from about 70% to about 95% (w/w) [22]. In another study by Mahkam et al, a Zn-Al LDH-alginate composite was investigated for the controlled release of insulin and was shown to support the stability of the peptide drug and serve as a suitable matrix for pH-sensitive controlled drug release [18].

In a number of studies, alginate was combined with another biocompatible material and hybridized with the LDHs in attempt to refine the overall release performance of the incorporated drug. In a study by Alcantara et al., the hydrophobic protein zein was used in association with alginate in a bionanocomposite for the controlled drug delivery of ibuprofen. The hydrophobic zein improves the stability of the drug delivery matrix by acting as a barrier to moisture and oxygen, in addition to controlling and adjusting the drug release. Ibuprofen-intercalated Zn-Al LDHs were incorporated in alginate/zein polymer matrices of different zein percentage compositions (0%, 20% and 50%). The encapsulation efficiency was found to be highest (about 52 % w/w) in composites comprising ibuprofen-intercalated LDHs in the polymer matrix of 50% zein composition, compared to only about 10% (w/w) encapsulation for the binary alginate/LDH system. Such drug delivery system exhibited a highly controlled drug release performance in conditions simulating the passage of the drug down the gastrointestinal tract, with a practically complete protection against the acidic medium of the stomach. The speed of delivering the drug was shown to decrease as the zein content in the composite increases [19].

2.4 Other LDH-Polymer Bionanocomposites in Drug Delivery Systems

LDHs have been 'hybridized' with a number of biocompatible polymers other than alginate that serve a protective role for the orally administered LDHs against their breakdown in the stomach's environment. Such LDH-polymer composites offer additional advantages to the controlled release performance of LDHs.

Eudragit® is the trade name for copolymers composed of the esters of acrylic and methacrylic acids. Variation in the proportions of the acidic, neutral and alkaline groups produces different grades of the polymer, each with different physicochemical properties. Eudragit® S/L refers to the enteric-type methacrylate polymer: it is insoluble in acidic medium. When used in oral drug delivery systems, it provides a barrier against drug release

in the stomach and slows down its release in the intestines [98] In a study by Arco et al., the intercalation of the NSAID fenbufen into Mg-Al and Mg-Al-Fe LDHs was conducted by co-precipitation, ion exchange and reconstruction. Such techniques lead to successful intercalation, except for Mg-Al-Fe failing to intercalate the drug by reconstruction. The successfully intercalated systems were coated with Eudragit® S100, which is insoluble below pH 7, by two procedures: simple dispersion and microspheronization. It was shown that the microsphere forms are associated with homogenous, smooth surfaces, and encapsulation efficiency values ranging between: 85%-94%. The polymer coating of fenbufen-intercalated LDHs into microspheres exhibited no dissolution in the stomach (pH 1.2), but after exposure to the intestinal fluid (pH 6.8), fenbufen is released, however, in a slower rate than without the polymer coating [99].

Pan et al. reported the intercalation of doxifluridine, an anticancer drug, into Mg-Al LDHs and then having the nanohybrid coated by Eudragit® L100 via oil-in-oil solvent evaporation method for the purpose of delaying and targeting the drug release. The encapsulation efficiency was 88%. The *in-vitro* release experiments showed that the polymer coating endowed the drug-intercalated LDH with colon-targeted drug delivery performance, in addition to controlling the drug release profile. Only 6% of the drug was released in 2 hours at pH 1.2, whereas in pH 6.8, after a 10-minute delay, 60% of the loaded drug was released in 3 hours, followed by a 12% drug release at pH 7.4 for 2 more hours, to reach an equilibrium final release level of 79% [100].

More recently, Kim et al. investigated the development of Ca-Al LDH, which itself serves as a mineral supplement for Ca^{2+} in the body. The LDH nanoparticles were coated with Eudragit® L100 in the presence of ethanol solution to avoid the intercalation of the polymer in LDHs. The enterically coated Ca-Al LDHs suppressed the dissolution of Ca^{2+} ions at pH 1.2, indicating that the Ca-Al LDHs were well protected from the acidic gastric media [101].

Kankala et al. reported the incorporation of the hydrophobic drug sulfasalazine in a multi-layer Eudragit® (S/L 100)-coated Mg-Al LDH nanocarriers. The stability of these carriers in acidic media was found to be greatly enhanced: on exposure to 0.1 M HCl for 4 hours they underwent a maximum of 20% weight loss, as compared to 80% weight loss for the uncoated particles. The multiple enteric coatings of the sulfasalazine-intercalated LDH improved the release behavior of the drug by 20% (compared to the uncoated LDHs) and were found to serve as emulsifiers improving the solubility of the hydrophobic drug, thus enhancing its bioavailability in the colon [102].

Another polymer that was used in composites with LDHs for drug delivery purposes is carboxymethyl cellulose (CMC). Barkhordari et al. prepared a drug delivery system comprising ibuprofen-intercalated Mg-Al LDH ($Mg^{2+}/Al^{3+} = 2$) embedded in CMC gel beads that are cross-linked in $FeCl_3$ solution. The LDH-polymer composites were characterized by

FT-IR to confirm and investigate the CMC-Fe^{3+} interactions, and their surface morphology was examined by Scanning Electron Microscopy (SEM). The loading amount of ibuprofen was determined to be 0.156 g/g. The composite beads exhibited a pH-dependent release profile. In acidic media, the CMC-LDH beads released negligible amounts of ibuprofen (less than 10%), in contrast to the case in absence of CMC, where the ibuprofen-intercalated LDHs released 60% of the drug load in about 60 minutes. The release is increased in basic media of pH = 7.4, however CMC-LDH-ibuprofen composites exhibited slower release than LDH-ibuprofen alone [103].

Chitosan, a cationic polysaccharide, was used as a drug carrier for its mucoadhesive properties that aid in prolonging the drug's residence time at its targeted site. Ribeiro et al. exploited the mucoadhesive properties of chitosan to encapsulate the NSAID 5-aminosalicylic acid (5ASA)-intercalated Mg-Al LDHs, to target and control its release in the colon, which is its site of action for the treatment of ulcerative colitis and Crohn's disease. The chitosan-coated 5ASA-intercalated LDHs particles were coated with the anionic polysaccharide pectin, which is stable in acidic conditions unlike chitosan and LDHs, and thus protects the drug-loaded vehicle through its journey down the intestinal tract to the colon. Pectinases present in the colon digest the pectin coating consequently initiating the drug release process. Increasing the amount of pectin in the ternary composite system was found to be associated with an increased amount of the incorporated drug. The pectin coated beads showed an enhanced stability against acidic medium when compared to the release of drug from either chitosan on its own or chitosan-LDH composites, where only 10% of 5ASA were released in the former composite as compared over 90% release from the latter ones. Moreover, the kinetics of the drug release can be fine-tuned by varying the pectin coat thickness [104].

2.5 Folic acid and Vitamin B6 in Clay/Polymer-based Drug Delivery Systems

A mixed-polymer system based on alginate and pectin was developed for the purpose of folic acid delivery in foods by Madziva et al. Microcapsules of multiple pectin percentages, 20%, 30% and 40% were prepared at different $CaCl_2$ solution concentrations: 0.1, 0.5 and 1 M. The effects of such variables, in addition to sodium alginate's concentration and the contact time of the microcapsules with the $CaCl_2$ hardening solution were studied. It was found that the capsular diameter increased with the increasing the hardening time of the microcapsules. The highest encapsulation efficiency of about 89 % (w/w) belonged to the sample of 30% pectin composition. Increasing the $CaCl_2$ concentration from 0.1-0.5 M increased the folic acid loading from 25 to 53% (w/w). It was found that the alginate-pectin composites improved the stability of the encapsulated folic acid against environmental factors during prolonged storage when compared to the free folic acid and that encapsulated in alginate

alone. As for testing the *in-vitro* release profile, it was found that the composite protected the folic acid in gastric media, and increasing the pectin percentage slows down the folic acid release [53].
Stevanovic et al. reported the loading of folic acid in poly(DL-lactide-co-glycolide) or PLGA polymer nanoparticles to sustain the vitamin's delivery for prolonged periods. The concentration of folic acid solution was varied to obtain different PLGA/folic acid ratios. Nanoparticles of 95% PLGA composition exhibited the highest loading efficiency of about 79% (w/w). The *in-vitro* release profile of folic acid, spanning a period of 30 days, shows an initial burst release of 17% of folic acid in the first day, due to the amounts adsorbed on the surface. The next 11 days witness a slow release rate of folic acid, beyond which the polymer's extensive degradation results in an increase in the vitamin's release rate. More than 82% of the vitamin is released by the end of the experiment [105].
Alborzi et al investigated the preparation and use of sodium alginate-pectin-poly(ethylene oxide) electrospun fibers as a stabilizing carrier for folic acid against degradation in acidic conditions and light. Such carrier was found to achieve folic acid retention close to 100% when stored at pH 3 in the dark for 41 days. The release studies showed that minimal folic acid (about 21%) was released at pH 3, but the release was significantly higher at pH 1.2 (65%). Nearly 97% of folic acid was released in water at pH, 7.8, but in simulated intestinal pH at the same pH resulted unexpectedly in only 41% release [58].

Vitamin B6 loading in clays and polymers was much less reported in the literature than folic acid. In a study by Joshi et al., vitamin B6 was intercalated in montmorillonite (MMT), a cationic clay of the class of phyllosilicates. The adsorption kinetics of vitamin B6 on MMT and the effects of changing pH, temperature and initial vitamin concentration on adsorption were studied. The adsorption process was found to be rapid, reaching equilibrium after 15 minutes. Temperature changes did not have a significant effect, whereas lower pH increased intercalation level. Optimizing the reaction conditions results in vitamin B6 loading of 13.9 mg/g MMT. *In-vitro* release studies showed that 67% and 87% of vitamin B6 were released from the MMT-vitamin hybrid in gastric (pH 1.2) and intestinal (pH 7.4) fluids respectively [106]

In another study, by Kevadiya and Joshi et al., vitamin B6-intercalated MMT was further incorporated in alginate hydrogel to control the vitamin release. Effects of pH and the vitamin's concentration on the intercalation process were studied. The maximum amount intercalated corresponded to 139 mg/g of MMT. Vitamin B6-intercalated MMT-alginate composites exhibited the highest encapsulation efficiency as compared to either the polymer or clay alone: about 90%, 28% and 87% (w/w) respectively. Release studies in phosphate buffer at pH 7.4 showed that the MMT-alginate composite controlled the vitamin's release, where only 44% of the vitamin was released along 9 hours [11].

Chapter 3. Theoretical Background

This chapter presents the characterization techniques used in this research. X-ray diffraction, infrared spectroscopy and ultraviolet/visible spectroscopy are based on the interaction of electromagnetic radiation with materials. The scattered, transmitted or absorbed radiation is studied to infer qualitative and quantitative information on the material investigated. On the other hand, nitrogen gas adsorption analysis, utilizes knowledge from the physics of gas adsorption to deduce information on the physical properties of solid materials.

3.1 X-ray Diffraction (XRD)

XRD is a structure-determination technique that is based on the *diffraction* of X-radiation when it interacts with crystalline solids. X-rays are high-energy electromagnetic waves of wavelength (λ) values in the range of 10-10^{-3} nm, corresponding to energies of 100 eV up to 10 MeV. X-rays are produced when a high-energy beam of electrons bombards a metal target. When the kinetic energy of the incident electron beam is sufficiently high, it induces an excitation in the target metal atoms, where an inner shell electron is ejected leaving behind an electron hole. As a higher-energy electron fills such electron hole to re-stabilize the metal atom, an X-ray photon, of energy equal to the difference between both energy levels, is emitted [107, 108]. The type of X-ray photons produced is named after the shell it was ejected from, as shown in figure 3-1.

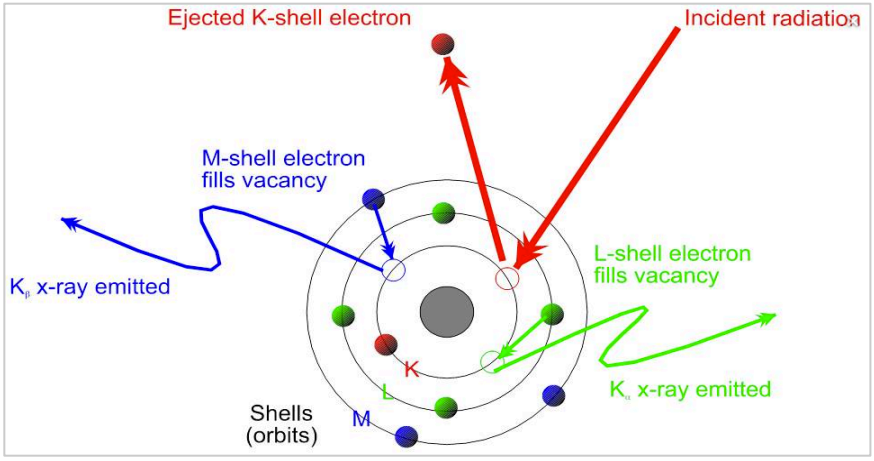

Figure 3-1. A schematic illustration of X-ray emission from metal atoms [104].

3.1.1 Basic principles

Upon the incidence of electromagnetic radiation on a material, its electric field component momentarily perturbs the electrons of the material's constituent atoms. The electrons oscillate with respect to their heavier nuclear core, causing a periodic polarization of the particles. As the atoms relax to their original state, the energy of such polarization is re-emitted in all directions as radiation of the same frequency as that of the incident radiation. When X-rays scatter off the different planes of atoms (or 'scattering units') of a material with

a long-range periodicity, i.e. crystalline, interference of the scattered radiation waves takes place both constructively and destructively. This happens because the distances between the scattering units of a crystal are of the same order of magnitude as the λ of the incident X-radiation. The intensity of the diffracted beam is a function of the positions of the atoms in the scattering unit and the relative orientation of the crystal to the incident beam's direction. W. L. Bragg defined the conditions that guarantee that the scattered X-ray waves be in-phase for constructive interference to occur and for the diffraction beam to be detected. Such conditions are defined by Bragg's law:

$$n\lambda = 2dsin\theta \qquad \textbf{(3- 1)}$$

n is an integer, λ is the wavelength of the incident X-radiation, *d* is the distance between planes in the crystal and *θ* is the angle between either the incident or the reflected beam and the normal plane as shown in figure (3-2). According to Bragg's law, constructive interference of the scattered X-rays only occurs when their path length difference is an integral multiple of the X-ray's wavelength. Otherwise, destructive interference occurs [107, 108, 110].

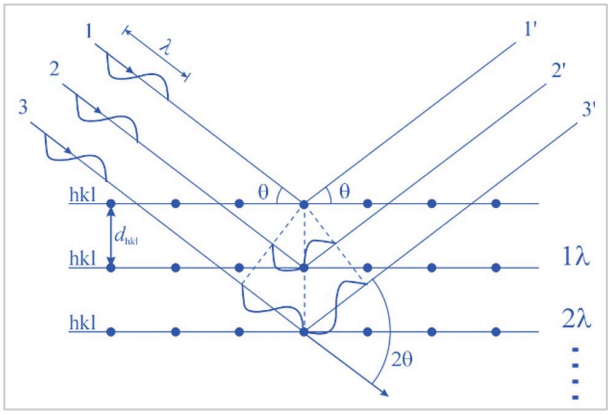

Figure 3-2. A schematic illustration of the conditions fulfilling constructive interference as defined by Bragg's law [111].

Exposing a crystalline material to X-radiation results in a diffraction pattern, which shows regions of high and low intensities, reflecting the incidences of constructive and destructive interferences, respectively. The diffraction pattern is specific to the crystalline material and thus enables the identification of the crystal structure. In order to relate the diffraction pattern to the crystal structure of a material, the understanding of some fundamentals of crystallography is needed. A *crystal* comprises repetitions of a basic structural motif, which can be an atom, a molecule, an ion, or a group of any of them. The theoretical construct representing the three-dimensional arrangement of these motifs in space is referred to as the *space lattice*. Joining neighboring lattice points into parallelepiped shapes enclosing each repetitive structural motif constitutes the *unit cell.* A unit cell is the smallest repetitive region

in the space lattice that can construct the entire crystal by translational displacements. The unit cell is described by unit cell parameters: the lengths of its sides a, b and c, and the angles between them α, β and γ [108, 112]. An example of a unit cell is shown in figure 3-3.

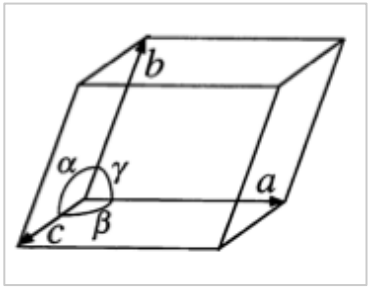

Figure 3-3. An example of a unit cell in a crystal [108].

In order to characterize the spacings of the lattice points, which eventually imply structural information on the investigated crystal, describing and labeling the different planes in a crystal lattice is needed. This is carried out using Miller indices, which are denoted by (*hkl*), and they designate the reciprocal of the intersection distances of the plane with the crystallographic axes. According to the crystal system that the investigated material belongs to, the inter-planar distance *d* can be calculated from equations that relate the Miller indices (*hkl)* and the lattice parameters to *d*, based on Bragg's law [108, 112].

3.1.2 Application

The basic components of an X-ray diffractometer are the X-ray source, X-ray filter, a goniometer, a detector, and a signal processor. The X-ray source is usually an X-ray tube, with the metal target typically being tungsten, molybdenum, or copper. Their respective wavelengths are shown in table (3-1). Filters are used to select the desired wavelength range.

Table 3-1. Examples of metal anodes used in common X-ray sources and their wavelengths [113, 114].

X-ray Source Metal Anode	Wavelength λ (Å) - Kα
Tungsten	0.20899
Molybdenum	0.71073
Copper	1.54184

The goniometer is the central component of the diffractometer and contains the sample holder at its center. It is connected to the detector and the X-ray source by two arms. Both the source and the detector lie on the circumference of a circle. The goniometer controls the mechanical motions of the specimen and the detector with respect to the source to satisfy

Bragg's law and enable the collection of the diffraction signals. Studying the diffraction of polycrystalline materials by XRD utilizes the Debye-Scherrer method, where the material, in powder form, is exposed to a monochromatic X-radiation. The powdered sample contains crystallites with a multitude of orientations and thus the monochromatic radiation will be diffracted by the ones of which orientation satisfies Bragg's law. The X-ray source is mostly stationary, whilst the specimen and the detector are rotated by angles θ and 2θ respectively to ensure the detection of the diffracted radiation (figure 3-4). The results of an X-ray diffraction experiment are plotted as 2θ versus intensity, as shown in figure 3-5. The intensity of a diffraction peak reflects the number of 'scattering units' that exist in a particular plane, and it is commonly expressed as counts per second. Powder diffraction techniques can be used for the identification of samples by comparing their diffraction lines (their positions and intensities) with those in a databank, in addition to determining phase diagrams and the relative amounts of phases in mixtures [107, 112, 115, 116].

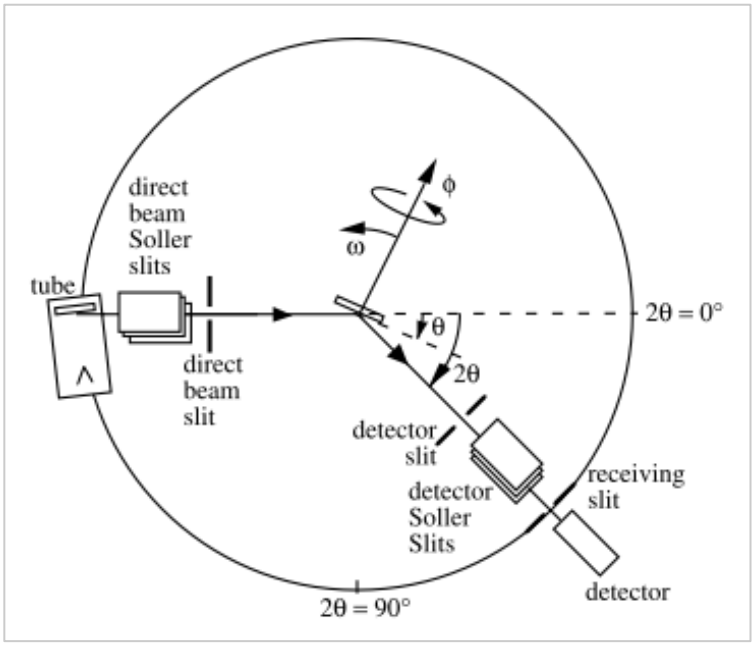

Figure 3-4. The Debye-Scherrer setup in the X-ray diffractometer [115].

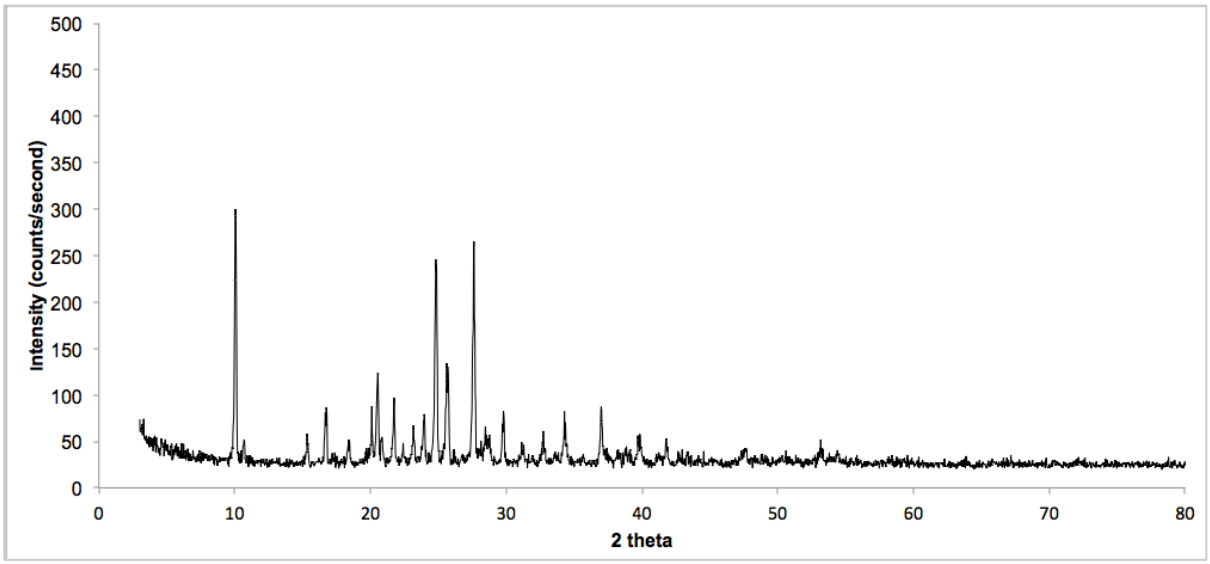

Figure 3-5. An example of a typical XRD pattern: Vitamin B6 powder.

3.2 UV/Visible Spectroscopy (UV/Vis)

UV/Vis spectroscopy is an absorption spectroscopy technique that finds widespread application in quantitative and qualitative analyses. The UV/Vis portion of the electromagnetic spectrum spans the range of wavelengths from 190-800 nm [117].

3.2.1 Basic principles

The energy of photons in the UV/Vis range corresponds to energy changes associated with transitions between electronic energy levels in atoms and molecules. For an atom, the absorption of radiation results in the excitation of electrons from one atomic orbital to another of higher energy. These transitions involve the *d* and *f* orbitals' electrons. For molecules though, the electrons are distributed in molecular orbitals. The electronic transitions in a molecule are typically from the **highest occupied molecular orbital (HOMO)** to the higher-energy **lowest unoccupied molecular orbital (LUMO)**, being the transition of the lowest energy cost [107, 117, 118]. A number of *selection rules* exist, which define whether an electronic transition is allowed or forbidden. These rules have to do with factors such as the spin quantum number of the excited electron, the number of electrons to be excited at one time, and symmetry considerations. The probability of a particular transition is reflected in a property inherent for each type of absorbing species called the *molar absorptivity* ε. Such property is independent of wavelength or solution-preparing parameters, but is dictated by the size of the absorbing species and the probability of the electronic transition involved. The value of ε and the concentration of the absorption species determine the magnitude of 'absorbance' by a particular sample. An empirical relationship:

the Beer-Lambert Law related the absorbance of a particular absorbing species at a particular wavelength to its concentration. The Beer-Lambert law is expressed as:

$$A = \log\left({}^{I_o}/_{I}\right) = \varepsilon c l \qquad \textbf{(3-2)}$$

A is the absorbance. I_0 and I are the values of radiation intensity before and after passing through the sample cell, respectively. c is the molar concentration of the solute and l is the length of the sample cell in cm [117].

3.2.2 Application

UV/Vis spectroscopy is a very useful utility for both quantitative and qualitative analyses of samples. A typical spectrometer comprises a light source, a monochromator, a sample holder, a detector and a readout device. Two light sources exist in the spectrometer: usually a deuterium or a hydrogen lamp for the UV wavelengths and a tungsten lamp for the visible wavelengths. The monochromator's function is to resolve the radiation beam into its component wavelengths. A system of slits lies in the beam's pathway to focus the wavelength-of-interest onto the sample cell. The detector receives the transmitted light and records its intensity. The sample container must be fabricated of a material that does not absorb radiation of the wavelengths used. Glass or plastic cells are used in the visible range whereas quartz cells are used in the ultraviolet range. There are two setups for UV/Vis spectrometers: single-beam and double-beam setups. In a single-beam spectrometer, the reference and the sample are placed in the measurement cell one after the other, and only a single beam of radiation emanates from the source and passes through each, one at a time. In a double-beam spectrometer, the light from the source is split into two beams, which pass into the reference and the sample cells simultaneously. The double-beam spectrometer offers the advantage of compensating for the short-term electrical fluctuations and other irregularities in the source, and detector. Single-beam instruments are only advantageous when single-wavelength measurements are needed. The output of a spectroscopic run is a plot of absorbance versus wavelength, as shown in figure (3-6), which shows the absorption spectrum of vitamin B6 (pyridoxine) [107, 117, 119].

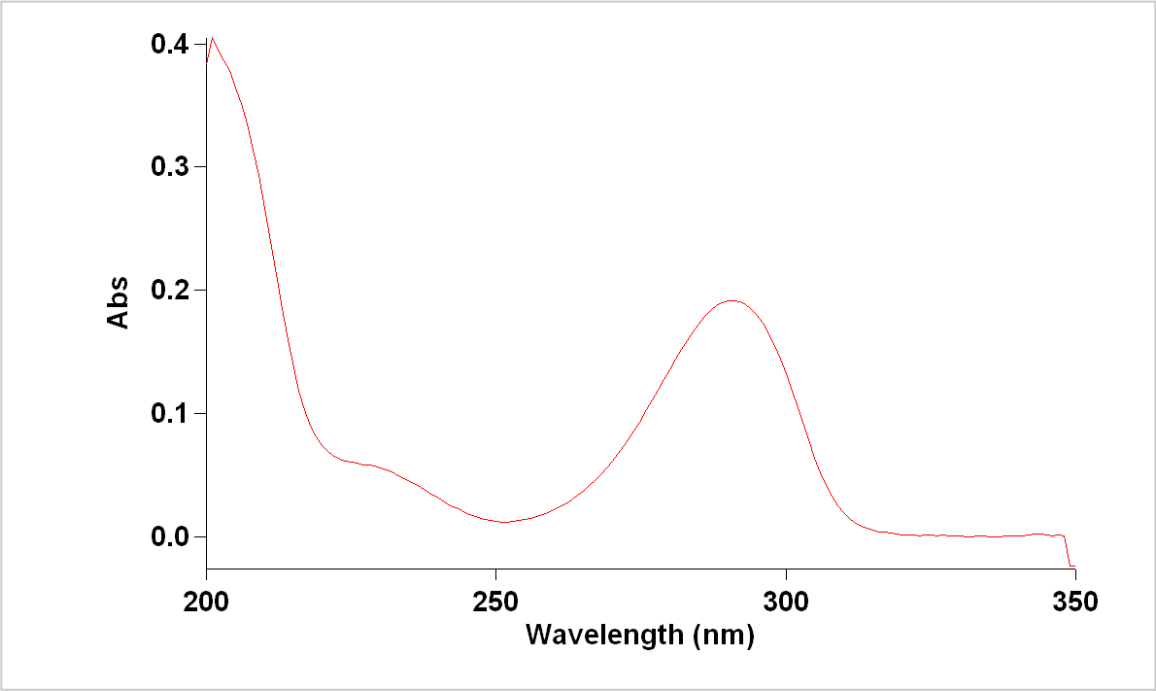

Figure 3-6. An example of a typical UV spectrum: vitamin B6 solution.

Analytical measurements are done at λ_{max}, since it is associated with the greatest change in absorbance per unit concentration, and thus offers maximal sensitivity. It is more commonly employed for quantitative purposes after establishing the relationship between absorbance and concentration by calibrating a series of standards against their respective absorbance values. The concentrations of the standards must span a wide range so that the relationship established can accurately calculate the unknown concentration of the analyte measured [107, 117, 119].

3.3 Fourier transform-Infrared spectroscopy (FT-IR)

3.3.1 Basic principles

The infrared (IR) region of the electromagnetic spectrum spans the range of wavelengths from 0.78 μm to 1000 μm (or wavenumbers: 12800 cm^{-1} to 10 cm^{-1}). The IR spectral region is subdivided into near, middle and far infrared radiation. Most analytical applications make use of the middle infrared region from 2.5-15 μm (4000-670 cm^{-1}). Infrared spectroscopy, like UV/Vis spectroscopy, is an absorption spectroscopic technique, where the IR radiation is absorbed resulting in the excitation of the absorbing species (exclusively molecular samples) from the ground state to the excited state. IR, being of a lower energy than UV/Vis radiation, results in transitions between energy states of smaller energy difference than those between electronic energy levels. These correspond to the vibrational and rotational energy levels of a

molecule. Like electronic energy levels, the energy of molecular vibrations and rotations are quantized: only discrete energy states can exist for each. A molecule absorbs radiation in the infrared region only if the frequency of the photons matches that of a natural vibrational frequency of the molecule, provided that such vibration results in a net change in the molecular dipole moment. Such condition is fulfilled in molecules in which the charge distribution on vibration is asymmetric. In molecules, the atoms can move relative to one another in two types of vibrations: stretching and bending [107]. Figure (3-7) shows examples of such vibrational modes.

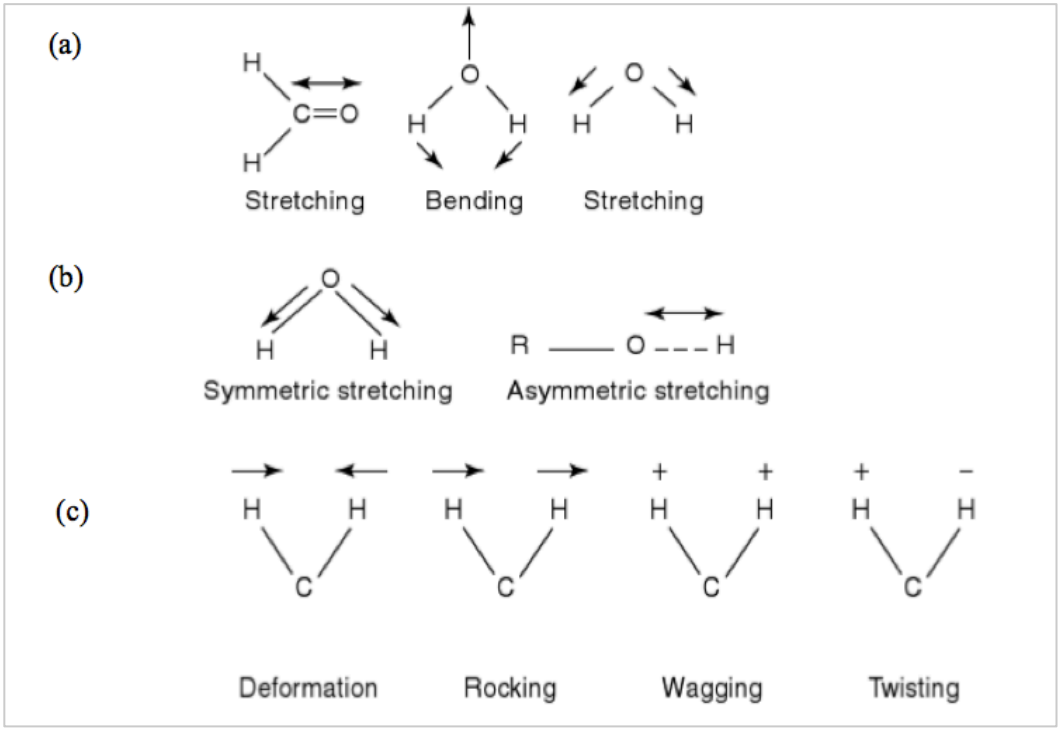

Figure 3-7. Types of bond stretching and bending vibrational modes [120].

To understand the characteristics of molecular vibrations, a molecule can be modeled as a system of masses connected to each other by springs, representing atoms and bonds, respectively. The displacement of one of the masses connected by the spring results in *simple harmonic oscillation,* of which vibrational frequency can be described by the equation:

$$\boldsymbol{\nu_m = \frac{1}{2\pi}\sqrt{\frac{k}{\mu}}} \qquad \textbf{(3-3)}$$

ν_m is the vibrational frequency. k is the force constant that is dictated by the stiffness of the spring, and is relevant to the type of the bond. μ is the reduced mass representing masses m_1 and m_2 connected by the spring. The reduced mass is calculated as: $\mu = \frac{m_1 m_2}{m_1 + m_2}$. For determining the number of vibrational modes in a polyatomic molecule of N atoms, each atom is described by three coordinates in space. Each coordinate represents one degree of freedom for each atom, giving the whole molecule 3N degrees of freedom. In order to

calculate the degrees of freedom attributable to vibrations, 3 translational and 3 rotational degrees of freedom are excluded, resulting in 3N-6 vibrational degrees of freedom (3N-5 for linear molecules which only have 2 rotational degrees of freedom). The number of stretching modes is as same as the number of bonds in the molecule, and the rest are bending vibrations [107, 120, 121].

3.3.2 Application

An IR-spectrometer comprises the basic components of other spectroscopic instruments: a source of radiation, monochromator, sample compartment, detector and readout device. The source of IR radiation is typically an inert metal that is electrically heated to temperatures of 1500-2000 °K. The sample must be placed in an IR-inactive compartment or 'matrix'. One of the common techniques of handling solid samples is compressing them into pellets with potassium bromide (KBr) as the IR-transparent matrix. Only a milligram or less of the finely ground sample is mixed with about 100 mg of dried KBr powder by the use of a mortar and pestle. The solid mixture is then compressed in a special die at high pressure into a transparent disk, which is then analyzed in the sample compartment of the spectrometer. Modern IR instrumentation employs Fourier Transform: a group of mathematical methods that allows for the simultaneous analysis of multiple frequency components in a single operation. IR spectrometers utilizing Fourier Transform (FT-IR) offer superior speed, accuracy and sensitivity when compared to wavelength dispersive spectrometers. The output of an FT-IR spectroscopic run is a spectrum plotted as amplitude (corresponding to either the extent of transmittance or absorbance) versus the frequency of radiation. The frequency is more commonly expressed in wavenumber units ($1/\lambda$, cm^{-1}) and is usually plotted against % transmittance [107, 120-122]. An example of a typical FTIR spectrum is shown in figure (3-8).

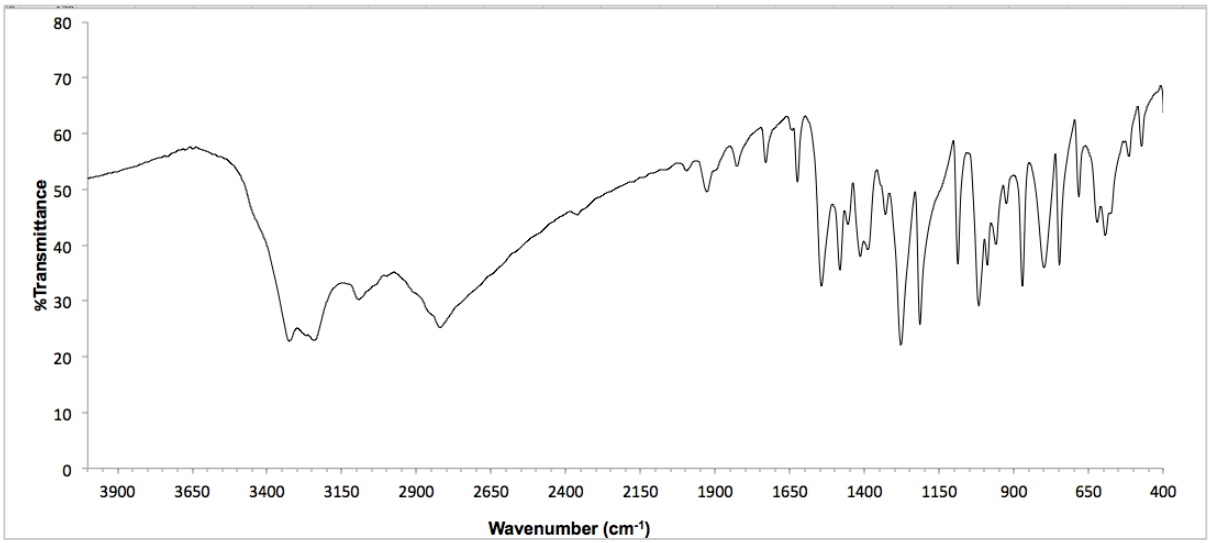

Figure 3-8. An example of a typical FT-IR spectrum: Vitamin B6 powder.

IR spectra allow for qualitative analyses. Different ranges of wavenumbers, the shape, and the intensity of the peaks have been empirically correlated with particular functional groups and recorded in *correlation charts,* which enable qualitative analyses and identification chemical groups in a material. If absorbance is plotted against wavenumber, the area/height of the peak is directly proportional to the molecular concentration and Beer's law applies, making FT-IR spectroscopy a useful quantitative tool as well [107].

3.4 Nitrogen Gas Adsorption and the BET Theory

3.4.1 Basic principles

Nitrogen gas adsorption is one of the most commonly used techniques for the characterization of porous solids. The principle of such technique is based on exploiting the adsorption behavior of gases on the external and internal surfaces (pores) of a material to deduce information on its physical properties. *Adsorption* refers to the attachment of atoms or molecules to a surface, either via physical forces (physisorption) or chemical bonding (chemisorption). The substance that adsorbs is called the *adsorbate* and the substance it attaches to is called the *adsorbent* or the *substrate* and is mostly a solid. The reverse of the process is termed *desorption*. Nitrogen, being a neutral molecule, undergoes physisorption. Physisorption is based on weak van der Waals forces, it has a low degree of specificity for the adsorbent and the adsorbate retains its identity both in adsorbed and desorbed states [112, 123-125].

At the interface between the two phases, the free gas and the adsorbed gas are in dynamic equilibrium state:

$$A(g) + M(surface) \rightleftharpoons AM(surface)$$

The extent of adsorption is expressed in terms of the ratio between the number of adsorption sites occupied to the number of those available. Such ratio is quantified by the fractional coverage θ corresponding to V/V_∞, where V is the volume of the adsorbed species and V_∞ is the volume of the adsorbate corresponding to complete monolayer coverage. The rate of change of the fractional coverage due to adsorption is proportional to the partial pressure p and the number of unoccupied sites, whereas that of desorption is proportional to the number of adsorbed species [112]. The relationship between the amount of gas adsorbed by a unit mass of the adsorbent and the equilibrium pressure p (or relative pressure: p/p^o, where p^o is the saturation vapor pressure above the layer of the adsorbate) at constant temperature is called the adsorption isotherm. The adsorption isotherm reflects the behavior of the adsorbent when exposed to the adsorbing species, and thus infers information on the nature of its external and internal surfaces. The internal surfaces refer to the pores in porous solids, which can take various forms: open, closed, interconnected, bottleneck or blind (figure 3-10). Pores can be classified according to their size (i.e. the width of two opposite walls) into micropores (< 2 nm), mesopores (2-50 nm) and macropores (> 50 nm). Enhanced adsorbate-adsorbent interactions are observed in micropores of molecular dimensions, where adsorption in such pores is associated with an increase in the adsorption energy and a decrease in the relative pressure at which they are filled [123].

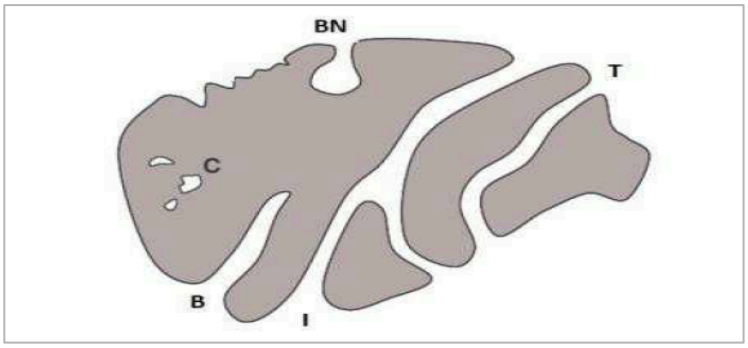

Figure 3-9. An illustration of the different types of pores that may be encountered in a porous material: C – closed pores, B – blind pores, BN – bottleneck pores, T – through pores, and I – interconnected pores [126].

3.4.1.a Types of Isotherms

The IUPAC (International Union of Pure and Applied Chemistry) has grouped the most empirically encountered isotherms into six types, depicted in figure 3-10.

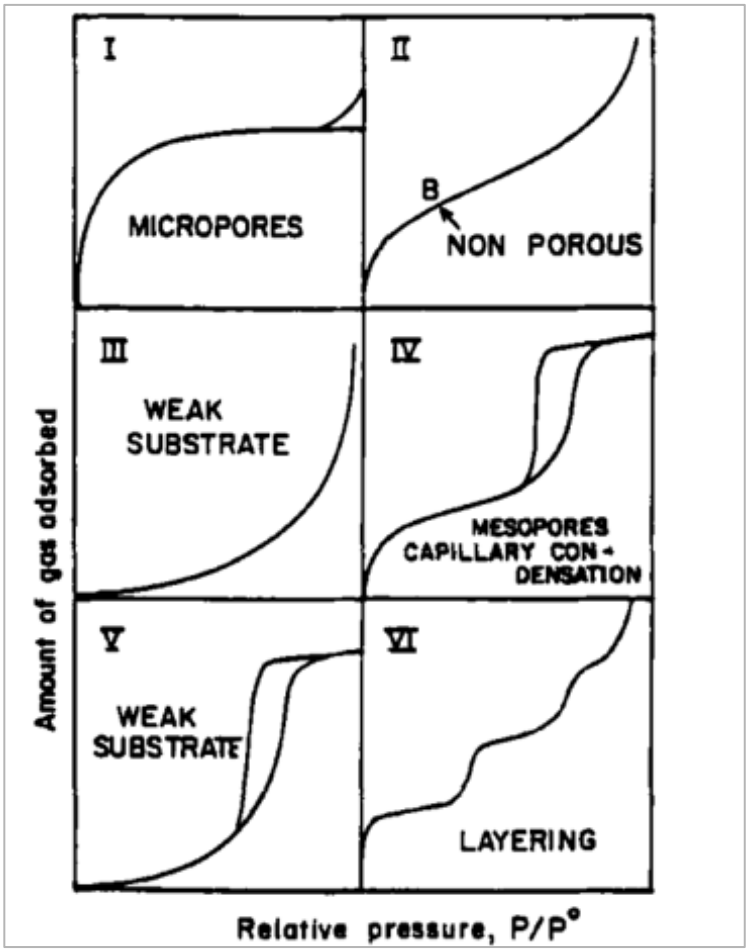

Figure 3-10. Types of isotherms as classified by the IUPAC [127].

The simplest isotherm is the Langmuir isotherm (Type I), which is valid under three assumptions: 1. The adsorption is restricted only to monolayer adsorption, 2. All adsorption sites are equivalent (flat surface), 3. No interaction exists between adsorbing molecules. In Type I isotherm, at low p/p^o values, the amount of adsorbed gas increases sharply until it reaches a plateau as p approaches p^o. The narrow range of p/p^o values for which adsorption occurs indicates the presence of micropores of a limited pore size distribution and a very small external area. Stephen Brunauer, Paul Emmett, and Edward Teller introduced a number of simplifying assumptions to the Langmuir isotherm. According to their theory (the BET theory), a monolayer of adsorbates can act as substrate for multilayer adsorption. Multilayer adsorption mostly occurs when the temperature is close to the boiling temperature of the

adsorbate gas at the operating pressure. Such adsorption can be viewed as some sort of condensation, where the extensive attraction between the adsorbate molecules causes them to condense into a liquid-like film [112, 123].

Types (II)-(VI) isotherms are understood in the context of multilayer adsorption. In Type (II), the isotherm shows that progressive adsorption takes place with increasing p/p^o until point B, which lies at the beginning of the quasi-linear part of the isotherm, marking the completion of monolayer adsorption and the start of multilayer stacking of the adsorbate. The coordinates at point B represent the amount of adsorbate required to cover a unit mass of the solid with monolayer coverage. Such amount can be used to calculate the total surface area of the adsorbent, assuming a close-packed arrangement of the adsorbate molecules. Type (II) isotherm is typical of nonporous and macroporous adsorbents, which allow for infinite adsorption at high p/p^o values. Desorption from such an adsorbent at temperatures at or below the adsorbate's boiling point, exhibits complete reversibility. Adsorption hysteresis refers to the condition where the amount adsorbed by a substrate does not reach the same level by adsorption and desorption processes at a given equilibrium pressure. The absence of adsorption hysteresis is compliant with the fact that structures associated with such isotherm are open, stable structures undergoing normal monolayer-multilayer adsorption. Type (IV) isotherm's first part is somewhat comparable to Type (II), however, it levels off at high p/p^o values, which indicates finite adsorption. Such isotherm is observed with mesoporous materials. Type (IV) isotherm comprises a hysteresis loop: the lower branch represents the adsorption phase, while the upper branch represents the desorption one. Such hysteresis loop is associated with mesoporous materials and it arises as a result of the filling and emptying of the mesopores by capillary condensation. The multi-molecular layers of gas adsorbed on the opposite walls of the mesopore eventually come together and interact condensing into liquid below the gas's p^o. Type (III) and Type (V) isotherms are typical of situations where adsorbate-adsorbent interactions are weak in non-/macro-porous and meso-porous solids respectively. Type (VI) shows a stepwise isotherm, associated with layer-by-layer adsorption upon highly uniform surfaces. Types (III), (V) and (VI) are rarely encountered [112, 123, 125, 127].

3.4.1.b Types of Hysteresis Loops

Hysteresis loops arise due to capillary condensation within the porous solid. Therefore, the shape of the hysteresis loop in an isotherm is dependent on the textural properties of the nanoporous material. The IUPAC empirically classified hysteresis loops into four types (H1 – H4), depicted in figure 3-11.

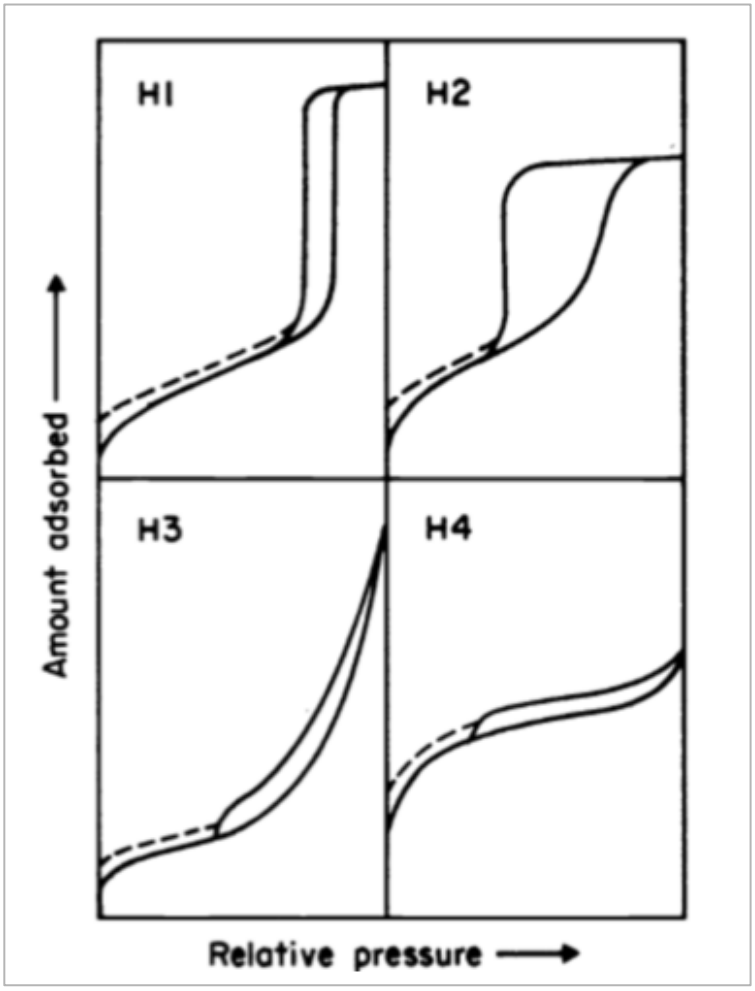

Figure 3-11. Types of hysteresis loops as classified by the IUPAC [128].

Type H1 hysteresis loops are often encountered with materials comprising uniform cylindrical pores with narrow pore size distribution. H2 loops are associated with materials containing a complex network of interconnected pores of different sizes and shapes. Isotherms with H3 hysteresis loops exhibit infinite adsorption properties at high p/p^{o} values. Such isotherms are usually considered a variant of Type (II) and are referred to as pseudo-Type (II) or Type (II-b) isotherms. H3 loops are associated with materials consisting of aggregates of layered particles or slit-shaped pores of non-rigid nature. H4 loops are

encountered with complex materials containing both meso- and micro-pores. Both H3 and H4 loops are characterized by a 'shoulder' in the desorption branch near the loop closure point [123, 128-130].

3.4.2 Application

Despite its oversimplified view of monolayer-multilayer adsorption, the BET theory is established as the standard method for surface area determination of porous solids from gas adsorption data. The BET equation is as follows:

$$\frac{{}^{p}/_{p^o}}{V\left(1-{}^{p}/_{p^o}\right)} = {}^{1}/_{V_m C} + \frac{C-1}{V_m C}\left(p/p^o\right) \qquad \textbf{(3-4)}$$

p^o is the saturation vapor pressure above the layer of adsorbate while p is the partial vapor pressure of the gas at equilibrium. V is the volume of adsorbed gas and V_m is the volume of complete monolayer coverage, both measured at standard temperature and pressure. C is a constant (BET constant). The value of C increases when the enthalpy of desorption from a monolayer is greater than the vaporization enthalpy of the liquid adsorbate [123].

For BET-nitrogen adsorption analysis, the solid sample (a minimum of 0.5 g) is placed in a glass cell. Before exposing the material to nitrogen, it needs to be degassed under vacuum and high temperature, in order to remove any pre-adsorbed gases or contaminants that may interfere with the analysis. It is recommended by the IUPAC that the sample must be degassed for at least 16 hours. After degassing, the sample cell is moved to the analysis compartment. Low temperature is maintained by using liquid nitrogen (77.4 K) in order to maximize the interaction between the gas and the sample and for a measurable extent of adsorption to take place. As the analysis process starts, a known 'amount' of nitrogen gas is released and the pressure increases gradually inside the sample cell until saturation is reached. The adsorption process is monitored by highly accurate and precise pressure transducers. After the adsorption process is complete, the sample is then heated in order to force desorption of nitrogen from the material and quantify it. In order to obtain information on the surface area of the material, single and multi-point-based measurements are plotted. In multipoint plots, the value of V is measured for at least 3 values of p/p^o and then the quantity $(\boldsymbol{p/p^o})/(\boldsymbol{V}\,(\boldsymbol{1-p/p^o})$ from equation 3-4 is plotted against p/p^o for such data points. This plot should produce a straight line in the range of $0.05 < p/p^o < 0.3$. The slope of the straight line is $(\boldsymbol{C-1})/(\boldsymbol{V_m\,C})$ and its intercept value is $\boldsymbol{1/(V_m\,C)}$ [131].
Having deduced the values of C and V_m from the slope and the intercept, the BET surface area (aBET) can be calculated from the formula:

$$\boldsymbol{aBET = \frac{V_m N \sigma}{M_v . m}} \qquad \textbf{(3-5)}$$

N is Avogadro's number, σ is the cross-sectional area occupied by the nitrogen molecules in

the adsorbed monolayer, M_v is the molar volume of the gas and m is the mass of the sample [113, 131, 132].
The BET model complies with experimental observations moderately well over a defined range of pressures. Above and below such pressure range it over- and under- estimates the extent of adsorption, respectively [112]. The model ignores surface inhomogeneities and lateral interactions between the adsorbate molecules. Such interactions result in high-energy sites being occupied at lower p/p^o and therefore explain the deviation of BET plots from linearity at $p/p^o < 0.05$. The model also does not account for the polarization effects that increase the heat of adsorption as successive layers adsorb upon one another, which justifies the failure of the BET equation at $p/p^o > 0.3$ [133].

For porosity studies, the shapes of the hysteresis loops give an indication on the type of pore structure in terms of its shape and uniformity. Pore size distribution (PSD) can be calculated by assuming a model for pore filling that relates the condensation pressure to the pore width. A thermodynamic model that is commonly employed for such purpose is the Kelvin equation:

$$\ln {}^{p}/_{p^o} = -2\gamma RT\rho_l H \qquad \textbf{(3-6)}$$

p is the pressure at which the condensation starts in the slit/pore of width H, R is the ideal gas constant, γ is the surface tension of nitrogen and ρ_l is the liquid density, at absolute temperature T. Applying Kelvin equation gives accurate values for large pores at low temperatures, but it fails when applied to narrow pores. The rising portion of an isotherm past the multilayer stacking region indicates the onset of adsorption within pores (capillary condensation). When the plateau is reached (such as in Type (IV) isotherm), this marks the filling of mesopores at high relative pressure values and from this value the volume of such pores is calculated. The BJH (Barrett-Joyner-Halenda) analysis is considered the most popular computational method, which utilizes the corrected Kelvin equation for the purpose of pore size distribution analysis [127, 134, 135].

Chapter 4. **Materials and Methods**

4.1 Materials

All materials used in this research are of analytical grade, they were purchased and used without further purification. Zinc nitrate hexahydrate (98%), aluminum nitrate nonahydrate (≥98%), pyridoxine hydrochloride (≥98%), sodium hydroxide (≥98%), hydrochloric acid (37%), sodium chloride (≥99.5%), low viscosity alginic acid sodium salt (from brown algae) and sodium phosphate monobasic dihydrate (98-100.5%) were purchased from Sigma-Aldrich (Germany). Extra-pure anhydrous calcium chloride (95%) was purchased from Scharlau (Spain). Folic acid (97%) was purchased from Alfa Aesar (Germany). Potassium dihydrogen orthophosphate (99-101%) was purchased from Adwic (Egypt). Fasted and Fed State Simulated Intestinal and Stomach Fluids (FaSSIF, FeSSIF & FaSSGF) powder was purchased from Biorelevant.com (United Kingdom). Deionized water was exclusively used for the preparation of the aqueous solutions and for precipitate washing.

4.2 Synthesis of Vitamin-Intercalated and Pristine Zn/Al-LDHs

Both pristine and vitamin-intercalated Zn/Al-LDHs were prepared by co-precipitation under low supersaturation conditions, based on work conducted in the same laboratory by Foraida and Ramadan, with a number of modifications [136]. Experimental parameters such as the Zn^{+}/Al^{3+} ratio, the reaction pH and the concentrations of both the precursor mixed metal cations solution and the vitamin solution were systematically varied for each vitamin until an optimized set of conditions leading to successful intercalation was obtained. Pristine LDHs (NO_3-intercalated Zn/Al LDHs) were prepared under the same conditions to serve as control specimens for comparison with the vitamin-loaded LDHs.

4.2.1 Synthesis of Vitamin B6-intercalated LDHs (B6-LDHs)

A Zn^{2+}/Al^{3+} mixed cations solution was prepared by thoroughly mixing 30 ml of 0.1 M $Zn(NO_3).6H_2O$ and 10 ml of 0.1 M $Al(NO_3)_3.9H_2O$ aqueous solutions corresponding to Zn^{2+}/Al^{3+} ratio of 3, and total metal cations concentration of 0.1 M. 0.617 grams of vitamin B_6 (~ 0.003 moles) were dissolved in deionized water and the volume completed to 50 ml, resulting in a vitamin solution concentration of 0.06 M. The vitamin solution was placed in a 600 ml-beaker and was magnetically stirred at 1000 rpm. N_2 gas was bubbled into the solution throughout the experiment to expel atmospheric CO_2 from the reaction medium, which would otherwise dissolve as CO_3^{2-} ions and compete with the vitamin for intercalation, by virtue of its high affinity to the brucite-like sheets. The reaction starts as the Zn^{2+}/Al^{3+} mixture is slowly added to the vitamin solution in the beaker from a burette (at a flow rate of ~ 2.5 $ml.min^{-1}$). The pH was gradually raised by the drop-wise addition of 2 M NaOH, and was maintained at 8 ± 0.3. A white precipitate was formed, and the suspension was kept stirring under N_2 bubbling for ~ 15 minutes after the reaction. It was then filtered and washed

thoroughly by re-dispersion in 40 ml of deionized water. After re-filtration, the precipitate was placed in a porcelain dish and left to dry in the oven at 80°C for 21 hours. The dried precipitate was ground and sieved with a 150 μm-opening sieve into a uniform fine powder. The yield of such process was not sufficient for the subsequent steps, so the reaction was repeated 12 times under the same conditions, and the solid products were homogeneously mixed using a tubular mixer set at 96 rpm for 45 minutes.

4.2.2 Synthesis of Folic acid-intercalated LDHs (Fa-LDHs)

A Zn^{2+}/Al^{3+} mixed cations solution was prepared by thoroughly mixing 15 ml of 0.3 M $Zn(NO_3).6H_2O$ and 15 ml of 0.1 M $Al(NO_3)_3.9H_2O$ aqueous solutions, corresponding to Zn^{2+}/Al^{3+} ratio of 3, and total metal cations concentration of 0.2 M. 1.324 grams of folic acid (~ 0.003 moles) were completely dissolved in a dilute NaOH solution (pH 7) and the volume completed to 50 ml, resulting in a vitamin solution concentration of 0.06 M. The folic acid solution was placed in a 600 ml-beaker and was magnetically stirred at 1000 rpm. The reaction starts as the Zn^{2+}/Al^{3+} mixture is slowly added to the vitamin solution in the beaker from a burette (at a flow rate of ~ 2.5 $ml.min^{-1}$). The pH was gradually raised by the drop-wise addition of 2 M NaOH, and was maintained at 7 ± 0.3. An orange precipitate was formed, and the suspension was kept stirring under N_2 bubbling for ~ 15 minutes after the reaction. It was then filtered and washed thoroughly by re-dispersion in 70 ml of deionized water. After re-filtration, the precipitate was placed in a porcelain dish and left to dry in the oven at 80°C for 21 hours. The dried precipitate was ground and sieved with a 150 μm-opening sieve into a uniform fine powder.

4.2.3 Synthesis of pristine LDHs (pLDHs)

The pristine LDHs are the NO_3-intercalated form of the Zn/Al-LDHs, prepared under the same conditions used for intercalating each vitamin.
For the synthesis of the control LDH of the B6-LDH sample, a Zn^{2+}/Al^{3+} mixed cations solution comprising 30 ml of 0.1 M $Zn(NO_3).6H_2O$ and 10 ml of 0.1 M $Al(NO_3)_3.9H_2O$ was placed in a 250-ml beaker. The mixture was magnetically stirred at 1000 rpm, and N_2 gas was bubbled into the solution throughout the experiment to expel CO_2. The pH was slowly adjusted to 8 ± 0.3 by the drop-wise addition of 2 M NaOH. The total metal cations concentration in the precursor mixture is 0.1 M and thus this control sample is labeled: **pLDH-0.1**. The same procedure was followed for preparing the control LDH of the Fa-LDH sample, except that the metal cations mixture comprised 15 ml of each of 0.3 M $Zn(NO_3).6H_2O$ and 0.1 M $Al(NO_3)_3.9H_2O$, and the pH was adjusted to 7 ± 0.3. The total metal cations concentration in the precursor mixture is 0.2 M and thus this control sample is labeled: **pLDH-0.2**.

Both suspensions were kept stirring for ~ 15 minutes after the reaction, they were then filtered, and thoroughly washed by re-dispersion in 40 ml and 70 ml deionized water for pLDH-0.1 and pLDH-0.2, respectively. The precipitates were re-filtered and dried in the oven at 80°C for 21 h in a porcelain dish. The dried precipitate was ground and sieved with a 150 µm-opening sieve into a uniform fine powder before further use. Table 4-1 summarizes the synthesis parameters for the vitamin-loaded and control LDHs.

Table 4-1. The synthesis parameters for vitamin-intercalated and pristine LDHs.

Sample	$[Zn^{2+}+ Al^{3+}]$	Vitamin/ Al^{3+}	pH of the reaction
B6-LDH	0.1 M	3	8±0.3
Fa-LDH	0.2 M	2	7±0.3
pLDH-0.1	0.1 M	-	8±0.3
pLDH-0.2	0.2 M	-	7±0.3

4.3 Loading Percentage Determination

The determination of the loading percentage of the vitamin-loaded LDHs was based on the method reported by Xiao et al. with some modifications [78]. A known amount of the vitamin-loaded LDH was dissolved in a specified volume of 2.5 M HCl and the volume was completed to 50 ml with phosphate buffer solution (6.8 g. of KH_2PO_4 dissolved in 1 liter of deionized water, adjusted to pH 6.8 by 2 M NaOH). The amount of vitamin loaded (both intercalated within and adsorbed externally upon the LDH layers) is determined by UV spectroscopy (λ_{max} = 290 nm for vitamin B6, and 300 nm for folic acid) according to calibration curves based on standard vitamin solutions prepared in the same way (figures A1-1 and A1-5 in Appendix 1). The loading percentage determination experiment was conducted in triplicate for each sample, and the average was calculated.

The loading percentage is calculated as follows:

$$Loading\ \% = \left(\frac{Weight\ of drug\ loaded}{Weight\ of\ LDH}\right) * 100 \qquad \textbf{(4-1)}$$

4.4 Preparation of Alginate/LDH (A/L) Composite Beads

Alginate/LDH composite beads were prepared by the ionotropic gelation of sodium alginate solution comprising dispersed LDHs in $CaCl_2$ solution. The concentration of the sodium alginate solution used and its flow rate into the gelation medium were optimized by trial-and-error so as to ensure the production of regular spherical beads, with a homogenous distribution of the entrapped LDHs. The molar ratio of alginate : Ca^{2+} ions in the gelation medium, was kept constant throughout the experiments, and it was set so as to ensure that the Ca^{2+} ions are present in excess.

Alginate/LDH (A/L) composite beads comprising B6-LDH, Fa-LDH and pLDH-0.1 (control beads) were prepared in three different alginate:LDH ratios (in order of increasing LDH content): 16:1, 10:1 and 4:1.

1.25 g of sodium alginate powder was added portion-wise to 30 ml of warm deionized water (50-60 °C), and was magnetically stirred until completely dissolved. According to the desired alginate:LDH ratio for the sample prepared, the corresponding weight of LDH was dispersed in 20 ml of deionized water under vigorous magnetic stirring (1200 rpm), for 15 minutes. The LDH dispersion was then added drop-wise to the sodium alginate (SA) solution, resulting in a final polymer concentration of 2.5% (w/v). The alginate/LDH dispersion was magnetically stirred (1200 rpm) for 30 minutes [21].

The gelling medium is 200 ml of 5% (w/v) $CaCl_2$ solution [21]. A peristaltic pump (Cole Parmer MasterFlex® L/S, USA) was used to add the alginate/LDH dispersion drop-wise to the $CaCl_2$ solution at a constant flow rate of 1.5 $ml.min^{-1}$. The dispersion was withdrawn at one end of the tubing connected to the pump, and dropped into the gently stirred $CaCl_2$ solution, from a height of ~ 3 cm, through a 1.1 mm-opening syringe attached to the other end of the tubing. As the alginate/LDH dispersion droplets come in contact with the $CaCl_2$ solution, they gel into regular spherical beads. The beads were cured for 20 minutes in solution, then filtered and washed 3 times with 50 ml of deionized water each. The beads were then left to dry at room temperature and pressure for 48 hours. LDH-free calcium alginate beads were also prepared following the same procedure and they were labeled A0.

Table 4-2 presents the different sample codes and summarizes the preparation conditions for each of them.

Table 4-2. A summary of the preparation conditions of the alginate/LDH composite beads.

	Sample Code	Alginate:LDH ratio	Sodium Alginate (g)	LDH (g)	Equivalent amount of vitamin (g)	Sodium Alginate and $CaCl_2$ solutions
B6	**B6-A/L16**	16:1	1.25	0.078	0.025	2.5% (w/v) Sodium Alginate solution (50 ml) 5% (w/v) $CaCl_2$ solution (200 ml)
	B6-A/L10	10:1	1.25	0.125	0.039	
	B6-A/L4	4:1	1.25	0.313	0.099	
Folic acid	**Fa-A/L16**	16:1	1.25	0.078	0.051	
	Fa-A/L10	10:1	1.25	0.125	0.081	
	Fa-A/L4	4:1	1.25	0.313	0.203	
Controls	**A/L16**	16:1	1.25	0.078	-	
	A/L10	10:1	1.25	0.125	-	
	A/L4	4:1	1.25	0.313	-	
	A0	1:0	1.25	-	-	

4.5 Entrapment Efficiency (EE) Determination

The entrapment efficiency of each of the composite beads was estimated by measuring the concentration of the vitamin leached in the $CaCl_2$ solution post gelation by UV spectroscopy (λ_{max} = 307 nm for vitamin B6, and 256 nm for folic acid), according to calibration curves based on standard solutions of each vitamin in 5% $CaCl_2$ (figures A1-2 and A1-6 in Appendix 1) [64, 137]. Subtracting the amount of leached vitamin from the amount theoretically loaded within the dispersed weight of vitamin-loaded LDHs reflects the amount of vitamin remaining entrapped within the composite beads. The entrapment efficiency is calculated as follows:

$$EE\% = \left(\frac{W_T - W_{CaCl2}}{W_T}\right) * 100 \qquad \textbf{(4-2)}$$

W_T is the theoretical amount of loaded vitamin and W_{CaCl2} is the amount of vitamin leached in $CaCl_2$.

4.6 *In-Vitro* Release Studies

The vitamin release behavior of B6-LDH, Fa-LDH and their respective A/L composite beads was studied in Biorelevant dissolution media of pH 1.6 and 6.5, simulating the gastric (BioSGF) and intestinal (BioSIF) environments, respectively. Biorelevant media comprise physiologically relevant components (e.g. phospholipids and bile salts) and hence afford a more realistic simulation of the gastrointestinal conditions [138]. The vitamin release from B6-LDH and Fa-LDH was studied in each dissolution medium separately as they almost completely dissolve in the acidic conditions of BioSGF. However, the B6- and folic acid-loaded composite beads were placed first in BioSGF for 2 hours, which is the approximate transit time of an oral dosage form in the stomach, then filtered and placed in BioSIF for 24 hours, to simulate the journey of the dosage form in the gastrointestinal tract.

4.6.1 Preparation of Biorelevant Dissolution Media

For the preparation of 1 L of BioSGF: 2 g of sodium chloride (NaCl) were dissolved in ~ 900 ml of deionized water. The pH was adjusted to 1.6 by concentrated hydrochloric acid (HCl) and the volume was then completed to 1 L by deionized water. 0.06 g of the Biorelevant media powder (FaSSIF, FeSSIF & FaSSGF) was dissolved in ~500 ml of the NaCl/HCl solution, and then the volume was completed to 1 L by the same solution.

For the preparation of 1 L of BioSIF: 0.420 g of sodium hydroxide (NaOH), 4.470 g of sodium phosphate monobasic dihydrate (NaH_2PO_4) and 6.186 g of sodium chloride (NaCl) were dissolved in ~ 900 ml of deionized water. The pH was adjusted to 6.5 by 1 N NaOH or 1 N HCl. The volume was then completed to 1 L by deionized water. 2.240 g of the Biorelevant media powder (FaSSIF, FeSSIF & FaSSGF) was dissolved in ~500 ml of the prepared buffer, and then the volume was completed to 1 L by the same solution.

4.6.2 In-Vitro Release Studies of B6

4.6.2.a In BioSGF

An amount of each of B6-LDH, B6-A/L16, B6-A/L10 and B6-A/L4 equivalent to 2.5 mg of B6 was weighed and placed in a glass bottle. The samples were suspended in 30 ml of BioSGF, to ensure sink conditions are applied. The stoppered glass bottles were placed in a water-bath shaker set at 37 °C and a shaking speed of 50 strokes/minute. 2-ml aliquots were withdrawn from each sample after: 10 minutes, 30 minutes, 1 hour and 2 hours. The withdrawn volume was replaced by 2 ml of fresh BioSGF at each interval. The concentration of the vitamin in the withdrawn aliquots is determined by UV spectroscopy (λ_{max} = 290 nm)

according to calibration curves calculated from standard solutions of B6 in BioSGF (figure A1-3 in Appendix 1).

4.6.2.b In BioSIF

After the 2-hour interval in BioSGF, the B6-A/L composite beads were filtered, blotted and carefully transferred, along with a new sample of B6-LDH, to another set of clean, labeled glass bottles containing 30 ml of BioSIF (sink conditions) and returned to the water-bath shaker under the same conditions. 2-ml aliquots were withdrawn from each sample after: 30 minutes, 1, 2, 4, 6, 20 and 24 hours in BioSIF. The withdrawn volume was replaced by 2 ml of fresh BioSIF at each interval. The concentration of the vitamin in the withdrawn aliquots is determined by UV spectroscopy (λ_{max} = 220 nm) according to calibration curves calculated from standard solutions of B6 in BioSIF (figure A1-4 in Appendix 1).

4.6.3 In-Vitro Release Studies of Folic Acid

4.6.3.a In BioSGF

An amount of each of Fa-LDH, Fa-A/L16, Fa-A/L10 and Fa-A/L4 equivalent to 1.5 mg of folic acid was weighed and placed in a glass bottle. The samples were suspended in 250 ml of BioSGF, to ensure the solubility of folic acid is reached. The stoppered glass bottles were placed in a water-bath shaker set at 37 °C and a shaking speed of 50 strokes/minute. 2-ml aliquots were withdrawn from each sample after: 10 minutes, 30 minutes, 1 hour and 2 hours. The withdrawn volume was replaced by 2 ml of fresh BioSGF at each interval. The concentration of the vitamin in the withdrawn aliquots is determined by UV spectroscopy (λ_{max} = 300 nm) according to calibration curves calculated from standard solutions of folic acid in BioSGF (figure A1-7 in Appendix 1).

4.6.3.b In BioSIF

After the 2-hour interval in BioSGF, the Fa-A/L composite beads were filtered, blotted and carefully transferred, along with a new sample of Fa-LDH, to another set of clean, labeled glass bottles containing 30 ml of BioSIF (sink conditions) and returned to the water-bath shaker under the same conditions. 2-ml aliquots were withdrawn from each sample after: 30 minutes, 1, 2, 4, 6, 20 and 24 hours in BioSIF. The withdrawn volume was replaced by 2 ml of fresh BioSIF at each interval. The concentration of the vitamin in the withdrawn aliquots is determined by UV spectroscopy (λ_{max} = 280 nm) according to calibration curves calculated from standard solutions of folic acid in BioSIF (figure A1-8 in Appendix 1).

4.7 Measuring the Swelling Percentage

Since the swelling of alginate in acidic media should be minimal, the swelling of the composite beads was evaluated in the basic media of the BioSIF under the same conditions as the *in-vitro* release studies: in a water bath shaker set at 37 °C and shaking speed of 50 strokes per minute. The degree of bead swelling on exposure to BioSIF was investigated by subjecting equal weights of each of the vitamin-loaded composite beads to the media and measuring their weight after a set time.

0.025 g of each of the B6-loaded composite beads (B6-A/L16, B6-A/L10 and B6-A/L4) were placed in 30 ml of BioSIF, for 8 hours. Every 2 hours, the beads were filtered and blotted with filter paper to remove excess fluid, and weighed.

The same procedure was applied for folic acid-loaded composite beads, except that the swelling experiment was done for only 6 hours, as the beads' integrity deteriorated by 8 hours. The swelling experiment was done in duplicates for each vitamin-loaded composite and the average calculated.

The swelling % was calculated as:

$$Swelling\ \% = \left(\frac{W_f - W_i}{W_i}\right) * 100 \qquad \textbf{(4-3)}$$

W_i is the initial weight of the beads (0.025 g) and W_f is their final weight after being subjected to BioSIF for a certain time.

4.8 Characterization Methods

This section presents the specifications of the instruments used for structural and chemical characterization of the prepared samples (XRD, FTI-R and N_2 sorption analysis), and for the vitamins' quantification in solution (UV spectroscopy).

4.8.1 XRD Analysis

The XRD analysis was done with a D8 Bruker X-ray diffractometer comprising Cu anode, producing high-intensity Kα X-rays of wavelength 0.1542 nm. The device was operated at 40 KV and 30 mA, and the scan spanned 2-theta range between 3° to 80° with a step size of 0.030°, and a step time of 3 seconds.

4.8.2 FT-IR Analysis

The FTIR analysis was done with a Thermo-scientific Nicolet 380 Fourier Transform Infrared spectrophotometer. The samples were first mixed with KBr powder at a 1:100 ratio, and compressed into KBr pellets by a hydraulic pump set at a pressure of 1400 KPa.

4.8.3 UV/Vis Spectroscopy

The absorbance of the vitamins in the different solutions was measured using a Varian Cary 500 UV-Vis NIR double-beam spectrophotometer. Solution concentrations were calculated using the Beer Lambert law (equation 3-2) after constructing calibration curves based on standard solutions of the vitamins (Appendix 1). Table 4-3 lists the λ_{max} values of B6 and folic acid in the loading determination solution, BioSGF, BioSIF and $CaCl_2$ solution.

Table 4-3. The absorption maxima values of vitamin B6 and folic acid in the loading determination solution (2.5 M HCl + phosphate buffer at pH 6.8), BioSGF, BioSIF and $CaCl_2$ solution.

Vitamin	**λ_{max} (nm)**			
	Loading determination solution	**BioSGF**	**BioSIF**	**$CaCl_2$ Solution**
B_6	290	290	220	307
Folic acid	300	300	280	256

4.8.4 Nitrogen Sorption Analysis

Nitrogen sorption analysis was done using an ASAP 2020-Micromeretics apparatus at 77 K. The time required to attain equilibrium for each point of the adsorption or desorption isotherm was between 15 and 20 minutes. The specific surface areas of the samples were calculated by the BET method and analyzed by the α_s method. The porosity of the samples was evaluated by the BJH method.

Chapter 5. **Results and Discussion**

5.1 Characterization of Pristine LDHs (pLDHs)

5.1.1 XRD Analysis

The X-ray diffractograms of both pristine LDHs (pLDH-0.1 and pLDH-0.2) are shown in figures 5-1 and 5-2, respectively.

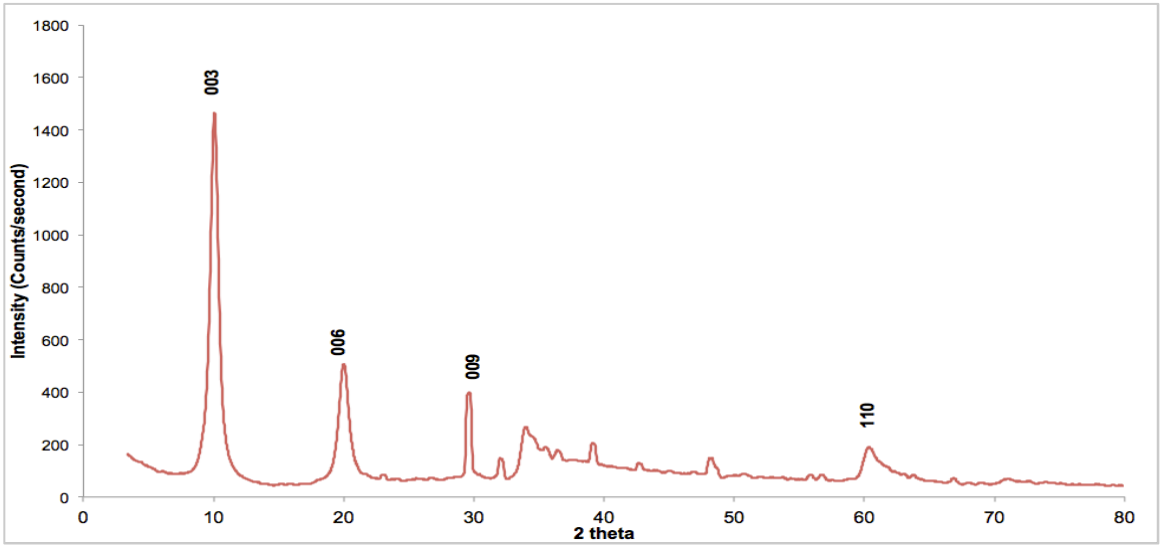

Figure 5-1. The XRD plot of the pristine LDH sample, pLDH-0.1.

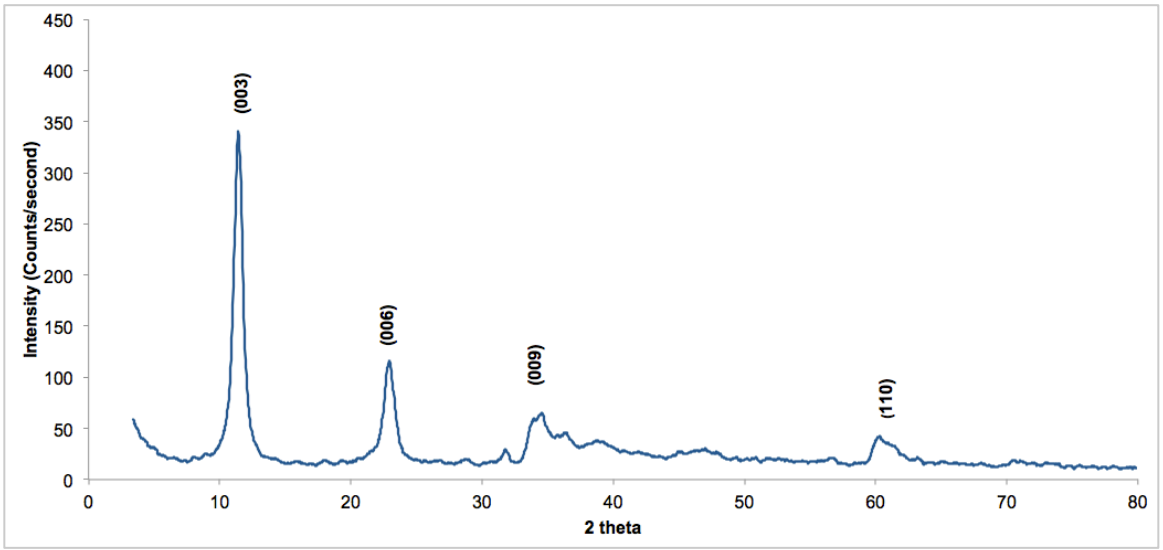

Figure 5-2. The XRD plot of the pristine LDH sample, pLDH-0.2.

Both XRD patterns exhibit features that are typical of well-crystallized Zn/Al hydrotalcite-like materials [25, 30, 95, 139]. Assuming a rhombohedral (3R) packing of the brucite-like layers, the first intense symmetric reflection is indexed (003) and it corresponds to the basal spacing between the layers $d_{(003)}$, which is defined as the sum of the inter-layer gallery height and the thickness of one brucite-like layer which is ~ 4.8 Å [140]. The first basal reflection

lies at 2θ = 9.90° for sample pLDH-0.1 and 11.25° for sample pLDH-0.2 corresponding to d_{003} values of 8.93 Å and 7.86 Å, respectively, as calculated by Bragg's law (equation 3-1). The less intense symmetric peaks at higher 2θ values correspond to the higher order basal reflections indexed (006) and (009), which correspond to ½ $d_{(003)}$ and $^1/_3$ $d_{(003)}$ respectively, further confirming the crystallinity of the layered structure. The low-intensity asymmetric reflection near 2θ = 60° corresponds to the plane indexed (110), where $d_{(110)}$ directly correlates to the distance between the metal cations in the brucite-like sheets (lattice parameter a). Assuming a crystal structure based on a hexagonal unit cell with rhombohedral stacking of the brucite-like layers, the lattice parameter $c = 3d_{(003)}$ and $a = 2d_{(110)}$. Table 5-1 lists the basal spacing and lattice parameter values of both samples. The weak and broad reflections around 2θ = 34° in both samples may be attributed to the presence of zincite (ZnO), which may have formed as an impurity in the LDH structure due to the basic pH of coprecipitation, as reported by Kloprogge et al [141-143].

The size of nitrate ions is ~ 3.7 Å, which complies with the interlayer spacings calculated: 4.13 Å for pLDH-0.1 and 3.06 Å for pLDH-0.2, suggesting their intercalation, along with evidence from FTIR, which will be presented in the next section [144].

Table 5-1. Basal spacing and lattice parameter values of pLDH-0.1 and pLDH-0.2.

Sample	$d_{(003)}$ (Å)	Inter-layer spacing (Å)*	c (Å)	a (Å)
pLDH-0.1	8.93	4.13	26.79	2.93
pLDH-0.2	7.86	3.06	23.58	3.07

** Calculated by subtracting 4.8 Å (the thickness of one brucite-like sheet) from $d_{(003)}$ [140]*

5.1.2 FTIR Analysis

The FTIR spectra of both pristine LDHs are shown in figures 5-3 and 5-4 respectively.

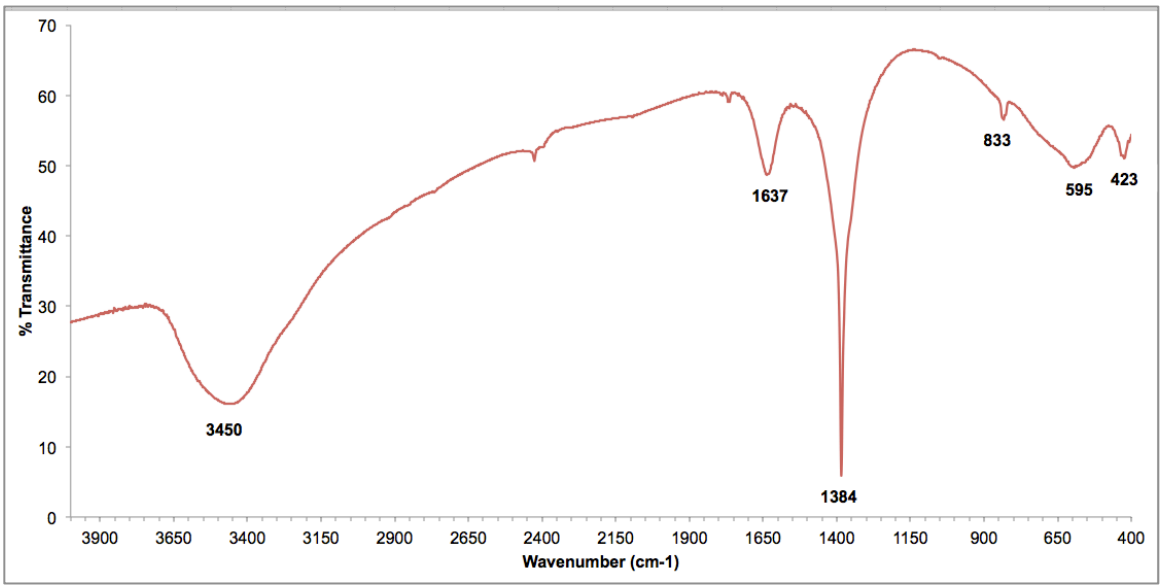

Figure 5-3. The FTIR spectrum of the pristine LDH sample, pLDH-0.1.

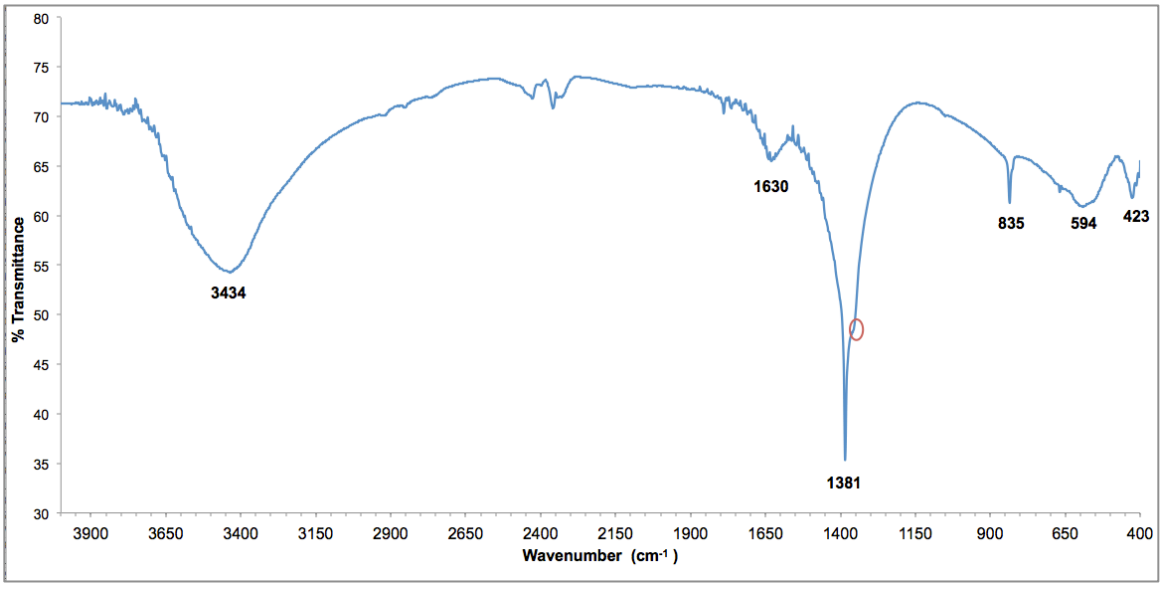

Figure 5-4. The FTIR spectrum of the pristine LDH sample, pLDH-0.2.

The basic features of typical nitrate-intercalated Zn/Al-LDHs are obvious in both spectra and are in agreement with those reported in literature [144]. The broad and strong absorption band in the range of 3500 - 3400 cm^{-1} is attributed to the symmetric stretching vibrational modes of the O-H bonds, belonging to the hydroxyl groups of the brucite-like sheets and interlayer water molecules. Such band is redshifted, compared to that of free hydroxyl groups

that should appear at around 3650 cm^{-1}, confirming that the hydroxyl groups are involved in hydrogen bonding. The absorption peak in the range of 1640 - 1630 cm^{-1} belongs to the H-O-H bending vibrational modes of water molecules. The peak at ~ 1380 cm^{-1} is assigned to the asymmetric stretching vibrations the bonds in nitrate, confirming its presence in the LDH structure. In the FTIR spectrum of pLDH-0.2, the nitrate peak is associated with a shoulder (the red-circled region in the figure 5-4) at a wavenumber of ~ 1360 cm^{-1}. This may be attributable to the asymmetric stretching vibrations of carbonate anions, which may have been co-intercalated during the coprecipitation process due to possible contamination by atmospheric carbon dioxide. Such finding may explain the relatively shorter interlayer spacing of pLDH-0.2 as compared to pLDH-0.1 (~3 Å and ~ 4 Å respectively). Since the carbonate anion has a higher charge density than nitrate, it attracts the brucite-like sheets more strongly and thus relatively shrinks the interlayer spacing. The absorption bands at low wavenumbers (< 900 cm^{-1}) are attributed to lattice vibrations. The peak at ~ 830 cm^{-1} is assigned to Al-O and Zn-Al-O bond stretching vibrations, while those at ~ 590 cm^{-1} and ~ 420 cm^{-1} are assigned to the bending vibrations of Al-O-H and Zn-Al-O [24, 139, 144, 146].

5.1.3 Nitrogen Gas Adsorption Analysis

The adsorption-desorption isotherm and the pore size distribution (PSD) plots of pLDH-0.1 are shown in figures 5-5 and 5-6.

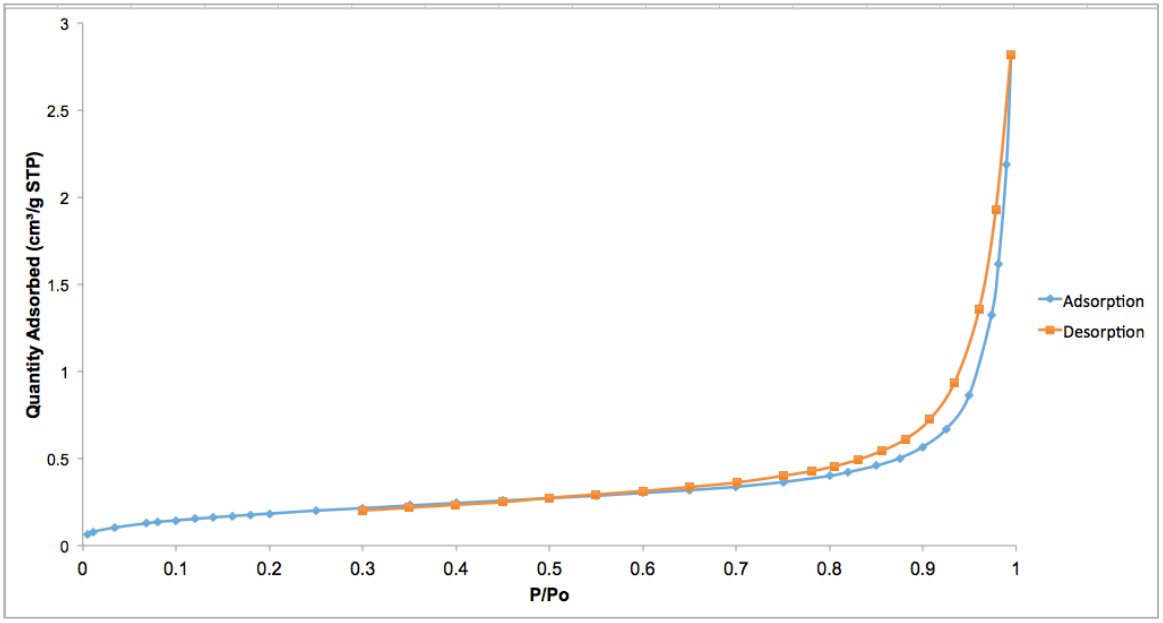

Figure 5-5. N_2 adsorption-desorption isotherm of the pristine LDH sample, pLDH-0.1.

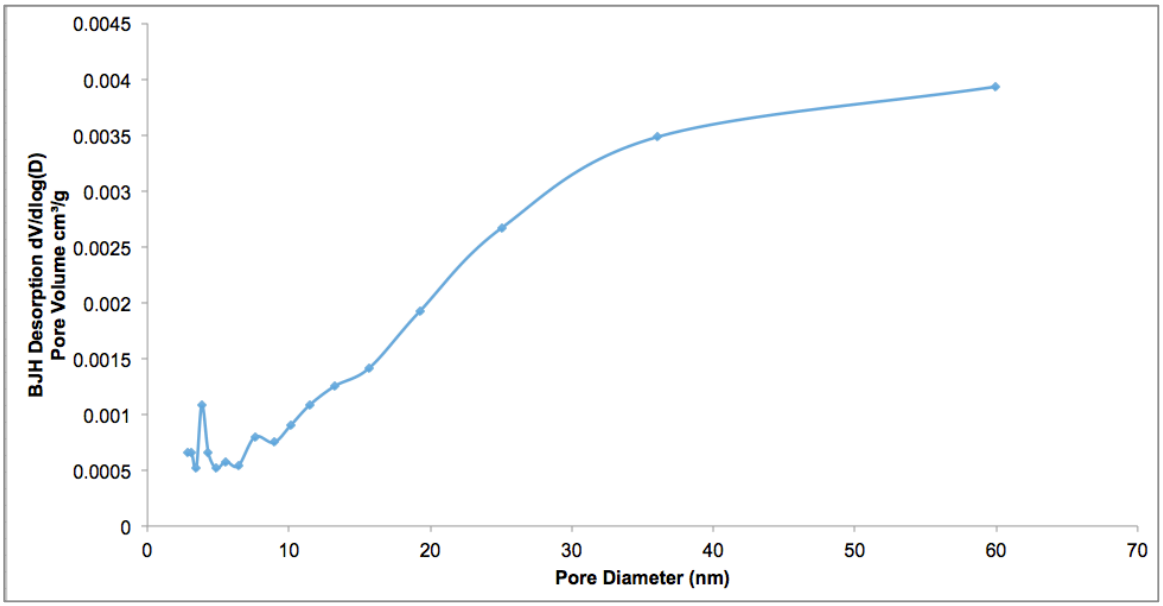

Figure 5-6. Pore size distribution (PSD) plot of the pristine LDH sample, pLDH-0.1.

The isotherm can be described as a pseudo-type (II)/type (IV) isotherm with type H3 hysteresis loop, which is typical of layered nanomaterials of mesoporous texture. The absence of limiting adsorption at high P/P_o value infers that the layered adsorbent is rather non-rigid with a low degree of pore curvature [129, 130]. The pore size distribution (PSD) plot exhibits a wide pore-diameter distribution: a small fraction of the pores have diameters in the range of 3-10 nm, whereas the rest have possibly collapsed into quite larger meso-pores and even macro-pores of diameters ranging from 10 nm up to 60 nm [147]. The BJH desorption average pore diameter is 18.19 nm and the BET surface area is 0.6778 m^2/g, which is much lower than values reported in literature. The extremely low BET surface area value maybe attributable to morphological characteristics of the LDHs such as increased particle size due to possible excessive inter-particle aggregation and/or the existence of inter-particle spaces that are too small to be accessed by N_2. However, such factors were not investigated in this research and may need to be explored further in future work [143, 146, 148, 149].

5.2 Characterization of B6-intercalated LDH (B6-LDH)

5.2.1 XRD Analysis

The X-ray diffractograms of pure vitamin B6, B6-LDH and pLDH-0.1 are shown in figure 5-7.

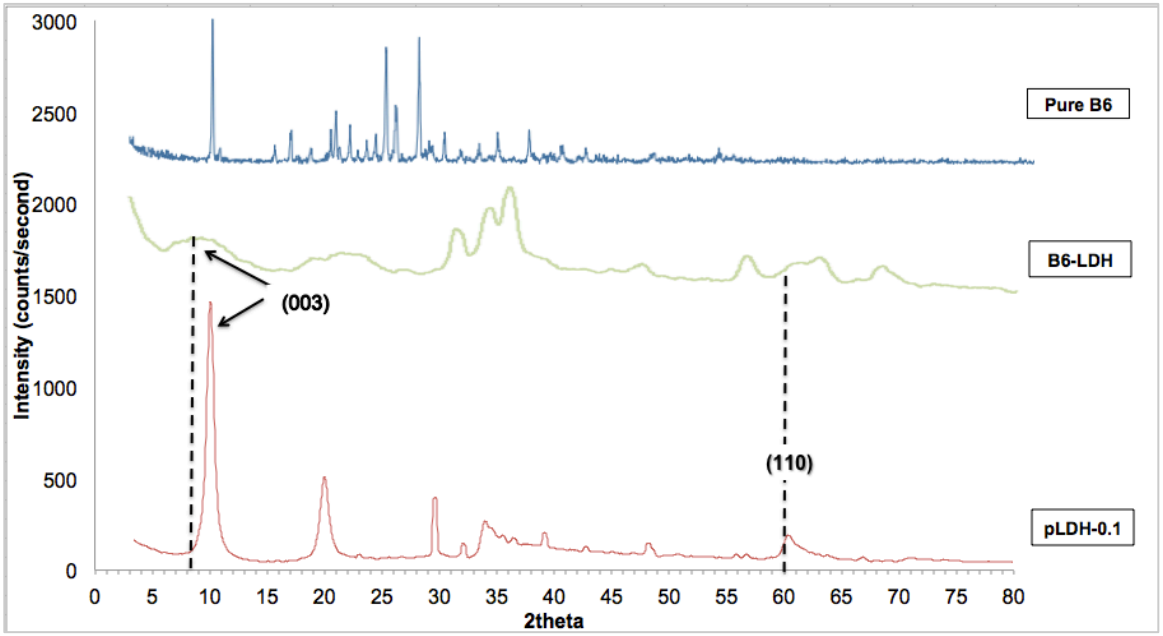

Figure 5-7. The X-ray diffractograms of pure B6, B6-LDH and pLDH-0.1.

In the B6-LDH plot, the (00*l*) basal reflections are shifted toward lower 2θ values. The (003) reflection is shifted to 2θ value of 8.49° corresponding to an increase of the basal spacing $d_{(003)}$ from 8.93 Å as in the control pLDH-0.1 to 10.4 Å. Subtracting the thickness of the brucite-like sheet (4.8 Å), the interlayer spacing is calculated to be 5.6 Å. The interlayer distance calculated is larger than the size of chloride, nitrate or carbonate anions, which may have been intercalated from the reaction solution during coprecipitation, thus the expansion of the interlayer space can be attributed to the successful intercalation of the vitamin B6 molecule. Foraida and Ramadan investigated the intercalation of B6 by coprecipitation in Zn/Al-LDH (Zn^{3+}/Al^{3+} =3), and modeled the molecular arrangement of the B6 molecule in between the brucite-like sheet using Gaussian 09 software package (semi-empirical pm3). The interlayer spacing was calculated to be 6.7 Å by XRD, and it was proposed that the B6 molecules were intercalated in monolayer arrangement with the phenolic and the 5-hydroxymethyl hydroxyl groups pointed toward the positive sheets, as shown in figure 5-8 [136]. In our situation, the interlayer distance is slightly shorter than the one reported by Foraida and Ramadan, which may suggest the intercalation of the B6 molecule in a more tilted orientation. The bump near 2θ = 60° belongs to the (110) plane reflection, and it confirms the preservation of the brucite-like sheets' structural integrity. Table 5-2 lists the

lattice cell parameter and interlayer space values of B6-LDH in comparison with those of pDH-0.1. It is worth mentioning that the intercalation process compromises the crystallinity of the LDH structure: the basal reflections have attenuated intensities. This is because the bigger the size of the intercalated anion, the higher is the degree of disturbance introduced to the regularly stacked layers, decreasing their periodicity/crystallinity [144]

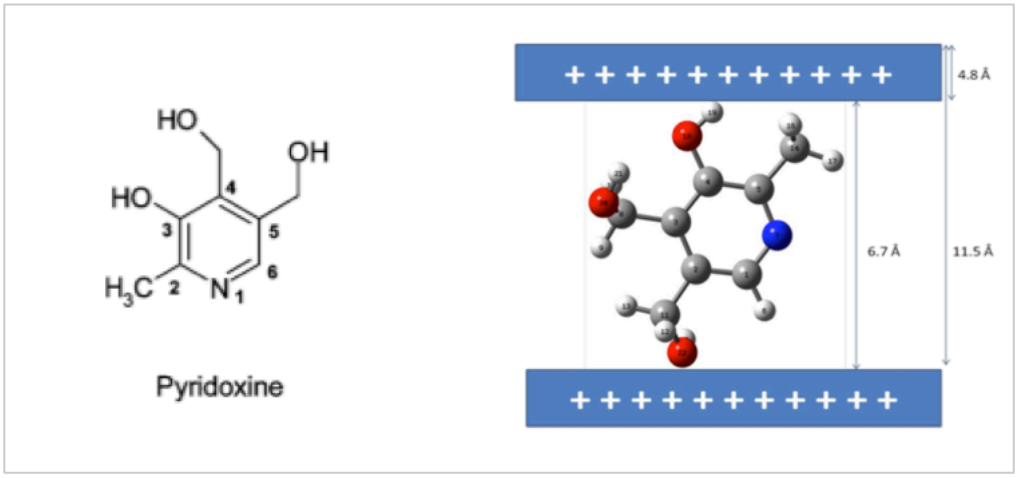

Figure 5-8. The molecular structure of vitamin B6 (left), and its modeled arrangement in between the brucite-like sheets as reported by Foraida and Ramadan (right) [136].

Table 5-2. Basal spacing and lattice parameter values of B6-LDH and its control pLDH-0.1.

Sample	$d_{(003)}$ (Å)	Inter-layer spacing (Å) *	*c* (Å)	*a* (Å)
pLDH-0.1	8.93	4.13	26.76	2.93
B6-LDH	10.41	5.61	31.21	3.05

** Calculated by subtracting 4.8 Å (the thickness of one brucite-like sheet) from $d_{(003)}$ [140]*

5.2.2 FTIR Analysis

The FTIR spectra of pure vitamin B6, B6-LDH and pLDH-0.1 are shown in figure 5-9.

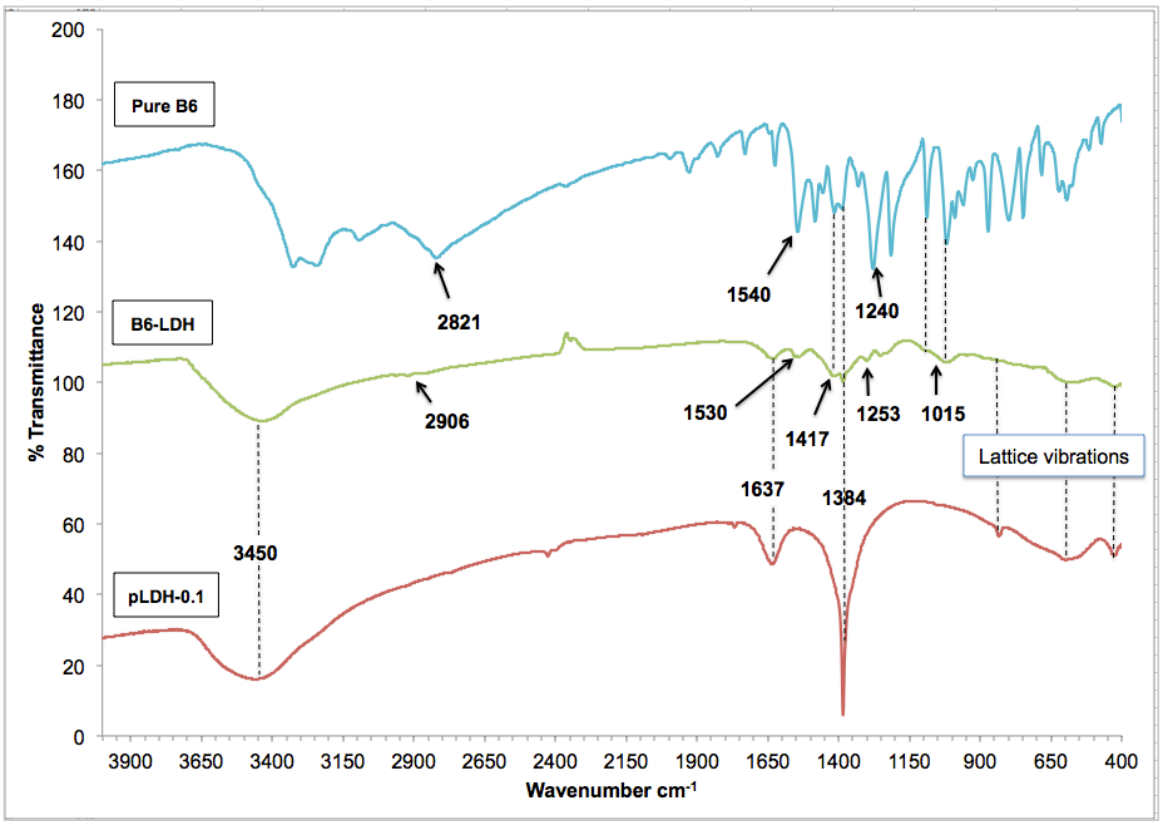

Figure 5-9. The FTIR spectra of pure vitamin B6, B6-LDH and pLDH-0.1.

Absorption peaks belonging to both LDHs and vitamin B6 can be seen in the B6-LDH FTIR spectrum confirming the presence of the vitamin in the LDH layers. As previously mentioned for the pristine LDHs, the stretching vibrations of the O-H bonds of the brucite-like sheet and the interlayer water molecules are observed at ~ 3450 cm^{-1}. The low-wavenumber peaks belonging to the LDH's lattice vibrations are preserved in the region from 900 - 400 cm^{-1}, confirming the structural integrity of the brucite-like sheets. The peak at ~ 2906 cm^{-1} is assigned to the stretching vibrations of the aliphatic C-H bonds of the methyl group. It is blueshifted from its position at 2821 cm^{-1} in the pure vitamin's spectrum. The peak at 1637 cm^{-1} is assigned to the bending vibrations (H-O-H) of interlayer water molecules, and is possibly broadened due to the overlap with the region where the peaks pertaining to the pyridine ring stretching vibrations arise. Such vibrations appear in the region from 1650 – 1200 cm^{-1} in the pure vitamin's spectrum. The peaks at 1530 cm^{-1} and 1253 cm^{-1} are assigned to the C-N-H bending and C-N stretching vibrations, respectively. The former is redshifted and the latter is blueshifted from their positions in the pure vitamin spectrum. The peaks appearing at 1417 and 1384 cm^{-1}, are assigned to C-O-H bending and C=C stretching

vibrations, respectively [106, 150, 151]. The peak at 1384 cm^{-1} can also be assigned to the stretching vibrations of the bonds in nitrate. However, its relatively low intensity suggests that even if nitrate is still present, most of it must have been replaced by B6 molecules. The sharp peaks at 1088 and 1018 cm^{-1} in the pure vitamin spectrum overlap and appear as a broadened less intense band at ~1015 cm^{-1}. These two peaks are assigned to the alcoholic O-H and C-OH stretching vibrations, respectively [106, 150, 151].

Peak shifts such as those observed in B6-LDH, when compared with the pure vitamin, are indicative of the existence of interactions between the B6 molecules and the brucite like-sheets. The pKa values of the B6 molecule are 5 and 9 for the nitrogen of the pyridine ring and the phenolic OH, respectively [50, 51]. Since the coprecipitation reaction was done at pH = 8, the B6 molecules are present mostly in neutral form, and thus they are expected to interact with the brucite-like sheets through only van der Waals' interactions and hydrogen bonding [152].

5.3 Characterization of Folic acid-intercalated LDH (Fa-LDH)

5.3.1 XRD Analysis

The X-ray diffractograms of pure folic acid, Fa-LDH and pLDH-0.2 are shown in figure 5-10.

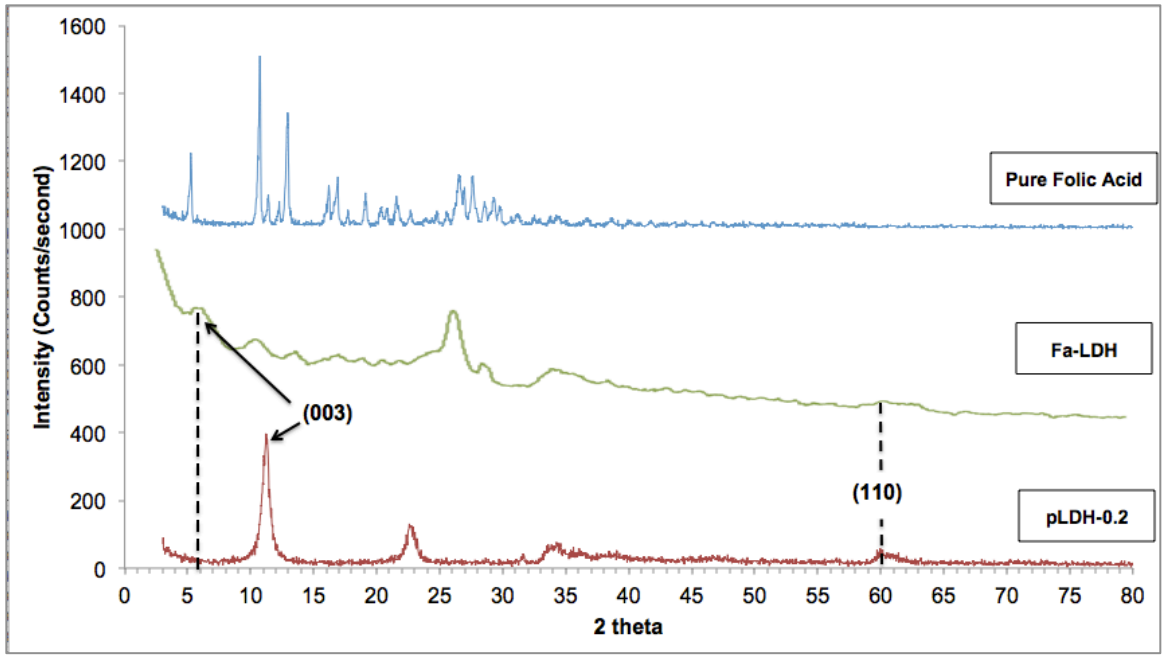

Figure 5-10. The X-ray diffractograms of pure folic acid, Fa-LDH and pLDH-0.2.

In the Fa-LDH plot, the (00*l*) basal reflections are shifted toward lower 2θ values. The (003) reflection is shifted to 2θ value of 6.72° corresponding to an increase of the basal spacing

$d_{(003)}$ from 7.86 Å as in the control pLDH-0.2 to 13.14 Å. Subtracting the thickness of the brucite-like sheet (4.8 Å), the interlayer spacing is calculated to be 8.34 Å. The magnitude of expansion of the interlayer gallery is comparable to values reported in literature and suggests the successful intercalation of folic acid in between the brucite-like sheets [77, 136, 153]
The expanded interlayer spacing is shorter than the longitudinal length of folic acid, which is approximately 21.5 Å, and is much longer than its lateral length. This observation suggests that folic acid is intercalated as a monolayer of longitudinally tilted molecules, as has been reported by Choy et al and Xiao et al [78, 153]. Figure 5-11 shows a schematic illustration of the mode of intercalation of folic acid reported by Xiao et al. for folic acid intercalated in Mg/Zn/Al-LDH, where the interlayer distance was 9.4 Å and the molecules were longitudinally arranged with a 60 ° tilting angle. The smaller interlayer distance calculated for the Fa-LDH described herein suggests that the molecules were arranged in a more tilted orientation [78].

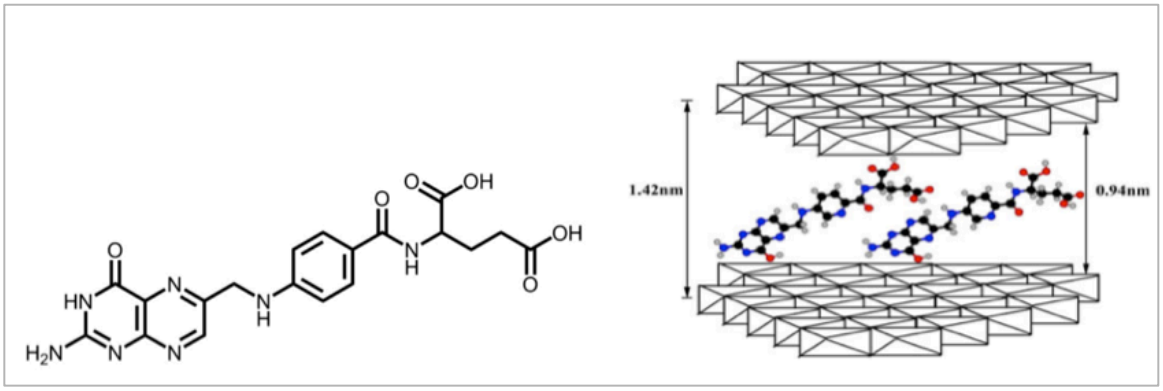

Figure 5-11. The molecular structure of folic acid (left) and a schematic illustration of its intercalation as longitudinally tilted monolayer of molecules in between the brucite-like sheets [78, 81].

In the Fa-LDH XRD plot, the weak reflections appearing between $2\theta = 10°$ and 30°, possibly belong to folic acid that may have re-crystallized as a separate phase during coprecipitation. The (110) reflection at $2\theta \sim 60$, though weak, it indicates the preservation of the brucite-like sheets. Table 5-3 lists the cell parameter and interlayer space values of Fa-LDH in comparison with those of pLDH-0.2. The XRD plot of Fa-LDHs exhibits a noticeable decrease in crystallinity when compared to the control pLDH-0.2, for the same reasons described for B6-LDH.

Table 5-3. Basal spacing and lattice parameter values of Fa-LDH and its control pLDH-0.2.

Sample	$d_{(003)}$ (Å)	Interlayer spacing (Å) *	*c* (Å)	*a* (Å)
pLDH-0.2	7.86	3.06	26.79	3.07
Fa-LDH	13.14	8.34	39.42	3.00

** Calculated by subtracting 4.8 Å (the thickness of one brucite-like sheet) from $d_{(003)}$ [140]*

5.3.2 FTIR Analysis

The FTIR spectra of pure folic acid, Fa-LDH and pLDH-0.2 are shown in figure 5-12.

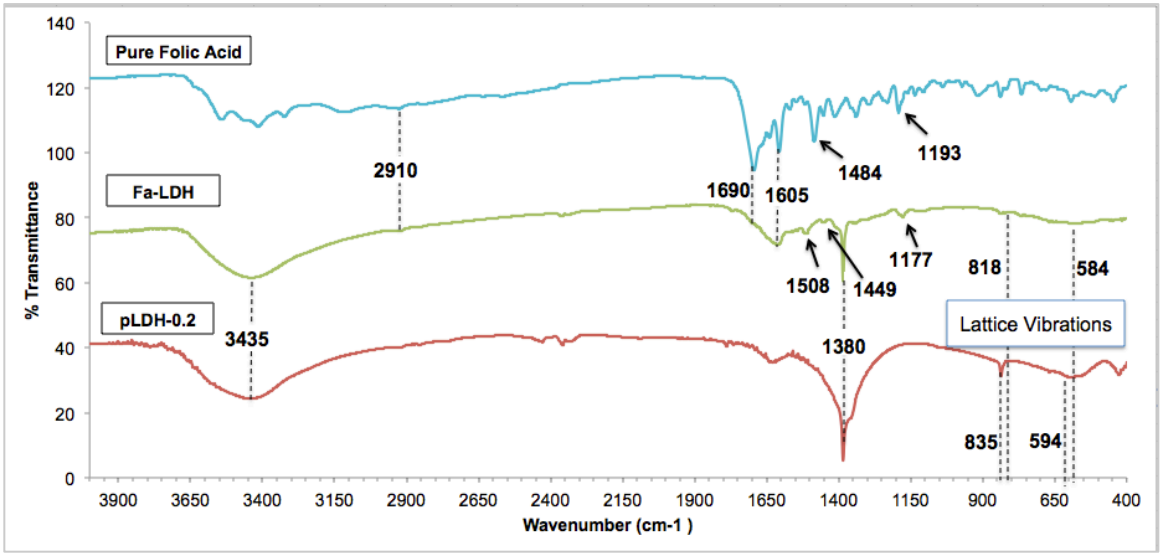

Figure 5-12. The FTIR spectra of pure folic acid, Fa-LDH and pLDH-0.2.

Absorption peaks belonging to both LDHs and folic acid can be seen in the Fa-LDH FTIR spectrum, confirming the presence of the vitamin in the LDH layers. The broad band at approximately 3435 cm^{-1} is assigned to the symmetric stretching vibrational modes of the O-H bonds belonging to the hydroxyl groups of the brucite-like sheets and the interlayer water molecules. The low-wavenumber peaks belonging to the LDH's lattice vibrations have slightly redshifted from 835 cm^{-1} and 594 cm^{-1} to 818 cm^{-1} and 584 cm^{-1} respectively, suggesting the possible presence of host-guest interactions between the brucite-like sheets and folic acid (either intercalated or adsorbed on the layers) [78]. The peak at ~ 2910 cm^{-1} is assigned to the stretching vibrations of the aliphatic C-H bonds. The region between 1690 and 1600 cm^{-1} comprises overlapping absorption peaks that can be assigned to the stretching vibrations of C=O bonds (~1690 cm^{-1}), the bending vibrations of the interlayer water molecules (~1630 cm^{-1}) and H-N-H of the aromatic amine group (~1610 cm^{-1}), in addition to the C=C bond stretching of the benzene ring (~ 1605 cm^{-1}). The peak at 1508 cm^{-1} is assigned to the anti-symmetric stretching vibrations of the carboxylate ions. The appearance

of the latter peak confirms the presence of the ionized form of folic acid (folate) in the LDH structure. The peak at 1449 cm^{-1} is assigned to the stretching vibrations of the bonds in the benzene ring. It is redshifted from its position at 1484 cm^{-1} in the pure folic acid spectrum. The sharp peak at 1381 cm^{-1} is assigned to the stretching vibrations of the bonds in nitrate, which suggests its co-intercalation in the LDH layers with folic acid. The peak at 1177 cm^{-1} is assigned to the stretching vibration of C-N bonds and is redshifted relative to its position at 1193 cm^{-1} in the pure folic acid spectrum [77, 78, 81, 153]. The peaks shifts observed with most of the chemical groups in intercalated folic acid, relative to the pure vitamin, in addition to those of the lattice vibrations indicate the presence of interactions between the folic acid molecules and the brucite-like sheets. The pKa values of folic acid are 3.1 and 4.8 for the carboxylic acid groups of the glutamate residue, and 10.5 for the aromatic amine [55-57]. Since the coprecipitation reaction was done at pH = 7, the folic acid molecules are present mostly in anionic form (the two carboxylic acid groups are ionized, giving the molecule a charge of -2), and thus they are expected to interact with the cationic brucite-like sheets mainly through electrostatic interactions, in addition to van der Waals' interactions and hydrogen bonding.

5.4 Characterization of the Alginate/LDH Composite Beads

5.4.1 XRD Analysis

Figure 5-13 shows the X-ray diffractograms of the vitamin-loaded LDHs (B6-LDH and Fa-LDH) before and after entrapment in the alginate matrix, in addition to that of plain calcium alginate beads (A0). The diffractograms of the composite beads with alginate:LDH ratio of 4:1 (B6-A/L4 and Fa-A/L4) were selected for such comparison, as representatives for the composite beads with the highest LDH content. The XRD analysis demonstrates the absence of peaks indicative of the presence of any crystalline phases of either the vitamins or the LDHs in the composite beads, when compared to the plots of the vitamin-intercalated LDHs (B6-LDH and Fa-LDH). This suggests that the LDH structure lost its regular layered arrangement and may have been de-laminated in the process of its entrapment in the alginate matrix.

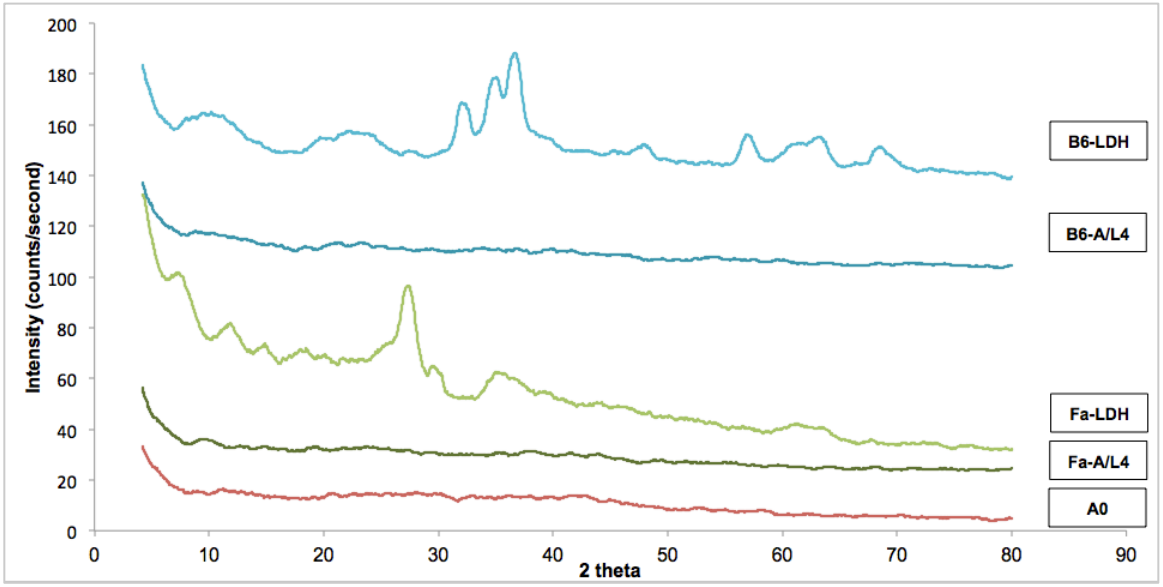

Figure 5-13. X-ray diffractograms of B6-LDH, B6-A/L4 composite beads, Fa-LDH, Fa-A/L4 composite beads and plain calcium alginate beads.

5.4.2 FTIR Analysis

In the FTIR spectra of the vitamin-loaded alginate/LDH composite beads, the overlapping of the multitude of peaks belonging to each component in the composite makes their analysis inconclusive when it comes to assigning the peaks to their chemical groups (Appendix 2). However, the FTIR spectra of the alginate/LDH composites without the vitamins are presented in order to characterize the chemical environment in the beads and identify any clay-polymer interactions present, aside from the loaded vitamin. The FTIR spectra of the pristine LDH (pLDH-0.1), composite beads of alginate:LDH ratios of 4:1 (A/L4) and 16:1 (AL/16), and plain calcium alginate beads (A0) are shown in figure 5-14.

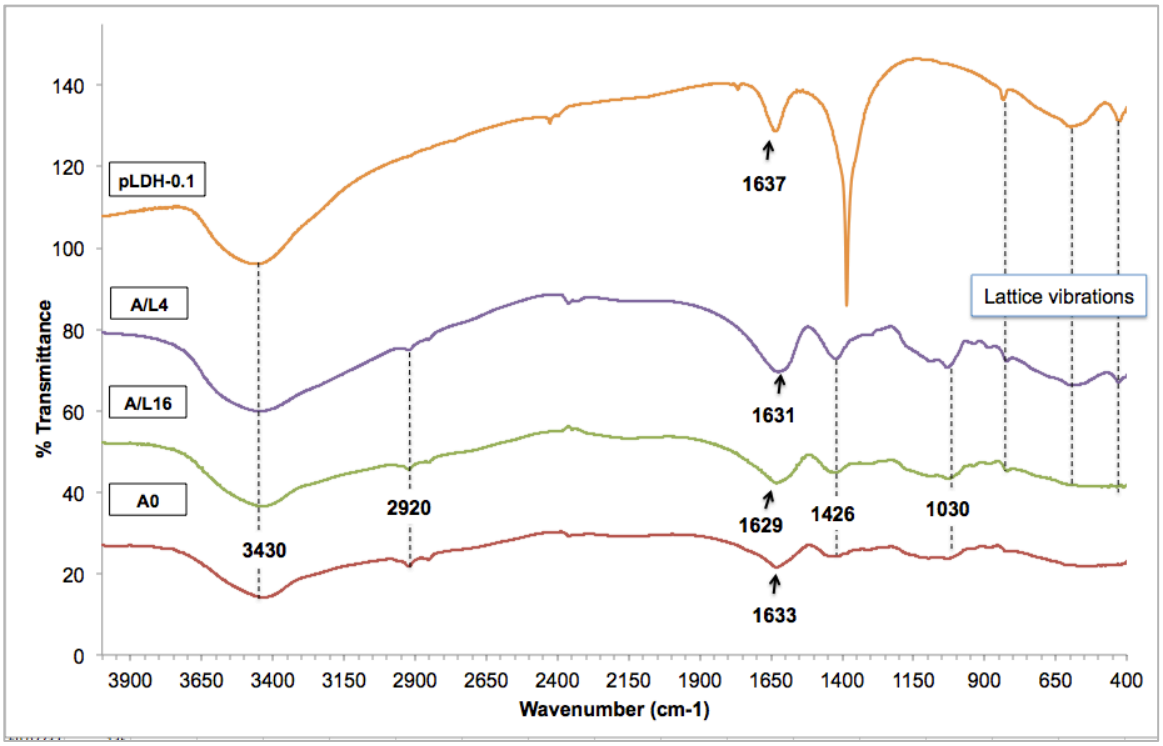

Figure 5-14. The FTIR spectra of pLDH-0.1, A/L4, A/L16 and A0.

In the A0 spectrum, the alginate polymer-specific peaks appear in the region from 1650 – 1030 cm^{-1}. The peaks appearing at ~1633 cm^{-1} and ~1426 cm^{-1} are assigned to the asymmetric and symmetric stretching vibrations of the carboxylate COO^- group bonds, respectively. The peak at ~ 1030 cm^{-1} is assigned to the stretching vibration of the cyclic ether C-O bonds in the pyranose ring. The peaks appearing at around 3430 cm^{-1}, and 2920 cm^{-1} are assigned to the alcoholic O-H and the aliphatic C-H bond stretching vibrations, respectively. In the A/L16 and A/L4 spectra, LDH structural features appear and become more intense as the LDH content increases (AL4>AL16). As shown in the spectra of A/L16 and A/L4, the peaks assigned to the lattice vibrations (900-400 cm^{-1}) are preserved, however, they have less 'defined' features than those in the pristine LDHs, which suggests the presence of possible interactions with the polymer. The peak in pLDH-0.1 at 1637 cm^{-1} that was assigned to the H-O-H bending vibrations of the interlayer water gets less intense and broader as the alginate content increases, possibly overlapping with the asymmetric stretching vibration of the alginate's COO^- group. Such overlap may have masked possible peak shifts of the COO^- group associated with the presence of interactions between the cationic LDH layers and the polymer as suggested. However, the peak at ~1426 cm^{-1} belonging to the symmetric stretching vibrations of the COO^- groups gets sharper as the LDH content increases. This may be attributable to a change in the coordination status of the carboxylates with the Ca^{2+} ions, which is another indication for the possible existence of clay-polymer interactions. The band at ~3430 cm^{-1} becomes rather more intense as the LDH

content increases due to the contribution of the brucite-like sheet and interlayer water molecules to the intensity of the O-H stretching vibrations of the whole composite [11, 154-156].

5.4.3 Nitrogen Gas Adsorption Analysis

The N_2 adsorption-desorption isotherm plots of the plain calcium alginate beads A0, and the control alginate:LDH composites of ratios 16:1 (A/L16), 10:1 (A/L10) and 4:1 (A/L4) are shown in figures 5-15 to 5-18 and their PSD plots are shown in figures 5-19 to 5-22.

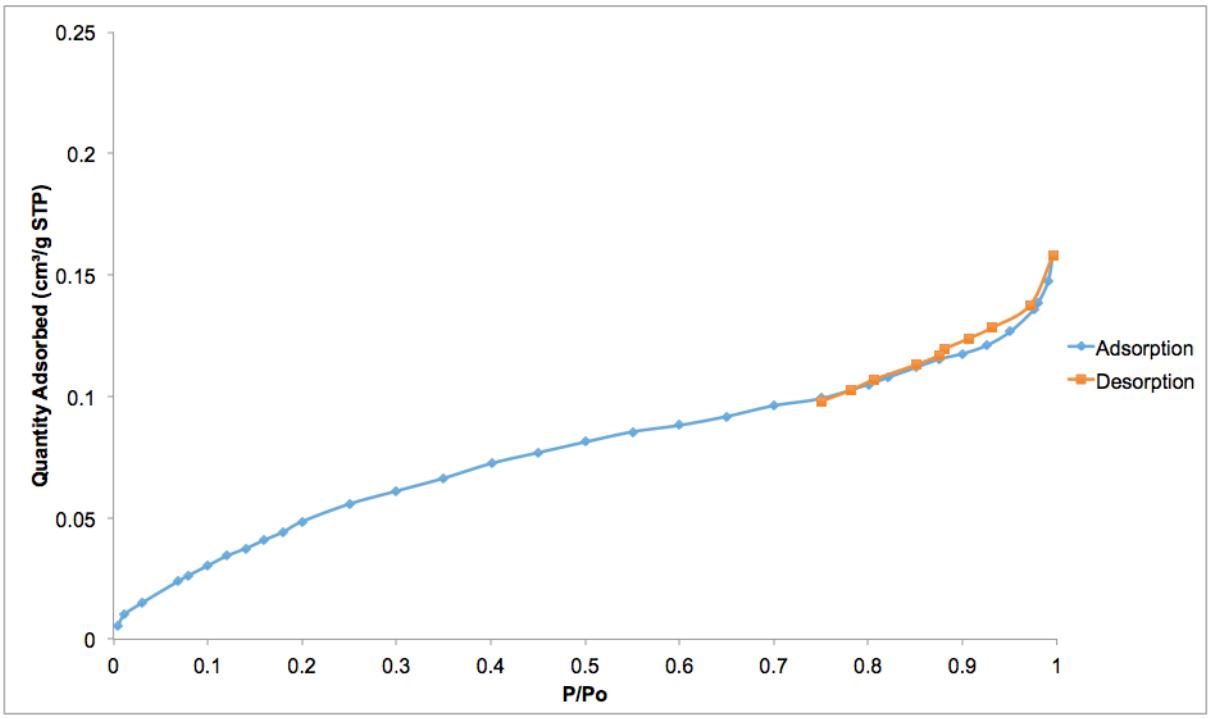

Figure 5-15. The N_2 adsorption-desorption isotherm of A0.

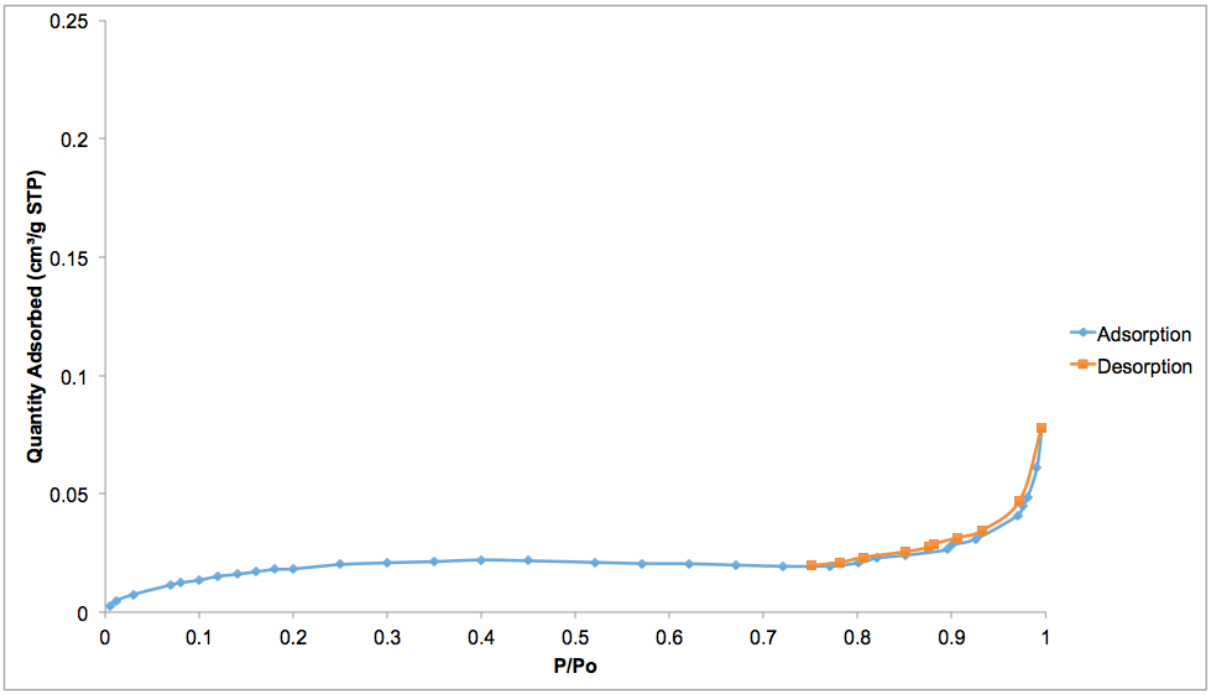

Figure 5-16. The N_2 adsorption-desorption isotherm A/L16.

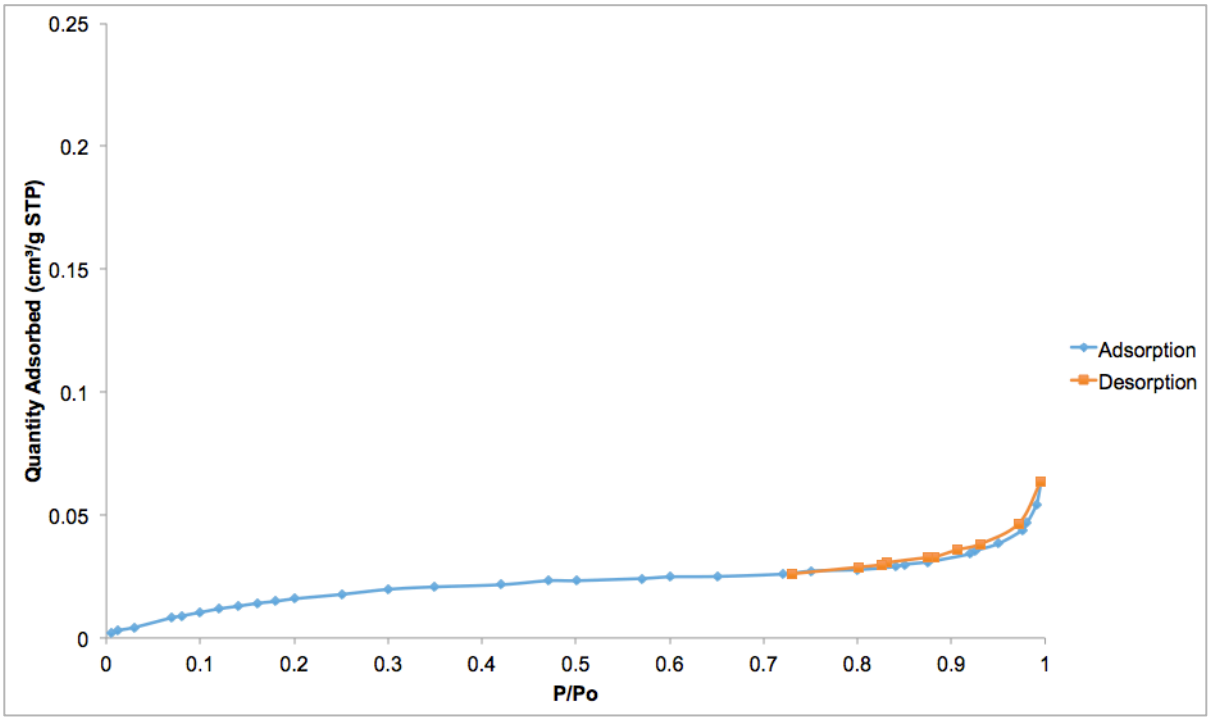

Figure 5-17. The N_2 adsorption-desorption isotherm A/L10.

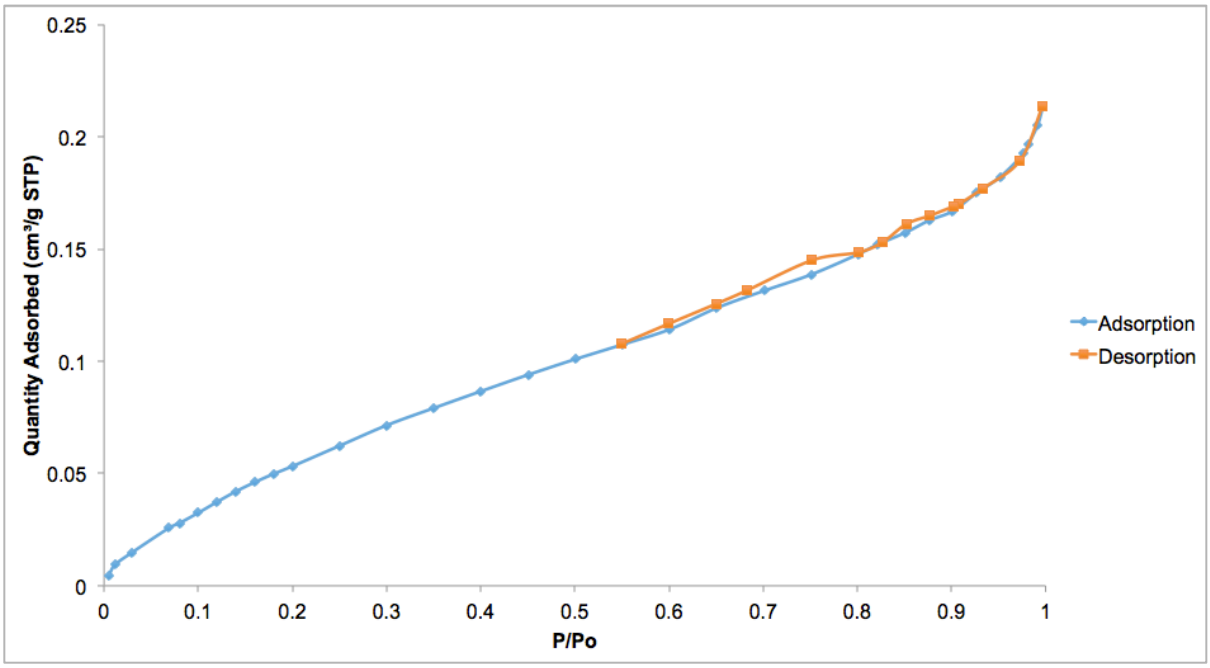

Figure 5-18. The N_2 adsorption-desorption isotherm A/L4.

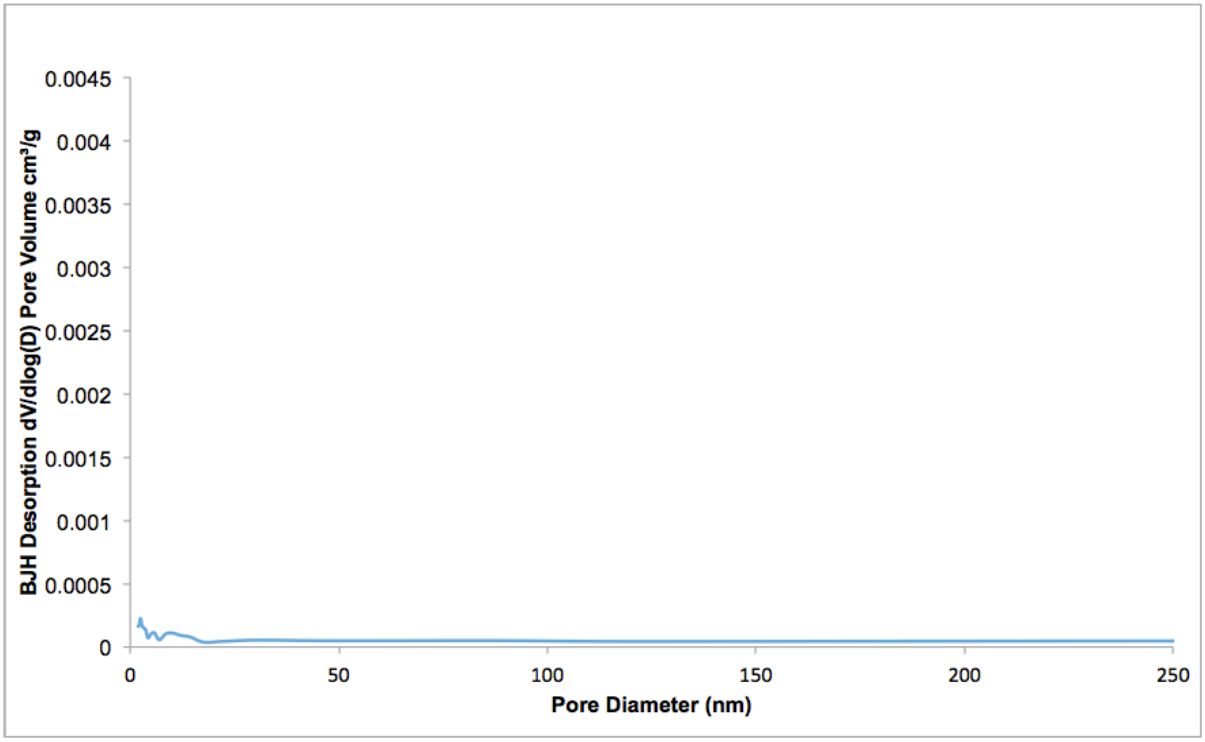

Figure 5-19. The pore size distribution (PSD) plot of A0.

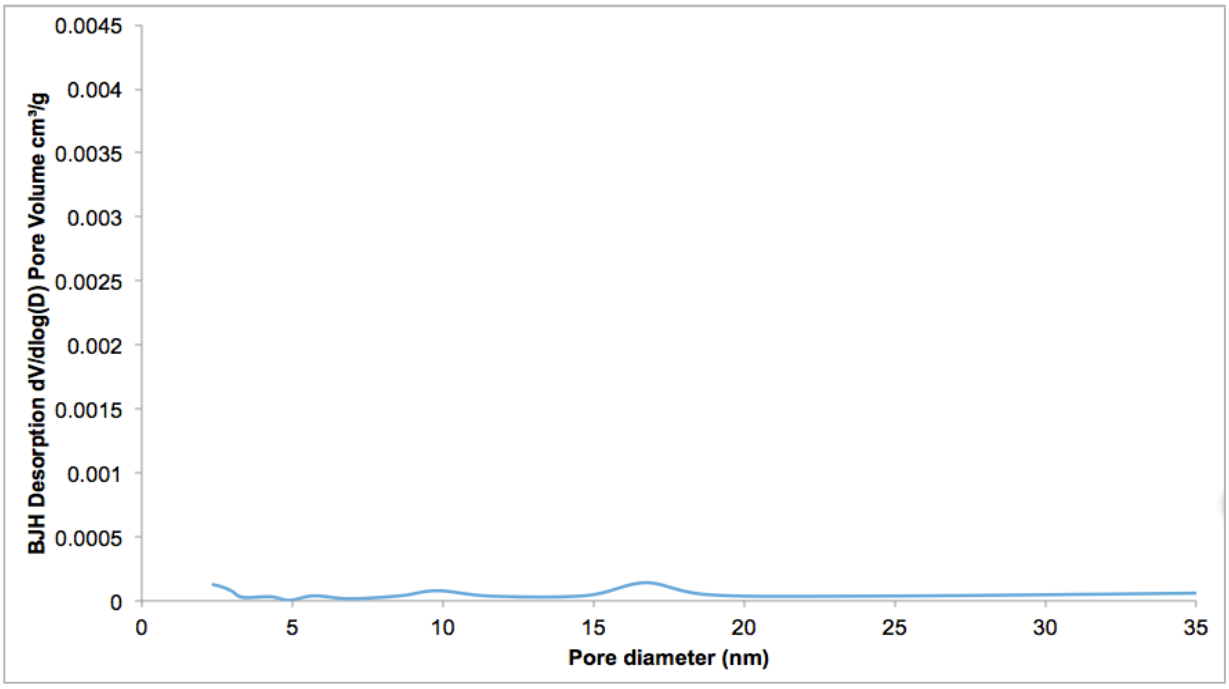

Figure 5-20. The pore size distribution (PSD) plot of A/L16.

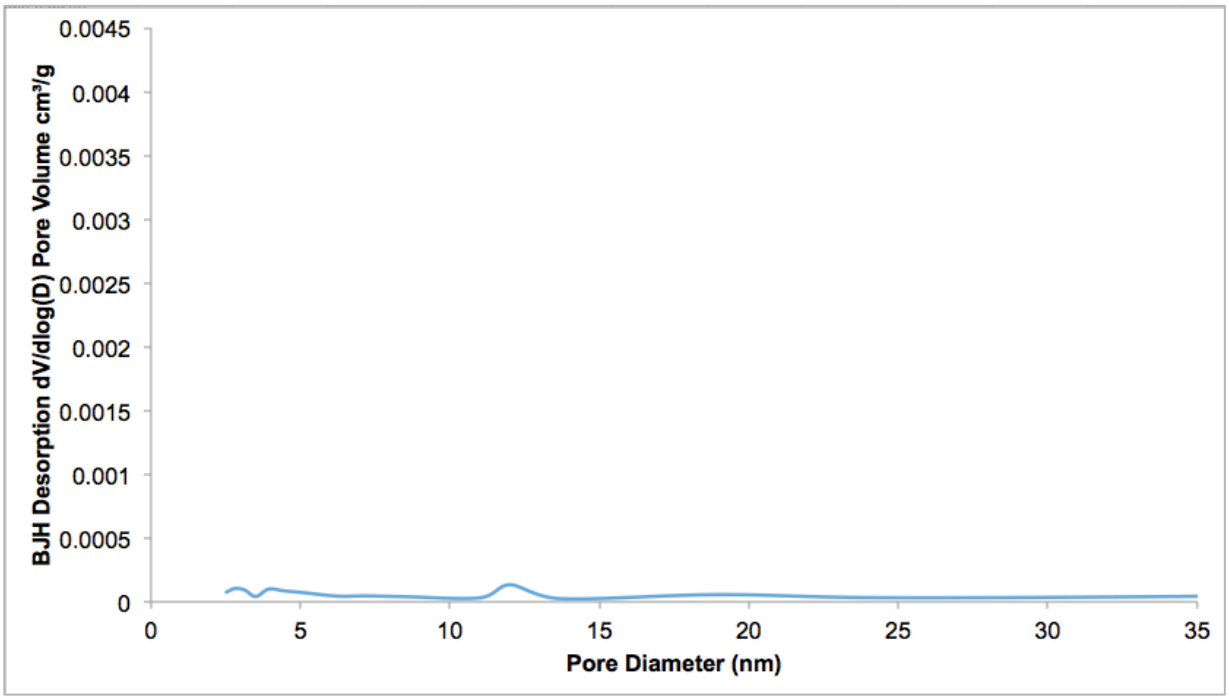

Figure 5-21. The pore size distribution (PSD) plot of A/L10.

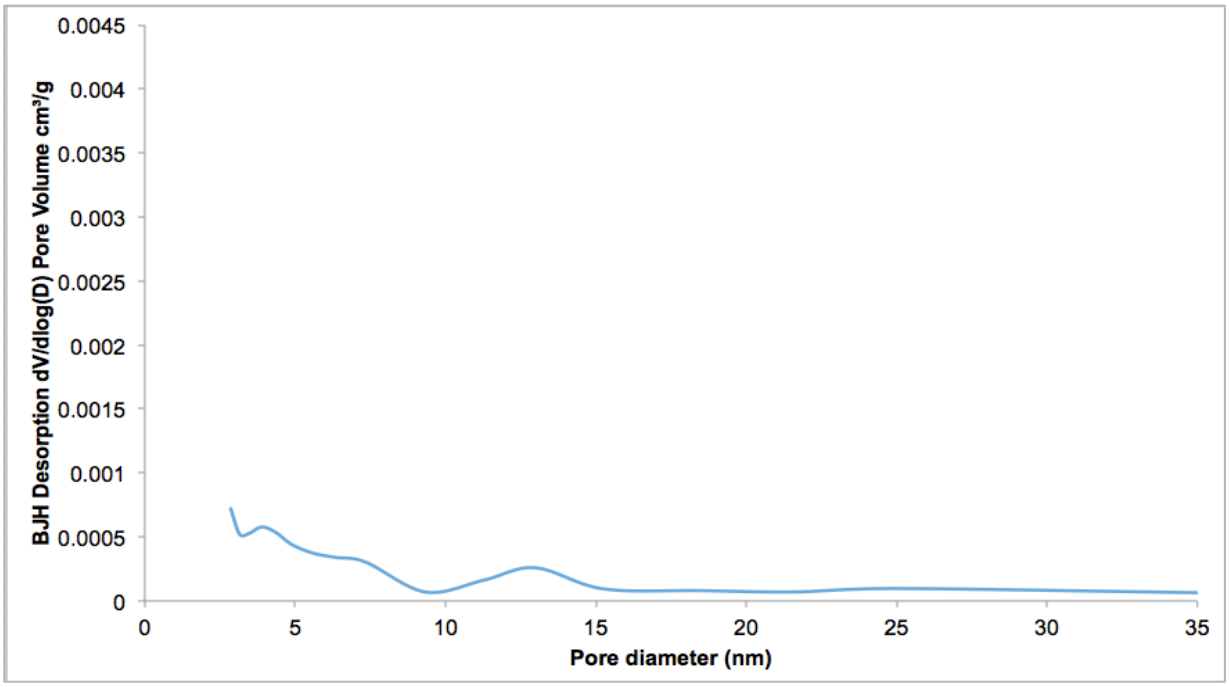

Figure 5-22. The pore size distribution (PSD) plot of A/L4.

The isotherms can be classified as pseudo-type (II)/type (IV) isotherms with type H3 hysteresis loops, indicating the presence of pores in the meso-size range as explained in section (5.1.3). It is observed in the isotherms of AL-16, AL-10 and AL-4 that the increase in the LDH content of the composite beads plays a role in the porosity texture of the composite. The three composites comprise pores in the meso-size range. The porosity of the plain calcium alginate beads and composite beads was too low for the pore size distribution to be reliably assessed, as is evident in the figures from 5-19 to 5-22. The BET surface area values and the BJH desorption average pore diameter values of A0, A/L16, A/L10 and A/L4 along with those of pLDH-0.1 are listed in table 5-4. The presence of LDH in the alginate matrix culminated in a decrease in the average pore diameter, which is in agreement with the results reported by Mandal et al [149]. A possible explanation to this observation is that the cationic layers of the LDHs may have played a role in the crosslinking of the anionic alginate chains during its gelation in the calcium chloride solution, and hence reducing the porosity as their content increases. The use of layered inorganic clays as polymer cross-linkers was reported in a number of investigations by Haraguchi et al. [157-160].

Table 5-4. The BET surface area and BJH desorption average pore diameter values of A0, A/L16, A/L10, A/L4 and pLDH-0.1.

Sample	BET surface area (m^2/g)	BJH desorption average pore diameter (nm)
A0	0.20	5.11
A/L16	0.07	7.03
A/L10	0.07	6.36
A/L4	0.24	5.30
pLDH	0.68	18.19

5.5 Loading Percentage and Entrapment Efficiency Determination

5.5.1 Loading Percentage of B6-LDH and Fa-LDH

The amount of vitamin loaded per weight of LDH by coprecipitation was measured and calculated as described in section (4.3), using equation 4-1. The loading percentage was calculated to be 31.5 % (w/w) for B6-LDH and 65 % (w/w) for Fa-LDH. The higher loading capacity of Fa-LDH compared to that of B6-LDH maybe attributed to a stronger interaction of the brucite-like sheets with the intercalated form of folic acid than with that of B6. Such observation can be explained by looking at the predominant molecular form of each vitamin at its coprecipitation pH as mentioned earlier. The pKa and the coprecipitation pH values of each of the vitamins are listed in table 5-5. According to these values, B6 is mainly intercalated in a neutral (zwitterionic) form, whereas folic acid is mainly intercalated as doubly charged folate anions. Therefore, B6 is expected to interact with the LDH layers through only hydrogen bonding and van der Waals forces, which are much weaker forces than the electrostatic interactions that would exist between folic acid (folate) and the cationic LDH layers leading to its higher loading percentage value. The co-intercalation of nitrate in Fa-LDH (as evidenced by XRD and FTIR) suggests that the relatively high loaded amount of folate is not exclusively in the interlayer space, but it is expected that a fraction is adsorbed on the LDH surface.

Table 5-5. A summary of the pKa values of B6 and folic acid and their corresponding molecular forms at their coprecipitation pH [50, 51, 55-57].

Vitamin	pKa_1	pKa_2	pKa_3	Coprecipitation pH	Predominant form (charge)
B6	5.0	9.0	15.0	~8	Neutral
Folic acid	3.1	4.8	10.5	~7	Anionic (-2)

5.5.2 Entrapment Efficiency (EE) of the Vitamin-Alginate/LDH Composite Beads

The entrapment efficiency (EE) of the prepared composites for each vitamin was measured and calculated as described in section (4.5) using equation 4-2. The results are summarized in table 5-6.

Table 5-6. EE% values of the vitamin-loaded alginate/LDH composite beads.

Sample	Amount loaded in LDH (g)	Amount leached in $CaCl_2$ (g)	EE %	Sample	Amount loaded in LDH (g)	Amount leached in $CaCl_2$ (g)	EE %
B6-A/L16	0.0246	0.0109	56%	**Fa-A/L16**	0.0508	0.0246	52%
B6-A/L10	0.0394	0.0171	57%	**Fa-A/L10**	0.0813	0.0301	64%
B6-A/L4	0.0984	0.0394	60%	**Fa-A/L4**	0.2030	0.0460	77%

It is evident from these results that increasing the LDH content in the composite beads minimizes the leaching of the vitamins into the gelling solution during the curing time and thus improves the entrapment efficiency of the vitamin in the beads. Similar findings were reported in literature on alginate composites with LDH and other clays [21, 161]. The interactions between both vitamins and the brucite-like sheets, within which they are intercalated, make the LDHs in the alginate beads serve as reservoirs for the vitamins, minimizing their escape into the alginate matrix and their subsequent leaching into the gelling solution. The results here, are in agreement with such explanation, since the effect of increasing the LDH content in the composite beads comprising Fa-LDH was more pronounced on the improvement of entrapment efficiency than those comprising B6-LDH, due to folate's stronger interaction with the LDH layers, as mentioned earlier. The effect of LDH on improving the entrapment efficiency of the alginate beads can also be explained by the N_2 adsorption results presented in section (5.4.3), which show that the increase in the LDH content of the composite beads is associated with a decrease in the average porosity, and thus fewer paths are available for the vitamin leaching.

5.6 Swelling Studies of the Vitamin-Alginate/LDH Composite Beads

The swelling percentage values of the vitamin-loaded composite beads in BioSIF (pH 6.5), as calculated by equation 4-3, are presented in table 5-7.

Table 5-7. The swelling percentage values of B6- and folic acid-loaded composite beads in BioSIF. The experiment was done for 8 hours for B6 and 6 hours for folic acid.

	Swelling time	2 hours	4 hours	6 hours	8 hours
B6	B6-A/L16	1320 %	2600 %	2880 %	3160 %
	B6-A/L10	1382 %	2417 %	2500 %	2760 %
	B6-A/L4	1388 %	2264 %	2340 %	2640 %
Folic acid	Fa-A/L16	1544 %	2260 %	2460 %	-
	Fa-A/L10	1276 %	2560 %	2780 %	-
	Fa-A/L4	1090 %	1980 %	2240 %	-

Figures 5-23 and 5-24 show the swelling profiles of both vitamin-loaded composite beads with time.

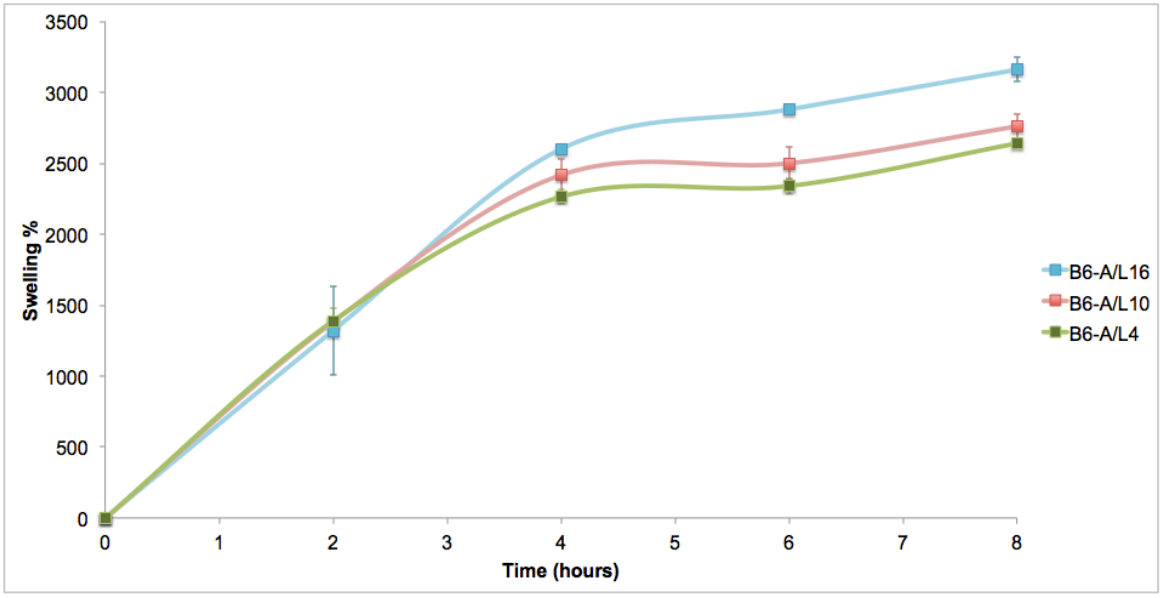

Figure 5-23. The swelling profiles of the B6-loaded composite beads in BioSIF (8 hours).

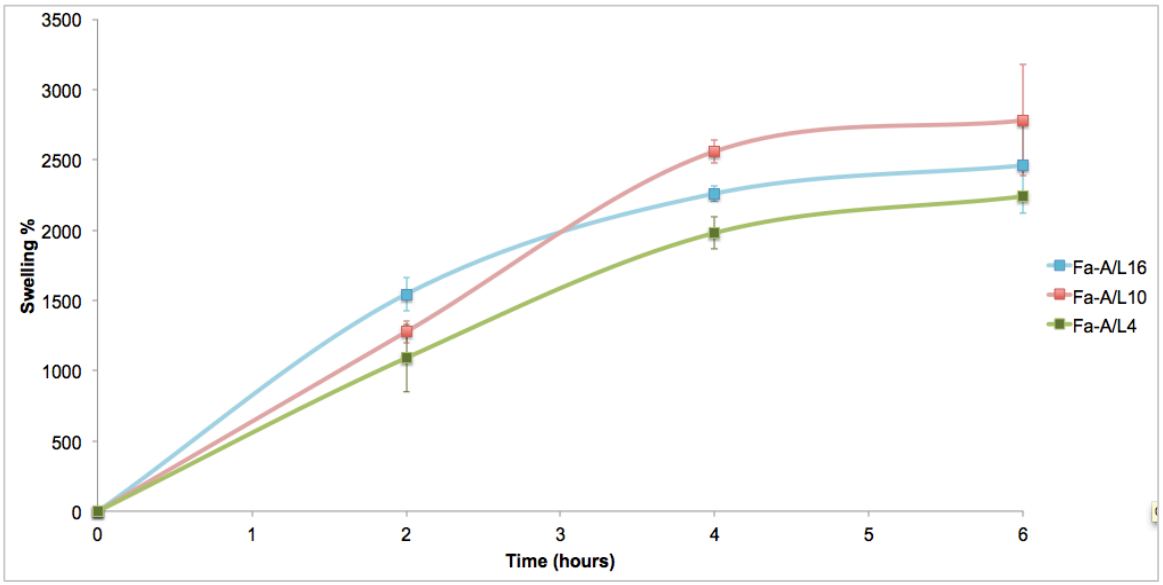

Figure 5-24. The swelling profiles of the folic acid-loaded composite beads in BioSIF (6 hours).

The results show that both vitamin-loaded composite beads undergo appreciable swelling in BioSIF for the first 4 hours. Past 4 hours, the degree of swelling per time is lower. The pKa value of the carboxylic acid groups of alginate ranges between 3.4 and 4.4 [45, 155]. In BioSIF (pH 6.5), the carboxylic acid groups of the alginate are ionized, resulting in the exposure of the negatively charged carboxylate groups (COO^-), which repel one another and result in the swelling of the alginate beads [38, 44-46]. The increase in the LDH content per bead was found to generally be accompanied with a decrease in the swelling degree of the vitamin-loaded composite beads. Such effect may have to do with a possible cross-linking reaction between the LDH and the alginate polymer chains, where the positive brucite-like sheets engage in electrostatic interactions with the negative COO^- groups of the alginate, screening their repulsive forces and restricting the flexibility of the polymeric chains. Such LDH-alginate interaction works against the swelling of the beads. This finding is in agreement with results reported by Hua et al. and Zhang et al. who demonstrated the decrease in the swelling of diclofenac-loaded LDH-calcium alginate beads as the LDH content increased, and attributed such effects to the LDHs serving as inorganic cross-linkers for the alginate polymeric chains [21, 22].

5.7 *In-Vitro* Release Studies of Vitamin B6

5.7.1 The Release Profiles of B6-LDH in BioSGF and BioSIF

Figures 5-25 and 5-26 show the release profiles of B6 from B6-LDH in BioSGF and in BioSIF, respectively.

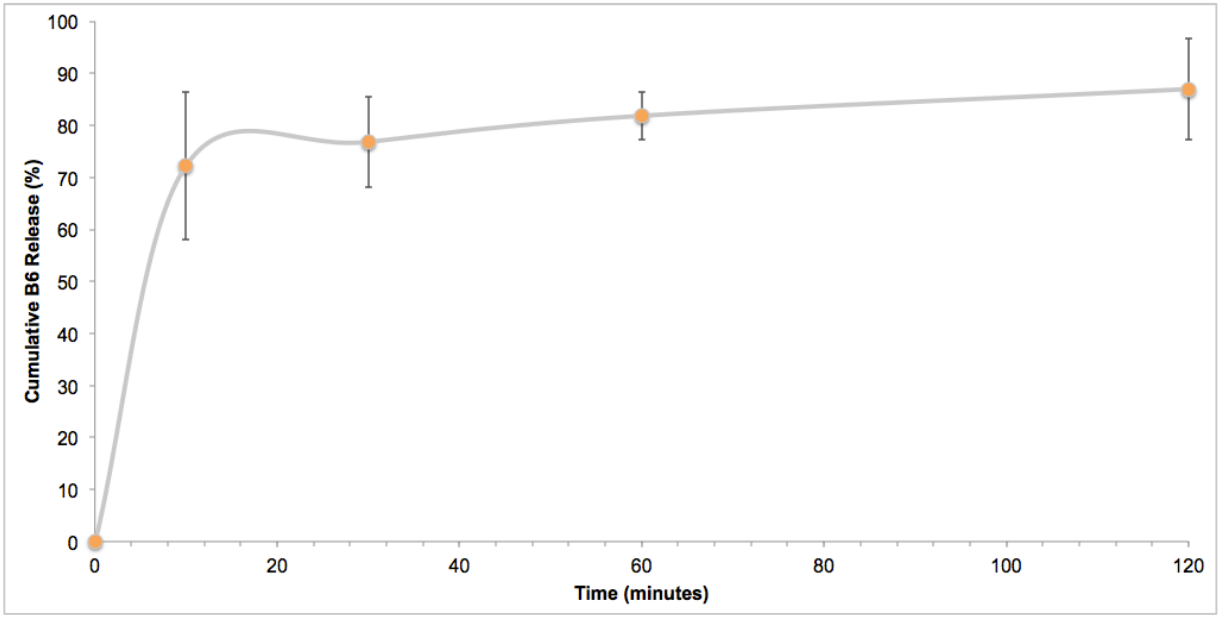

Figure 5-25. The release profile of B6-LDH in BioSGF (pH 1.6) for 2 hours.

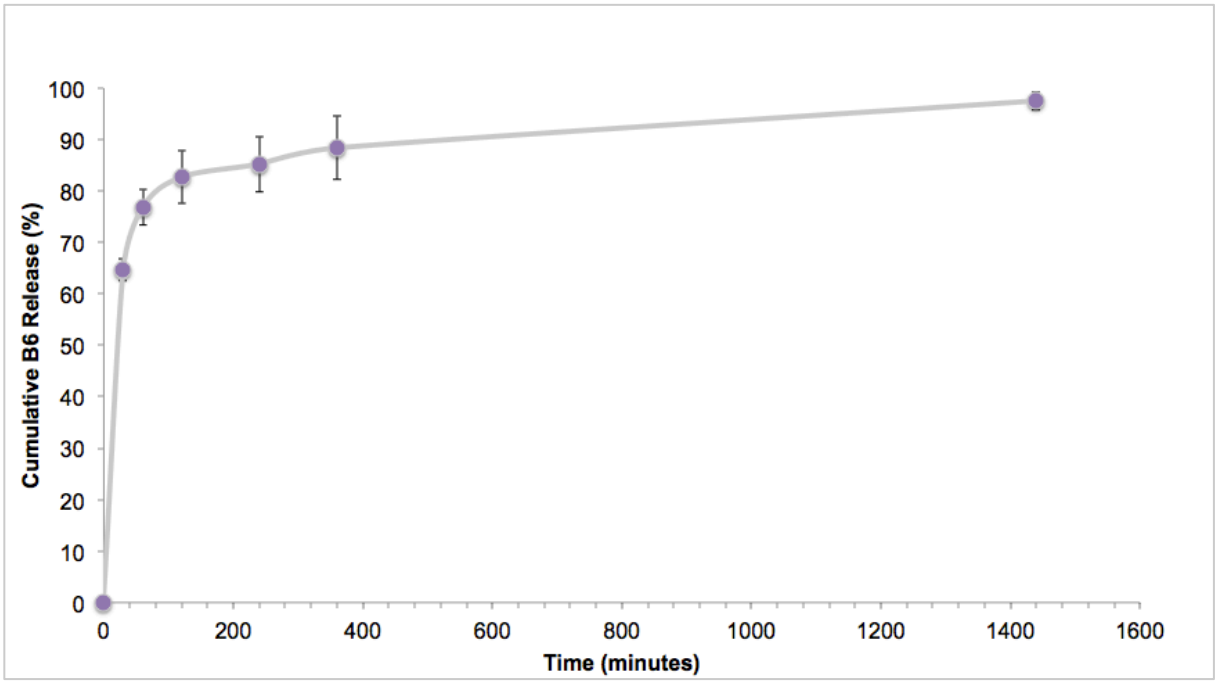

Figure 5-26. The release profile of B6-LDH in BioSIF (pH 6.5) for 24 hours.

In the acidic medium (pH 1.6), ~ 76% of the vitamin load was released in the first 30 minutes of the release study, followed by a reduction in the relative release with time, reaching up to ~ 86% in total by 2 hours. The release in the basic medium (pH 6.5) was relatively slower, where ~ 65% of the vitamin load was released in the first 30 minutes. The release of the rest of the vitamin's load was sustained, reaching ~ 98 % by the end of the experiment after 24 hours.

The main mechanism dominating the vitamin's release from B6-LDH in acidic conditions is the weathering of the basic LDH structure. At pH as low as 1.6, most of the surface hydroxyl groups of the brucite-like sheets are protonated on exposure to the acid, resulting in highly polarized and weakened M-O bonds and the subsequent dissolution of the LDH layers. Parello et al. proposed a two-step mechanism for the dissolution process of Mg/Al-LDH in highly acidic media, which can be extended to the Zn/Al-LDH system in our experiment [162]. The two-step dissolution mechanism can be represented as follows:

$$\mathbf{Zn/Al.LDH — OH + H^+ \rightleftharpoons ZnAl.LDH — OH_2^+} \quad \mathbf{(1)}$$

$$\mathbf{Zn/Al.LDH — OH_2^+ \rightarrow Zn^{2+} + Al^{3+} + intercalated\ species + H_2O} \quad \mathbf{(2)}$$

In addition to the weathering process, Cl^- ions present in the BioSGF, being of smaller size and higher affinity to the brucite-like sheets than vitamin B6, are also expected to contribute to the vitamin's de-intercalation and release from the LDH, by diffusing into the inorganic matrix and displacing B6 from the interlayer space [82, 163-165].
The release of vitamin B6 in basic conditions takes place strictly via anion-exchange with phosphate-type anions present in the BioSIF (HPO_4^{2-} and $H_2PO_4^-$). Phosphate anions have high affinity for the LDH layers and will thus diffuse into them and displace the intercalated B6. The progressively reduced relative release of the vitamin from the LDH may be attributed to the grafting reaction that happens between the highly acidic $H_2PO_4^-$ and the hydroxyl groups of the brucite-like sheets, producing Zn/Al hydroxyphosphate layers and rendering the phosphate ions no longer exchangeable. Such structure presents an obstacle to the diffusion of the rest of the intercalated vitamin, which has to resort to more tortuous and longer pathways to diffuse out of the LDH [166-168]. The release profile of B6-LDH in the basic medium exhibits improved sustained release properties when compared to that reported by Foraida and Ramadan [136]. This may be attributable to the higher pH of the coprecipitation reaction of B6-LDH than that applied in the coprecipitation reaction by Foraida and Ramadan, which increases the fraction of the negatively charged (deprotonated) B6 molecules that are expected to interact more strongly with the brucite-like sheets on intercalation.

5.7.2 The Release Profiles of B6-loaded Composite Beads

Figures 5-27 to 5-29 show the release profiles of B6 from samples (in order of increasing LDH content): B6-A/L16, B6-A/L10 and B6-A/L4, which were sequentially placed in BioSGF for 2 hours and then in BioSIF for 24 hours.

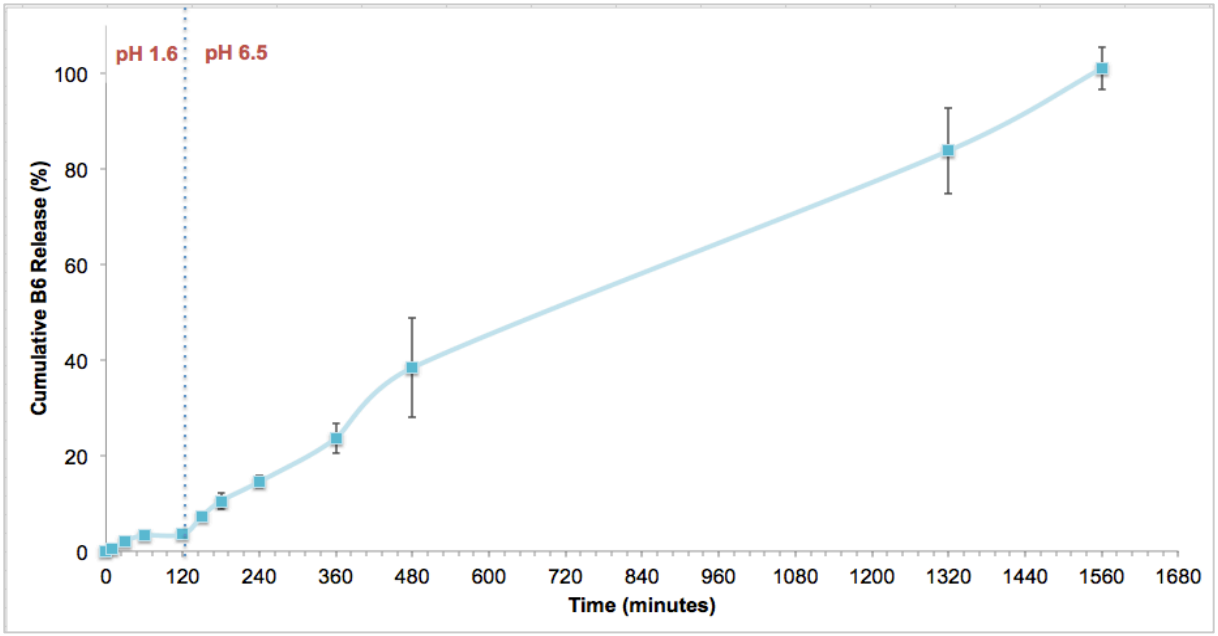

Figure 5-27. The release profile of B6-A/L16 composite beads (2 h in BioSGF, followed by 24 h in BioSIF).

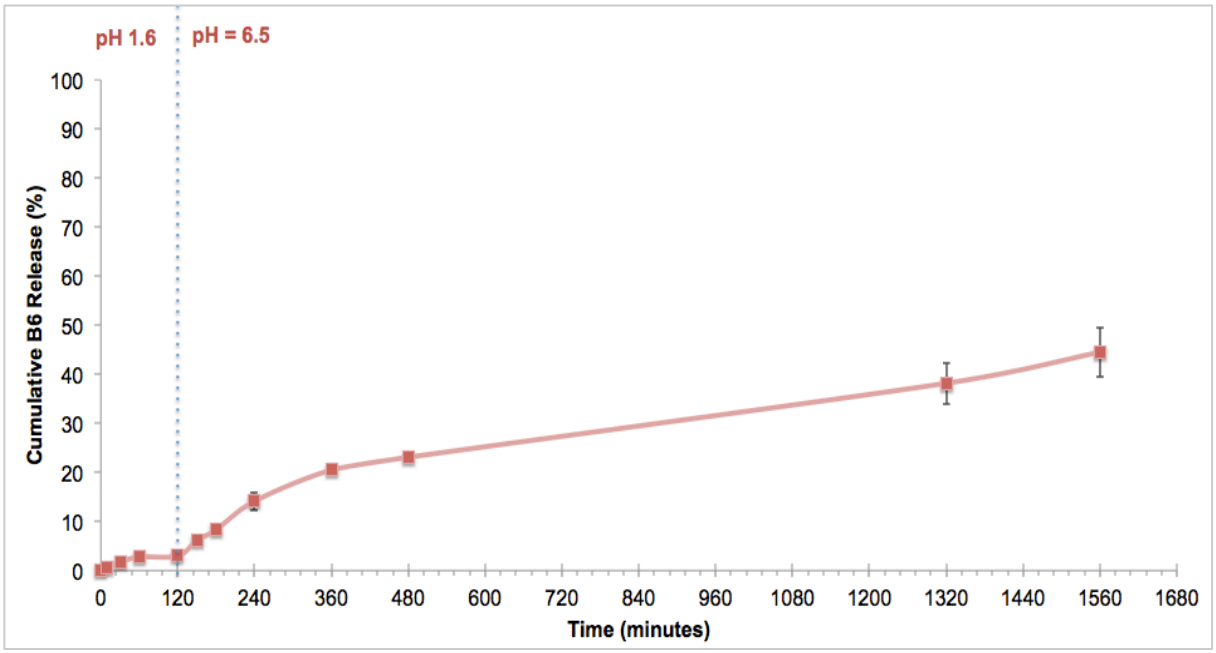

Figure 5-28. The release profile of B6-A/L10 composite beads (2 h in BioSGF, followed by 24 h in BioSIF).

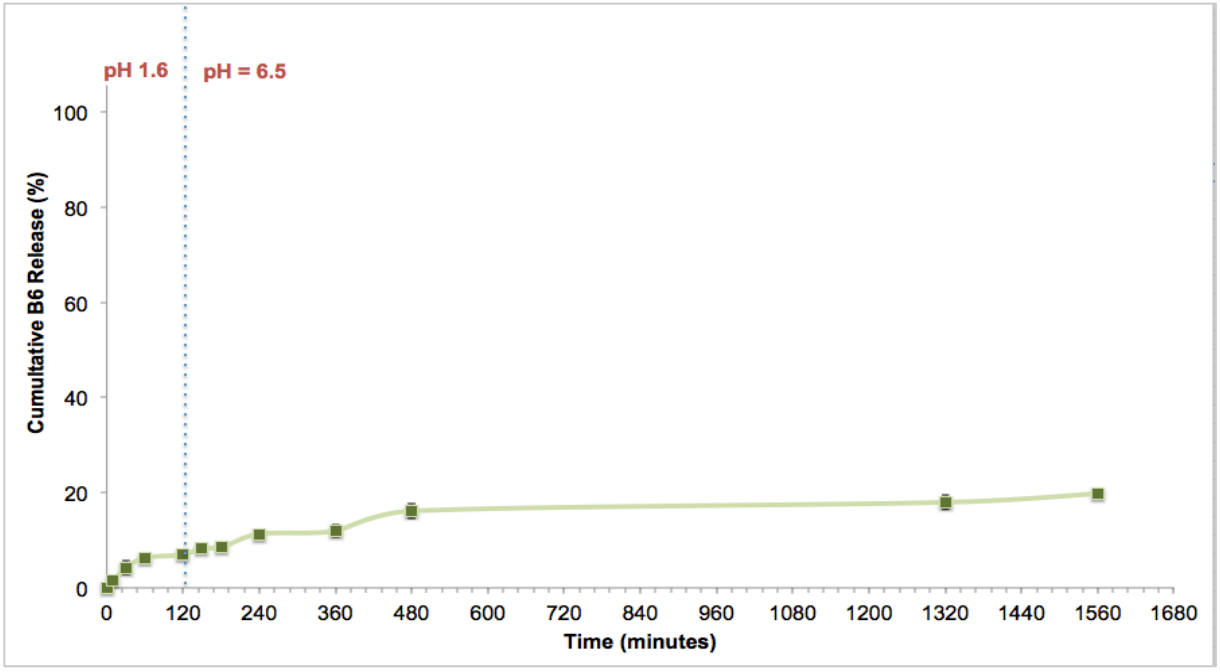

Figure 5-29. The release profile of B6-A/L4 composite beads (2 h in BioSGF, followed by 24 h in BioSIF).

It is evident from such release profiles that the entrapment of the B6-LDH in the alginate matrix is associated with a drastic improvement in the stability of LDHs in the acidic medium: only a maximum of 7% of the loaded vitamin was released in two hours (sample B6-A/L4) versus 86% from B6-LDH. The overall release profile from the B6-loaded composite beads exhibits a clear trend of reducing the relative release of the vitamin with time as the LDH content increases in the composite beads.

Figure 5-30 shows a 'magnified' view of the first 2 hours in the release profile of each of the composite beads when placed in BioSGF.

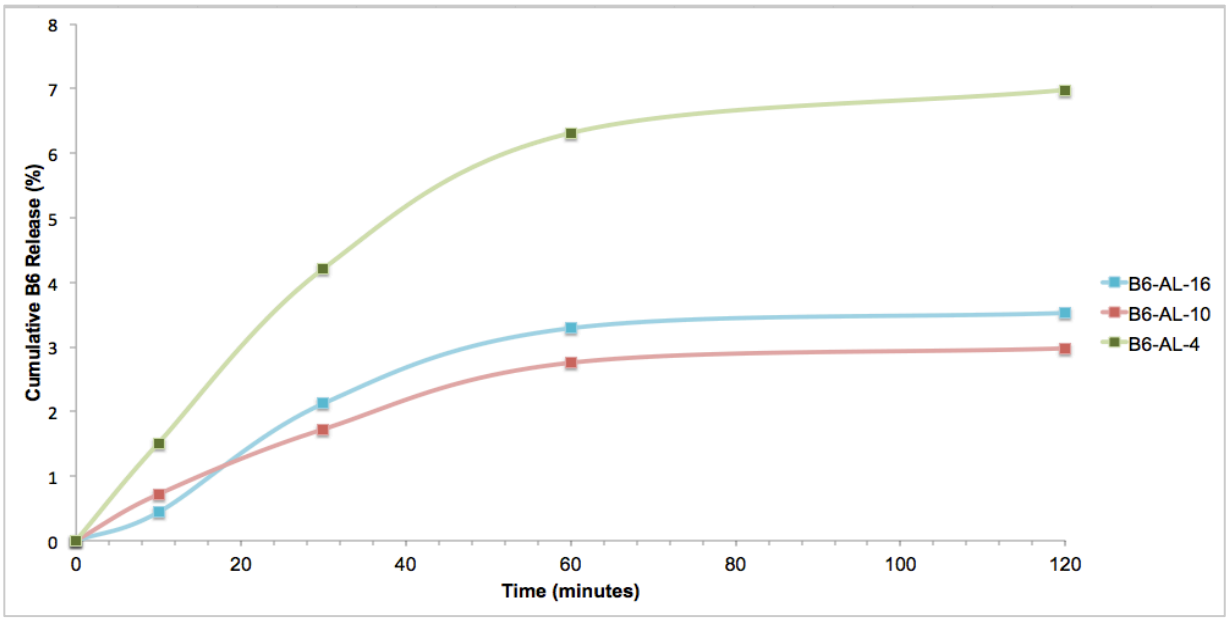

Figure 5-30. The release profiles of the B6-loaded composite beads in BioSGF (pH 1.6) for 2 hours.

It is interesting to notice that the trend of B6's release from the composite beads is almost opposite to that observed at the end of the experiment after 26 hours. B6-A/L16 and B6-A/L10 beads exhibit an almost coincident profile, releasing ~ 3.5% and ~ 3% of the B6 load in 2 hours, respectively. On the other hand, B6-A/L4 beads release approximately double the amount of B6 in the same duration of time (~7%).

Figure 5-31 shows the release profiles of the composite beads after they were filtered off the BioSGF and placed in the BioSIF for 24 hours.

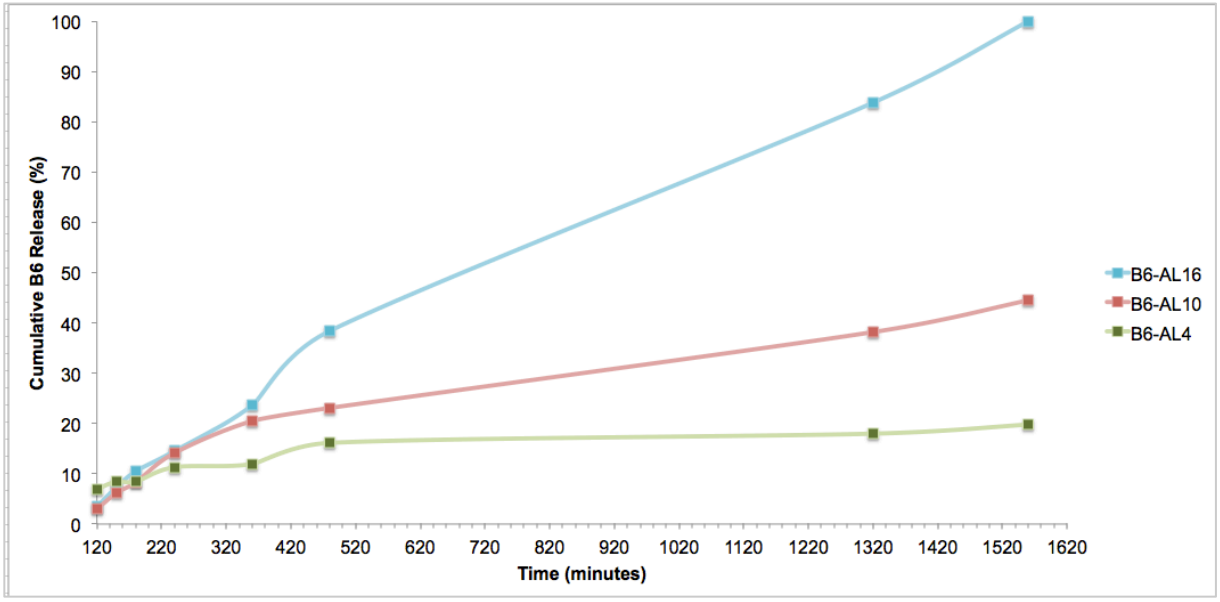

Figure 5-31. The release profiles of the B6-loaded composite beads in BioSIF (pH 6.5) for 24 hours.

Comparing the three profiles shows a clear trend of reduction in the relative release of B6 with time as the LDH content in the composite beads increases. After 2 hours in BioSIF, B6-A/L16 and B6-A/L10 released approximately five times the amount of B6 they had released after 2 hours in BioSGF (~3% → 14%), whereas the amount released from B6-A/L4 was less than doubled (7% → 11%) during the same period. The release from B6-A/L16 proceeds almost constantly, releasing its full B6 cargo by the end of the experiment (after 26 hours subjected to both media). The relative release from B6-A/L10 beads with time was much less than that from B6-AL/16, eventually releasing a maximum of ~ 44% of its B6 load by the end of the experiment. The relative release of B6 from B6-A/L4 with time was the least throughout the experiment. The release of the vitamin almost stopped after 6 hours in BioSIF, where only a maximum of ~ 20% of its B6 load was released by the end of the experiment.

In BioSGF, the beads undergo minimal swelling due to the protonation of alginate into the insoluble alginic acid. The reduced solubility and swelling of alginic acid in acidic media is the key factor in protecting the LDHs against breakdown in BioSGF, explaining the much reduced B6 release from the composite beads when compared to B6-LDH.

Since B6 is soluble in acidic media, and both its molecules and the alginate matrix are electrically neutral and are not expected to interact strongly with each other, the release behavior in BioSGF (pH 1.6) is expected to be governed mainly by the release of B6 from the entrapped LDH and its diffusion through the alginate matrix. The B6-A/L4 beads, containing more LDHs and less alginate per bead, are expected to have their LDHs more

prone/accessible to acid attack than those comprising a greater alginate content (B6-A/L16 and B6-A/L10). Even though alginate beads undergo minimal swelling in acidic media, it was apparently enough to allow protons from the BioSGF to attack the high density of LDHs in the B6-A/L4 beads: an action that eventually lead to the relatively higher vitamin B6 release % from B6-A/L4 beads than from the other composites in the same period of time.

As for the situation in BioSIF, it can be seen that the trend in the vitamin's release % with the LDH content per bead is as same as the swelling trend described in section 5.6. Therefore, the release behavior of B6 from the composite beads in the basic medium can be described in terms of their degree of swelling. The swelling decreases as the LDH content (which serve as polymer cross-linkers) increases, explaining the release % of B6 during the 24-hour experiment in BioSIF from the composite beads being in the order: B6-A/L16 > B6-A/L10 > B6-AL4. Such finding is in agreement with results reported by Hua et al. and Zhang et al. who demonstrated the decrease in swelling and release properties of diclofenac-loaded LDH-calcium alginate beads as the LDH content increased, and attributed such effects to the LDHs serving as inorganic cross-linkers for the alginate polymeric chains [21, 22]. In addition to the relatively reduced swelling, increasing the LDH content dispersed per bead endows the alginate matrix with barrier properties. This would render more difficult the diffusion of B6 through the swollen alginate matrix, necessitating B6 molecules to adopt more tortuous pathways in order to be released from the swollen beads. This would lead to a reduced release % from B6-A/L4 beads when compared to B6-A/L16 beads, which is in fact observed. Similar findings were observed for other clay-polymer composites, where the dispersion of the clay phase (exfoliated or intact) is associated with a decrease in the diffusivity of the species loaded in the clay [11].

5.8 *In-Vitro* Release Studies of Folic Acid

5.8.1 The Release Profiles of Fa-LDH in BioSGF and BioSIF

Figures 5-32 and 5-33 show the release profiles of folic acid from Fa-LDH in BioSGF and in BioSIF respectively.

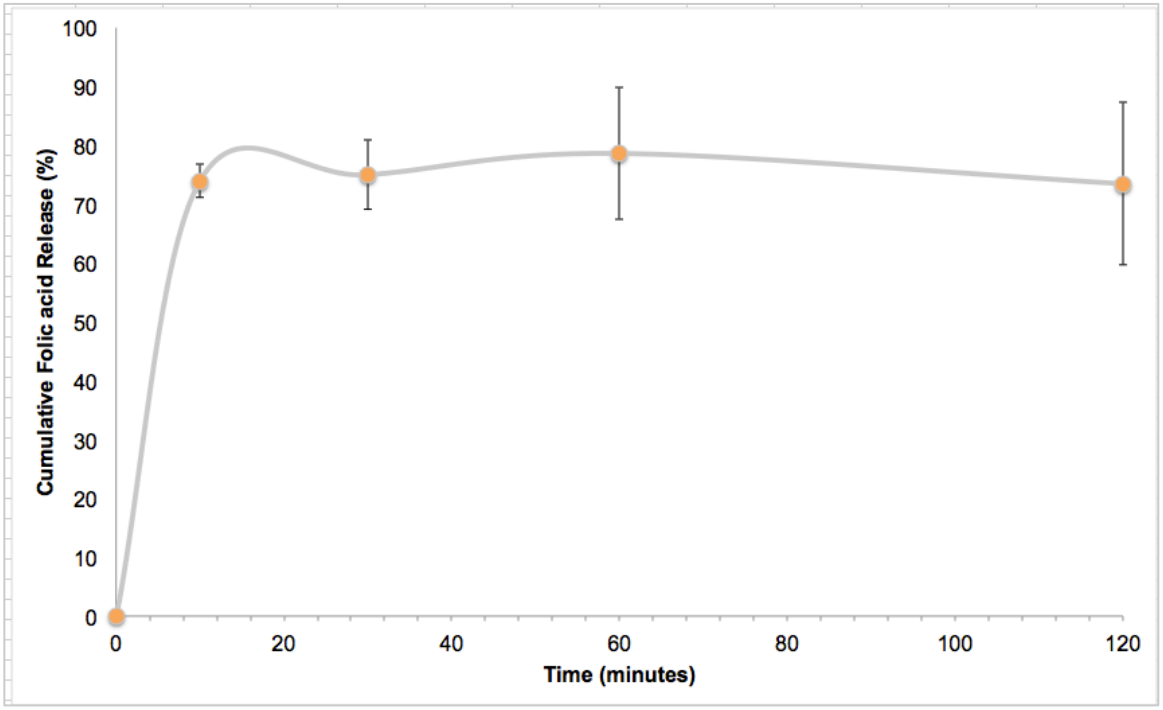

Figure 5-32. The release profile of Fa-LDH in BioSGF (pH 1.6) for 2 hours.

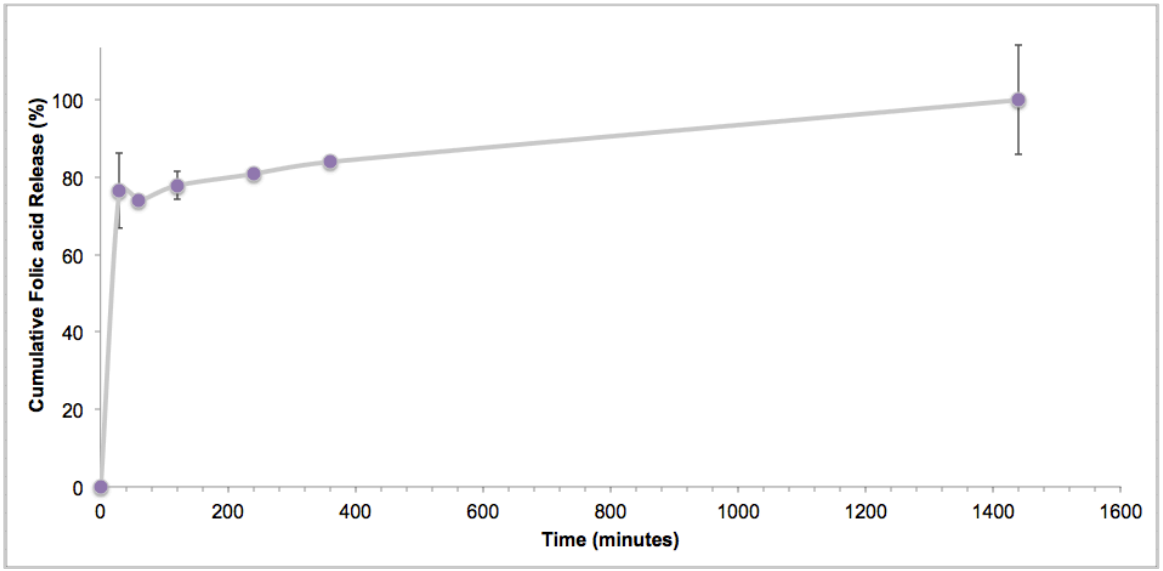

Figure 5-33. The release profile of Fa-LDH in BioSIF (pH 6.5) for 24 hours.

In the acidic medium (pH 1.6), ~ 74% of the vitamin load was released after 30 minutes of the release study. Past 30 minutes, the vitamin release almost comes to an end, where the % release remains almost constant until the end of the two-hour period. In the basic medium (pH 6.5), approximately 77% of the vitamin load was released in the first 30 minutes, while the rest of the vitamin's load (23%) was released over the rest of the experiment's duration, reaching 100% by 24 hours.

Unlike the release properties of B6 from B6-LDH in BioSGF, the release of folate from Fa-LDH is expected to not only be determined by the weathering of the basic LDH structure, as described in section (5.7.1), but also be affected by the solubility of folic acid in the medium. It is expected for Fa-LDH, with its relatively high loading % (65% w/w) and presence of co-intercalated nitrate (as evidence by FTIR), to have a fraction of the loaded folate adsorbed on the surface of the brucite-like sheets. On encountering the acidic conditions of BioSGF, the adsorbed folate anions undergo protonation into folic acid, which is poorly soluble in acidic conditions and would thus form a distinct insoluble phase. Therefore, the release rate of folate in BioSGF becomes controlled by both the weathering rate of Fa-LDH, and the dissolution rate of the undissolved folic acid. Similar results were reported by Rojas et al. who studied the release of the poorly soluble NSAID naproxene from LDH in acidic media (pH 1.2), and compared it to the more soluble drugs: ketoprofen and ibuprofen. It was shown that a pure phase of naproxene existed in the solid material post-exposure to the acidic medium and its dissolution rate was the limiting factor in the drug release profile, as it occurred at a slower rate than the LDH weathering process [163].

In BioSIF, the solubility of folic acid is greatly enhanced. The release of the vitamin takes place, as described for B6, by anion-exchange with phosphate-type anions present in the BioSIF (HPO_4^{2-} and $H_2PO_4^-$). The release profile of Fa-LDH in basic medium described herein exhibits reduced sustained-release properties than those reported by Foraida and Xiao possibly due to the presence of a fraction of the loaded folic acid adsorbed on the LDH surface rather than in intercalated form, and thus is released faster [78, 136].

5.8.2 The Release Profiles of Fa-loaded Composite Beads

Figures 5-34 to 5-36 show the release profiles of folic acid from samples (in order of increasing LDH content): Fa-A/L16, Fa-A/L10 and Fa-A/L4, which were sequentially placed in BioSGF for 2 hours and then in BioSIF for 24 hours.

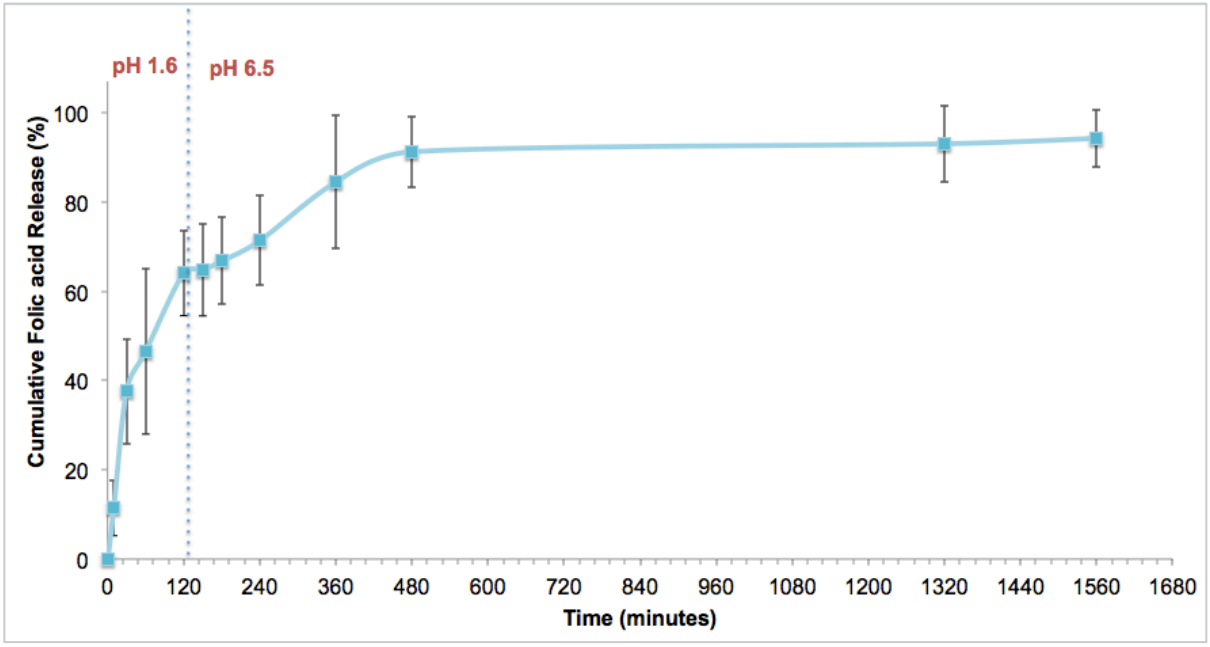

Figure 5-34. The release profile of Fa-A/L16 composite beads (2 h in BioSGF, followed by 24 h in BioSIF).

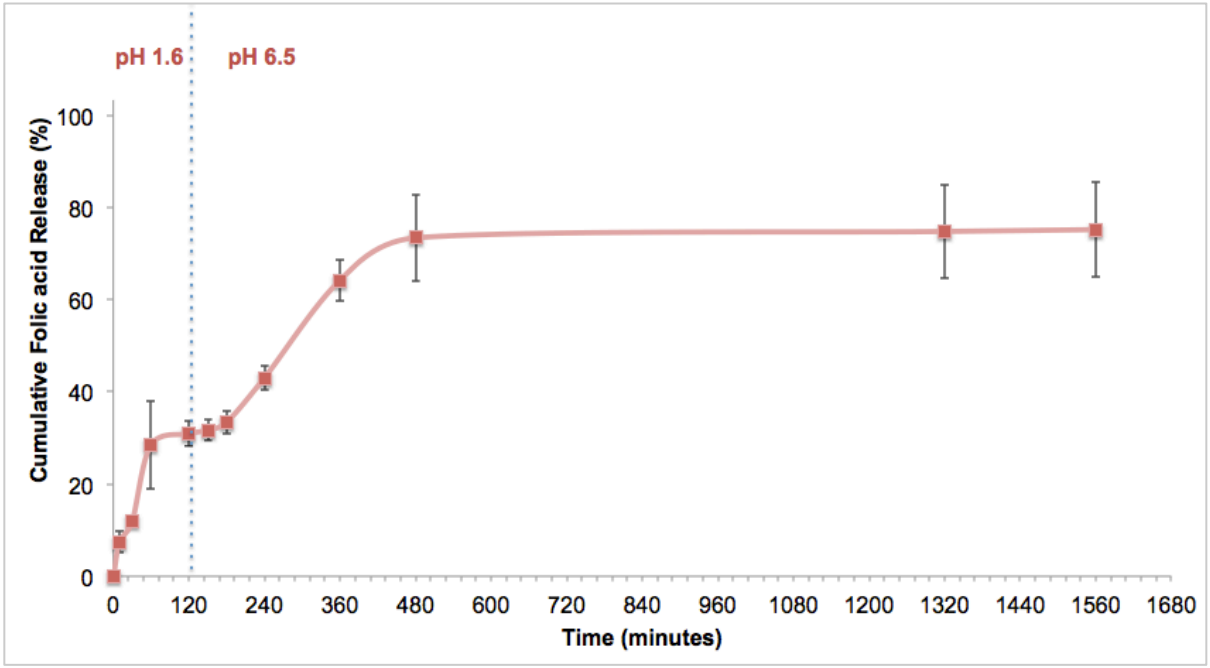

Figure 5-35. The release profile of Fa-A/L10 composite beads (2 h in BioSGF, followed by 24 h in BioSIF).

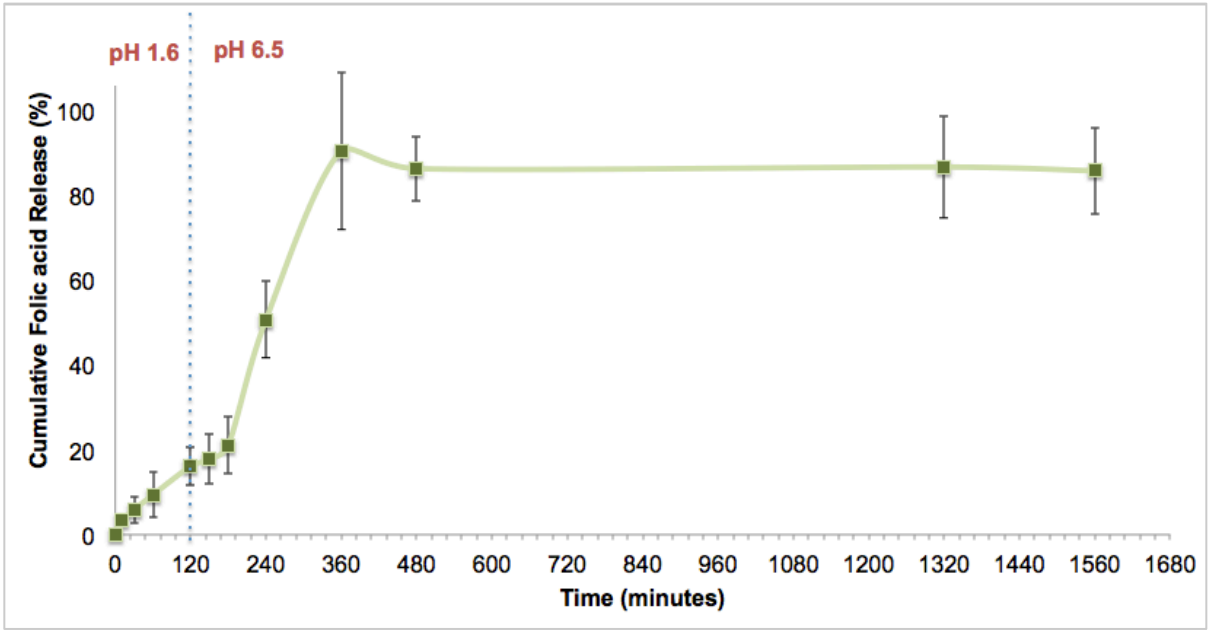

Figure 5-36. The release profile of Fa-A/L4 composite beads (2 h in BioSGF, followed by 24 h in BioSIF).

It is evident from the release profiles that the entrapment of the LDH in the alginate matrix is associated with an improvement of the stability of Fa-LDHs in the acidic medium: a maximum of 64% of the loaded vitamin was released in 2 hours (sample Fa-A/L16) versus 74% from Fa-LDH. The release of folic acid from the folic acid-loaded composite beads exhibit relatively more complex profiles than those observed with B6-loaded ones. A closer look at the release behavior from each composite in both media is presented below.

Figure 5-37 shows a 'magnified' view of the first 2 hours in the release profile of each of the composite beads when placed in BioSGF.

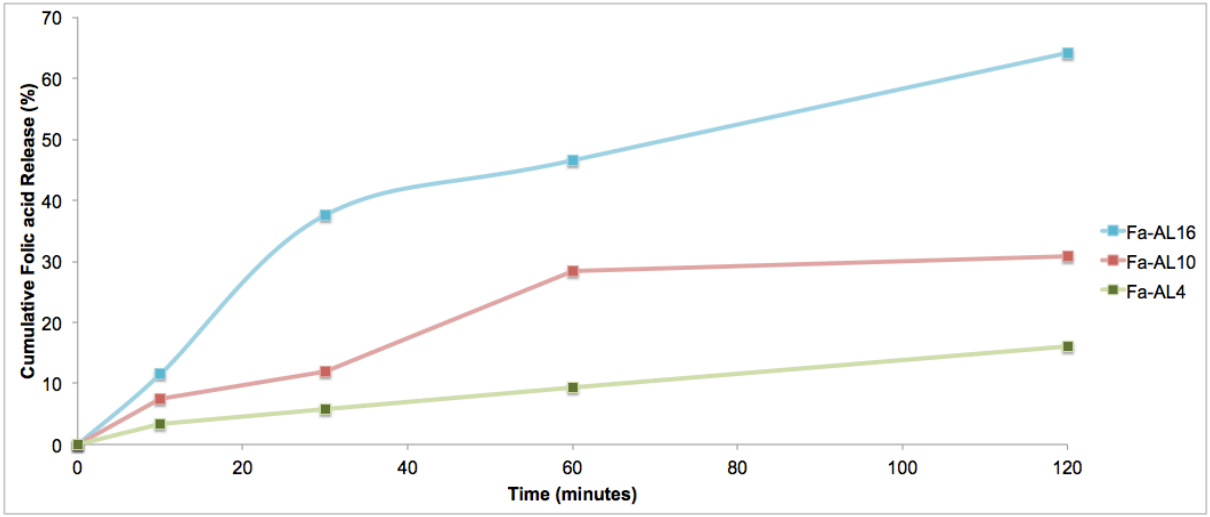

Figure 5-37. The release profiles of the folic acid-loaded composite beads in BioSGF (pH 1.6) for 2 hours.

An obvious trend in the release behavior can be noticed: the increase in the LDH content of the composite beads is associated with a decrease in the release % of the vitamin. During the 2-hour interval in BioSGF, the highest amount of folic acid was released by Fa-A/L16 (~64%) followed by Fa-A/L10 (~31%) and Fa-A/L4 (~16%).

Figure 5-38 shows the release profiles of the composite beads after they were filtered off the BioSGF and placed in the BioSIF for 24 hours.

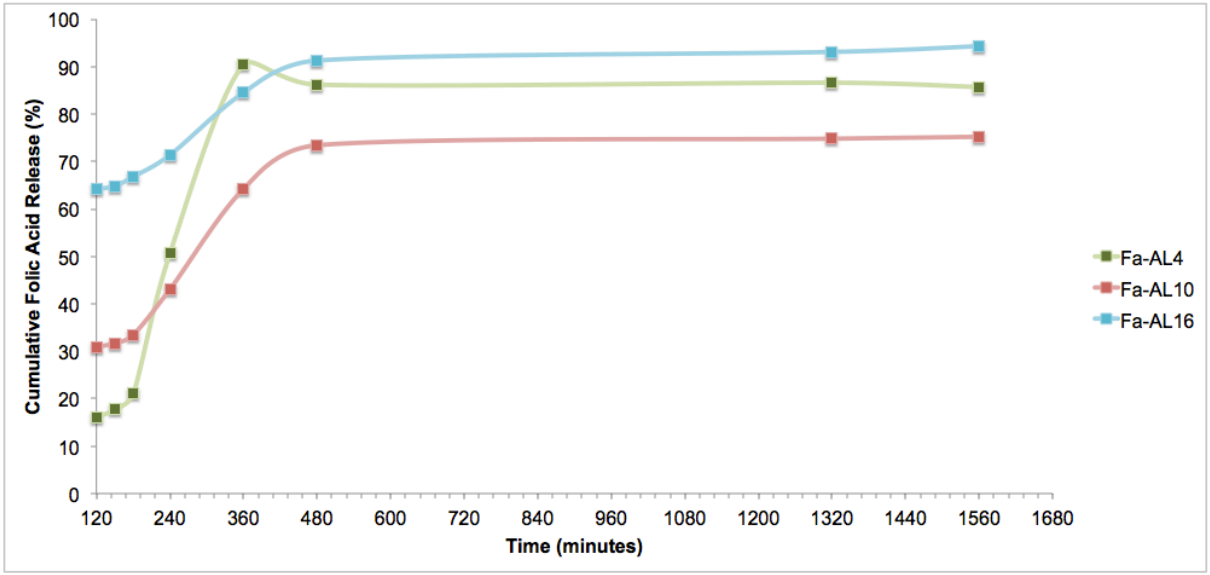

Figure 5-38. The release profiles of the folic acid-loaded composite beads in BioSIF (pH 6.5) for 24 hours.

The release profile of folic acid from the composite beads in basic conditions can be divided into three stages based on the change in the release properties: from 0 -1 hour, from 1 - 6 hours and from 6 - 24 hours. During the first hour in BioSIF, the relative release of the vitamin from Fa-A/L16 and Fa-A/L10 with time was much reduced than their release in BioSGF, releasing only additional ~3.5% and ~2% of their vitamin load, respectively. The relative release from Fa-A/L4 with time was approximately the same as in BioSGF, releasing additional ~ 5% of its folic acid load by the end of the first hour in BioSIF. The second stage (1-6 hours) witnesses a considerable increase in the relative release of the three composites with time: Fa-A/L4 showing the most abrupt increase, and Fa-A/L16 showing the least. Past 1 hour, approximately 24 %, 40 % and 65% of folic acid were released from Fa-A/L16, Fa-A/L10 and Fa-A/L4 during the second stage, respectively. In the third and final stage (6-24 hours), Fa-A/L4 reaches plateau, where no more vitamin than 86% is released past 6 hours until the end of the experiment. Whereas, the release from Fa-A/L16 and Fa-A/L10 proceeds releasing ~ 94% and 75% of their folic acid load by the end of the experiment, respectively.

As was explained for B6-loaded composite beads in BioSGF, the presence of the Fa-LDH in the alginic acid matrix protects it from breaking down in acidic conditions, and improves its stability. This was reflected in the relatively lower release % of folic acid from the composite beads than from Fa-LDH in BioSGF.

If the folic acid release were only driven by the proneness of the beads to acidic attack in BioSGF as their LDH content increases and alginate content decreases, Fa-A/L4 would have exhibited the highest relative release with time and Fa-A/L16 the lowest, as was the case with B6-AL beads. However, the reverse trend was observed, indicating that other factors come into play. As the folic acid-loaded composite beads come in contact with BioSGF, the surface-adsorbed and intercalated folate ions in the dispersed Fa-LDHs get protonated into folic acid, which is poorly soluble and thus regardless of the LDH weathering rate, the dissolution of folic acid becomes the limiting factor. The release of the dissolved folate ions in the core of the beads that manage to get liberated into the release medium becomes mainly governed by their diffusivity in the alginate matrix, from the Fa-LDH to the outside the beads. The main factor that would influence the diffusivity of the folate ions in the alginate matrix is the dispersed LDH phase, which would endow the matrix with barrier properties, that, along with the bulkiness of the folate ions, cause the vitamin release to be hindered, having to adopt more tortuous pathways to diffuse out of the beads. The proposed explanation justifies the release trend of folic-acid loaded composite beads in BioSGF, where the relative release is clearly reduced as the LDH content of the composite beads increases.

As for the situation in BioSIF, contrary to the case of the B6-loaded composite beads, the release trend was not compliant with the swelling trend described in section 5.6. However, the release can be explained in terms of the repulsive forces that would exist between the

ionized forms of both the alginate carboxylate groups and the folate anions, which were apparently more dominant over the release profile than the effect of swelling. As the beads get exposed to BioSIF, their swelling results in the influx of the basic medium, which progressively deprotonates the folic acid formed inside the beads into folate anions (first stage in the release profile). The repulsive forces between the ionized carboxylate groups of the alginate and the folate anions are most pronounced for Fa-A/L4 composite beads, which contain more folate per bead, and thus expel the most folate ions into the release medium, explaining the sharp increase in release % observed in the second stage the release profile. The degree of such expulsion decreases as LDH content (and thus folate) per bead decreases. Similar findings were reported in literature, where it was shown that entrapping 'charged' molecular species in polymer matrices of the same charge results in increasing their fractional release properties [169, 170]. Having expelled most of their negatively-charged folate load by repulsion with the alginate chains, the release of the remaining vitamin load from the beads again becomes a function of its diffusivity in the matrix and de-intercalation by ion exchange with the phosphate ions in the medium as the beads erode, eventually reaching a state of equilibrium.

5.8.3 Summary

Schematic illustrations depicting the effect of the LDH content per composite bead on the release behavior of both vitamins are shown in figure 5-39 (B6-loaded composite beads) and 5-40 (folic acid-loaded composite beads).

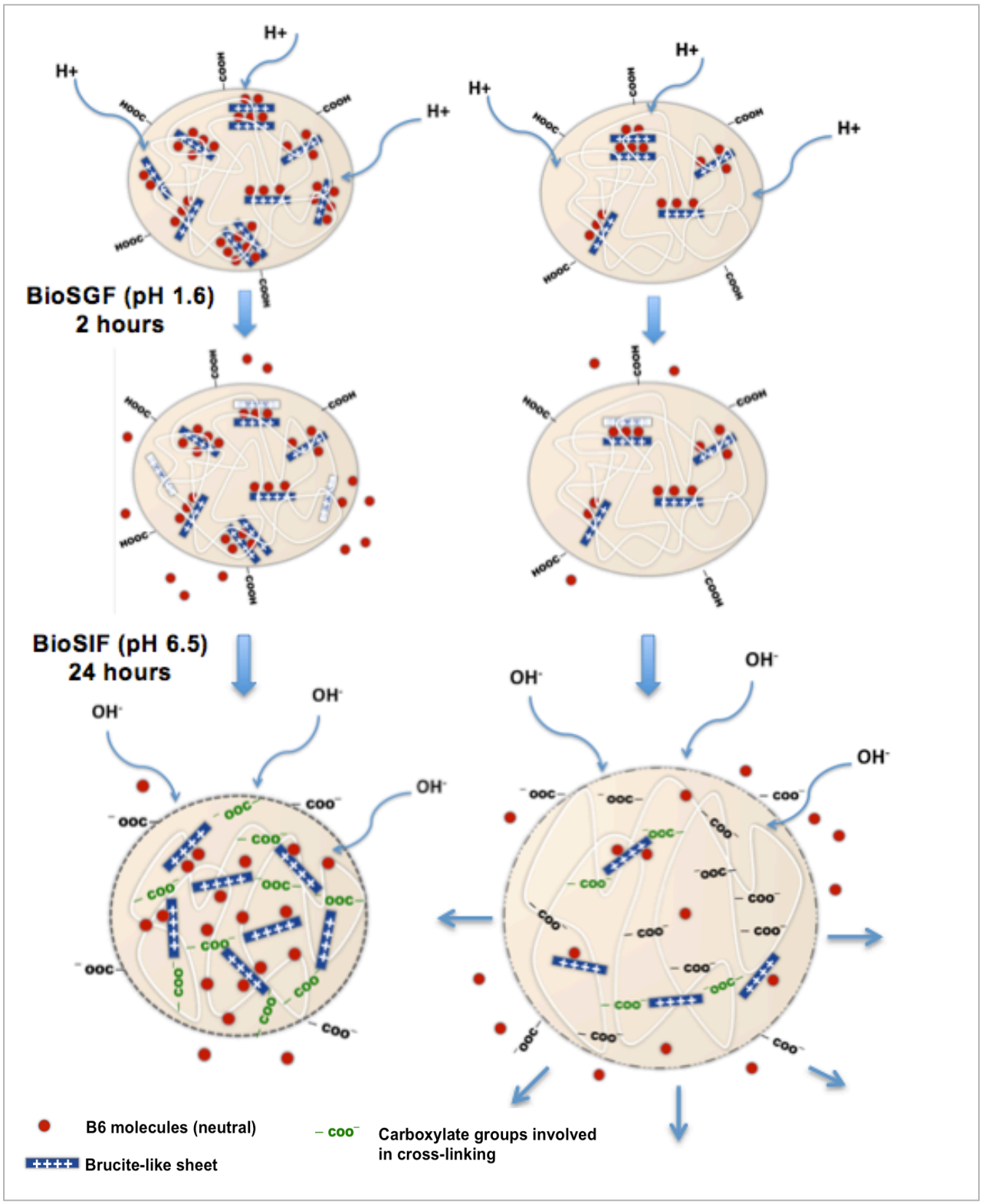

Figure 5-39. A schematic illustration of the proposed explanation for the release behavior of vitamin B6 from the high LDH-content sample B6-A/L4 (left) and the low LDH-content sample B6-A/L16 (right), as they are exposed to BioSGF for 2 hours, then to BioSIF for 24 hours.

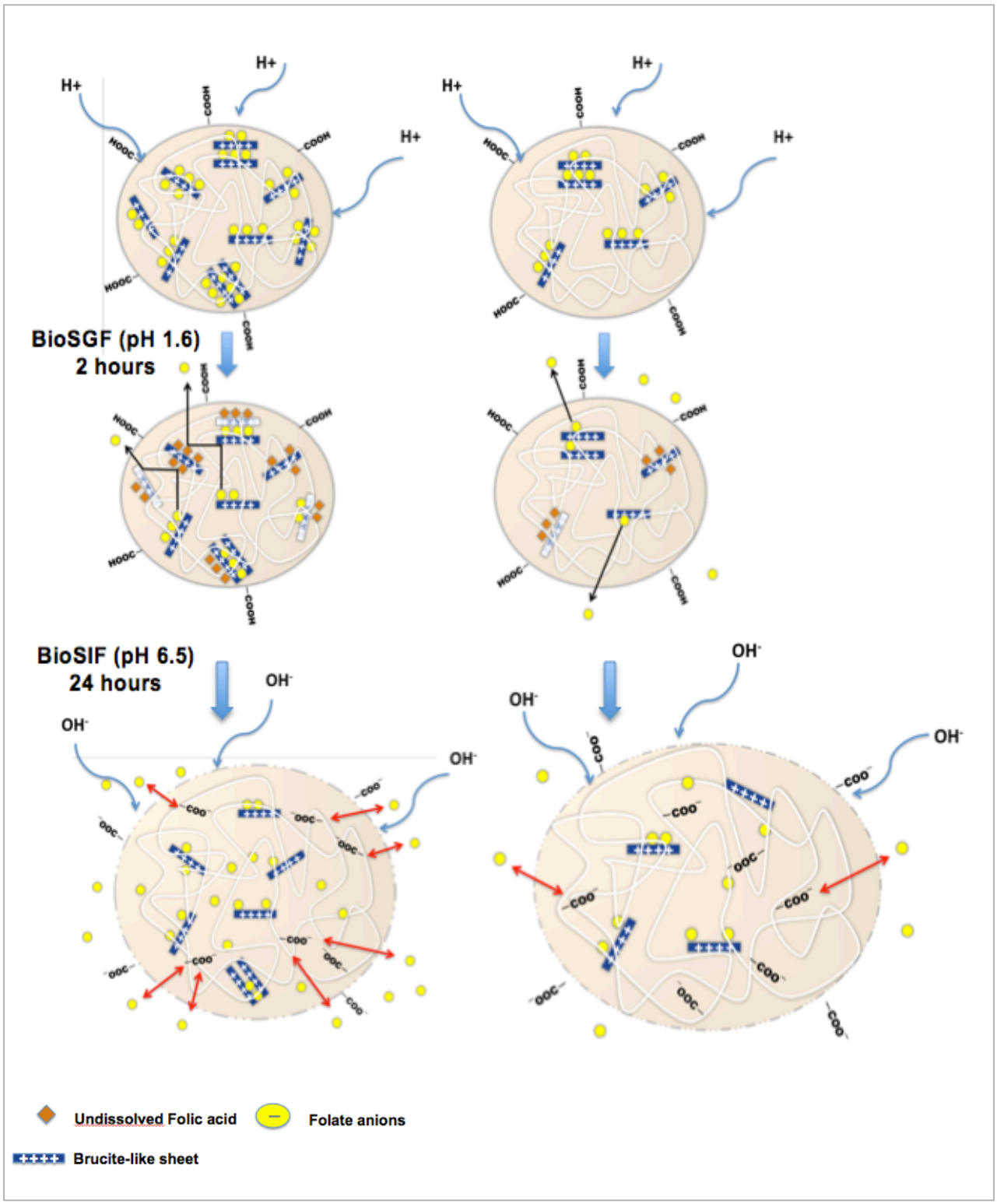

Figure 5-40. A schematic illustration of the proposed explanation for the release behavior of folic acid from the high LDH-content sample Fa-A/L4 (left) and the low LDH-content sample Fa-A/L16 (right), as they are exposed to BioSGF for 2 hours, then to BioSIF for 24 hours.

A summary of the performance of the different release systems investigated in this research is presented in table 5-8.

Table 5-8. A summary of the release performance of the vitamin-loaded composite beads in both BioSGF and BioSIF.

		BioSGF (2 h)		**BioSIF (24 h)**	
Vitamin	**Sample**	**Release %**	**Amount (mg)**	**Release %**	**Amount (mg)**
B6-loaded composite beads (Equivalent to 2.5 mg of B6)	**B6-A/L16**	3%	0.075	100%	2.500
	B6-A/L10	3%	0.075	44%	1.100
	B6-A/L4	7%	0.175	20%	0.500
Folic acid-loaded composite beads (Equivalent to 1.5 mg of folic acid)	**Fa-A/L16**	35%	0.525	94%	1.410
	Fa-A/L10	31%	0.465	73%	1.095
	Fa-A/L4	16%	0.240	83%	1.245

The choice of a satisfactory *oral* controlled-release drug delivery system aims to fulfill a number of criteria. The system must be able to deliver the desired bioactive agent efficiently at its site of action, while providing sustained release properties during its residence time there. Vitamin-loaded LDHs released the majority of their loaded dose early on exposure to the acidic environment simulating the stomach conditions. However, dispersing the vitamin-loaded LDHs in the alginate matrix minimized the release in acidic conditions, and delayed the release of the vitamins until they reached the neutral/basic conditions of the intestinal region. For vitamin B6, sample B6-A/L16 (comprising alginate:LDH ratio of 16:1) shows the most promising release profile. It showed the least loss of the entrapped vitamin in the acidic medium, and after placement in the basic medium, it released 100% of its cargo, in a sustained fashion, during the investigation time, which is more than the maximum residence time of dosage form in the gastrointestinal tract, and thus is considered the most efficient system. For folic acid, the efficiency of the three systems is almost comparable, so one may suggest Fa-A/L4 (comprising alginate:LDH ratio of 4:1), releasing the least of its folic acid load in the acidic conditions, to be the most promising system, as it preserves the major fraction of its loaded dose until it reaches the basic intestinal medium. However, by virtue of its chemical nature, composite beads loaded with folic acid exhibit less sustained release properties than those loaded with B6, when compared over prolonged periods (past 6 hours in the basic medium).

Chapter 6. Conclusion and Future Work

6.1 Conclusion

Based on the findings presented in this investigation, the following can be concluded:

- Vitamin B6- and folic acid-intercalated LDHs are successfully synthesized by coprecipitation. One of the important factors that affect the strength of interaction between the intercalated species and the LDH layers is where the coprecipitation pH stands from the species' pKa value(s), as this determines its predominant molecular form during the reaction.
- Dispersing LDHs in the alginate matrix was found to be associated with the loss of their crystalline features, which indicated that the layers mostly de-laminate in the composite preparation process. We presume that the dispersed cationic LDH layers possibly contribute to the cross-linking of the alginate polymer chains along with the Ca^{2+} ions during gelation, decreasing the porosity as their content per bead increases.
- Entrapment of the LDHs in an alginate matrix was associated with a substantial improvement in their stability on exposure to acidic conditions simulating the gastric environment. Such finding offers a solution to the challenge associated with the use of LDHs as drug-delivery nanocarriers for intestinally absorbed drugs.
- The LDH content in the alginate/LDH composite beads was found to affect their swelling degree.
- The LDH content in the alginate/LDH composite beads was found to play a role in the release behavior of both vitamins in media simulating gastric and intestinal conditions. The resultant effect was also dependent on the ionization status of the intercalated vitamin.
- The release behavior of the vitamins from the alginate/LDH composite is presumed to be a contribution of a number of competing factors: the ionization status of the vitamin in the entrapped LDHs, the solubility of the vitamin in the release medium, the accessibility of the dispersed LDH phase by the release medium (especially in the acidic one), the swelling degree of the beads, and the tortuosity developed in the composite structure by the randomly dispersed LDH nano-sheets. The final release profile is a function of the factors that predominate for each vitamin-loaded beads based on the vitamin's chemical nature and the release medium they are exposed to.
- The neutrality of B6, even though lead to weak interactions with LDH layers, it served the purpose of sustaining the vitamin's release from the alginate/LDH composite throughout the investigated period, which is approximately the maximum residence time of an oral dosage form in the gastrointestinal tract. Sample B6-A/L16, comprising the least LDH content, was found to exhibit the most promising features, delivering 100% of its content by the end of the experiment and in a sustained fashion.

- The anionic nature of the folic acid intercalated in LDHs improved its loading percentage by virtue of its increased interactions with the cationic brucite-like sheets. However, such property worked against the sustainment of release from the composite beads in the basic medium because the alginate matrix assumed the same charge at high pH. Such effect was demonstrated by observing the trend in the vitamin's release on increasing the folic acid-loaded LDH content. Sample Fa-A/L4 was selected to be the most promising amongst the folic acid-loaded systems due to its highest protection of the vitamin's load in the acidic stomach medium.

6.2 Future work

- The developed system of alginate/LDH composites may be extended for other anionic and neutral drugs, in order to improve their release profile in terms of efficient delivery, in addition to delayed and sustained-release properties.
- To make the best use of the advantages of LDHs in such composite with anionic species, the use of a cationic polymer instead of, or combined with alginate can be investigated in attempt to minimize the effect of the repulsive forces between both the entrapped species and alginate on the release in basic media. Examples of such polymers are chitosan and cationic Eudragits.

Chapter 7. References

1. Barahuie, F.; Hussein, M.; Fakurazi, S.; Zainal, Z. Development of Drug Delivery Systems Based on Layered Hydroxides for Nanomedicine. *International Journal of Molecular Sciences.* **2014**, *15,* 5, 7750-7786.
2. Ladewig, K.; Xu, Z. P.; Lu, G. Q. Layered double hydroxide nanoparticles in gene and drug delivery. *Expert Opinion in Drug Delivery*. **2009**, *6,* 9, 907-922.
3. Sosnik, A. Alginate Particles as Platform for Drug Delivery by the Oral Route: State-of-the-Art. *International Scholarly Research Notices: Pharmaceutics*. **2014**.
4. Wen, H.; Park, K. Introduction and overview of oral controlled release formulation design. In *Oral Controlled Release Formulation Design and Drug Delivery: Theory to Practice.* Wen, H.; Park, K., Eds.; John Wiley & Sons Inc, 2010; pp 1-18.
5. Siegel, R.; Rathbone, M. Overview of Controlled Release Mechanisms. In *Fundamentals and Applications of Controlled Release Drug Delivery*. Siepmann, J.; Siegel, R.; Rathbone, M., Eds.; Springer Science & Business Media, 2012; pp 19-43.
6. Ochekpe, N.; Olorunfemi, P.; Ngwuluka, N. Nanotechnology and Drug Delivery Part 1: Background and Applications. *Tropical Journal of Pharmaceutical Research.* **2009**, 8, 3, 265-274.
7. Emeje, M.; Obidike, I.; Akpabio, E.; Ofoefule, S. Nanotechnology in Drug Delivery. In *Recent Advances in Novel Drug Carrier Systems*. Sezer, A., Ed.; In-Tech, 2012; pp 69-106.
8. Li, F.; Duan, X. Applications of Layered Double Hydroxides. In *Layered Double Hydroxides;* Duan, X.; Evans, D. G., Eds.; Springer-Verlag: Berlin, Heidelberg, 2005; pp 193-223.
9. Zhang, K.; Xu, Z.; Lu, J.; Tang, Z.; Zhao, H.; Good, D.; Wei, M. Potential for Layered Double Hydroxides-Based, Innovative Drug Delivery Systems. *International Journal of Molecular Sciences.* **2014**, *15,* 7409-7428.
10. Del Hoyo, C. Layered double hydroxides and human health: An overview. *Applied Clay Science*. **2007,** *36,* 103.
11. Kevadiya, B.; Joshi, G.; Patel, H.; Ingole, P.; Mody, H.; Bajaj, H. Montmorillonite-alginate nanocomposites as a drug delivery system: intercalation and *in-vitro* release of vitamin B1 and vitamin B6. *Journal of Biomaterials Applications.* **2010**, 2, 161-77.
12. Choy, S.; Choy, J. Layered double hydroxide nanoparticles as target-specific delivery carriers: uptake mechanism and toxicity. *Nanomedicine.* **2011**, 6, 5, 803–814.
13. Rodriguesa, L.; Figueirasc, A.; Veigac, F.; de Freitasa, R.; Nunesa, L.; Filhob, E.; Leitea, C. The systems containing clays and clay minerals from modified drug release: A review. *Colloids and Surfaces B: Biointerfaces*. **2013**, 103, 642–651.
14. Sachan, N.; Pushkar, S.; Jha, A.; Bhattcharya, A. Sodium alginate: the wonder polymer for controlled drug delivery. *Journal of Pharmacy Research.* **2009**, 2, 8, 1191-1199.
15. Tonnesen, H.; Karlsen, J. Alginate in Drug Delivery Systems. Drug Development and Industrial Pharmacy. **2002,** 28, 6, 621-30.
16. George, M.; Abraham, T. Polyionic hydrocolloids for the intestinal delivery of protein drugs: Alginate and chitosan: a review. *Journal of Controlled Release*. **2006**, 114, 1–14.
17. Draget, K.; Skjak-Bræk, G.; Stokke, B. Similarities and differences between alginic acid gels and ionically crosslinked alginate gels. *Food Hydrocolloids*. **2006,** 20, 170–

175.

18. Mahkam, M.; Davatgar, M.; Rezvani, Z.; Nejati, K. Preparation of pH-Sensitive Polymers/Layered Double Hydroxide Hybrid Beads for Controlled Release of Insulin. *International Journal of Polymeric Materials*. 2013, 62, 57–60
19. Alcantara, A. C. S.; Aranda, P.; Darder, M.; Ruiz-Hitzky, E. Bionanocomposites based on alginate–zein/layered double hydroxide materials as drug delivery systems. *Journal of Materials Chemistry*. **2010,** *20,* 9495–9504.
20. Lee, K. Y. Alginate: Properties and biomedical applications. *Progress in Polymer Science*. **2011,** *37,* 106-126.
21. Zhang, J.; Wang, Q.; Xie, X.; Li, X.; Wang, A. Preparation and Swelling Properties of pH-Sensitive Sodium Alginate/Layered Double Hydroxides Hybrid Beads for Controlled Release of Diclofenac Sodium. *Journal of Biomedical Materials Research Part B: Applied Biomaterials*. **2010,** *92,* 205-214.
22. Hua, S.; Yang, H.; Li, Q.; Zhang, J.; Wang, A. pH-sensitive sodium alginate/calcined hydrotalcite hybrid beads for controlled release of diclofenac sodium. *Drug Development and Industrial Pharmacy*. **2012**, 38, 6, 728–734.
23. Paula, D.; Robesonb, L. Polymer nanotechnology: Nanocomposites. *Polymer*. **2008**, 49, 3187–3204.
24. Auerbach, S.; Carrado, K.; Dutta, P. *Handbook of layered materials-LDHs.* Marcel Dekker Inc.: USA, 2004.
25. Evans, D. G.; Slade, R. C. T. Structural Aspects of Layered Double Hydroxides. In *Layered Double Hydroxides;* Duan, X.; Evans, D. G., Eds.; Springer-Verlag: Berlin, Heidelberg, **2005**; pp 89-119.
26. Trave, A.; Selloni, A.; Goursot, A.; Tichit, D.; Weber, J. First principles study of the structure and chemistry of Mg based HT-like anionic clays. *Journal of Physical Chemistry B*. **2002**, *106*, 47,12291–12296.
27. Roy, A.; Forano, C.; Besse, J. Layered Double Hydroxides: Synthesis and Post-Synthesis Modifications. In *Layered Double Hydroxides: Present and Future.* Rives, V., Ed.; Nova Science Publishers: New York, 2001; pp 1- 40.
28. Tronto, J.; Bordonal, A. C.; Naal, Z.; Valim, J. B. Conducting Polymers / Layered Double Hydroxides Intercalated Nanocomposites. In *Materials Science-Advanced Topics*. Mastai, Y., Ed.; In-Tech, 2013.
29. Khan, A.; O'Hare, D. Intercalation chemistry of LDHs recent developments and applications. *Journal of Materials Chemistry*. **2002**, 12, 3191–3198.
30. Drits, V.; Bookin, A. Crystal Structure and X-Ray Identification of Layered Double Hydroxides. In *Layered Double Hydroxides: Present and Future.* Rives, V., Ed.; Nova Science Publishers: New York, 2001; pp 41- 100.
31. He, J.; Wei, M.; Li, Bo.; Kang, Y.; Evans, D.; Duan, X. Preparation of layered double hydroxides. In *Layered Double Hydroxides;* Duan, X.; Evans, D. G., Eds.; Springer-Verlag: Berlin, Heidelberg, **2005**; pp 1-87.
32. Forano, C.; Hibino, T.; Leroux, F.; Taviot- Gueho, C. In *Handbook of Clay Science*; Bergaya, F.; Theng, B.; Lagaly, G., Eds.; Developments in Clay Science 1; Elsevier

Ltd.: Netherlands, 2006; pp 1021-1095.
33. Choy, J.; Choi, S.; Oh, J.; Park, P. Clay minerals and layered double hydroxides for novel biological applications. *Applied Clay Science*. **2007**, 36, 122–132.
34. Braccini, I.; Perez, S. Molecular Basis of Ca^{2+}-Induced Gelation in Alginates and Pectins: The Egg-Box Model Revisited. *Biomacromolecules.* **2001**, 2, *1089-1096.*
35. Morris, E.; Rees. D.; Thom, D.; Boyd, J. Chiroptical and stoichiometric evidence of a specific dimerization process in alginate gelation. *Carbohydrate Research.* **1978**, 66, 1, 145-154.
36. Sikorski, P.; Mo, F.; Skjåk-Bræk, G.; Stokke, B. Evidence for Egg-Box-Compatible Interactions in Calcium-Alginate Gels from Fiber X-ray Diffraction. *Biomacromolecules.* **2007**, 8, 2098-2103.
37. Braccini, I.; Grasso, R.; Perez, S. Conformational and configurational features of acidic polysaccharides and their interactions with calcium ions: a molecular modeling investigation. *Carbohydrate Research*. 1999, 317, 119-130.
38. Velings, N.; Mestdagh, M. Physico-Chemical Properties of Alginate Gel Beads. *Polymer Gels and Networks.* 1995, 3, 311-330.
39. Gombotz, W.; Wee, S. Protein release from alginate matrices. *Advanced Drug Delivery Reviews*. **2012**, 64, 194–205.
40. Bajpai, S.; Sharma, S. Investigation of swelling/degradation behaviour of alginate beads crosslinked with Ca2+ and Ba2+ ions. *Reactive & Functional Polymers.* **2004**, 59, 129–140.
41. Martinsen, A.; Skjåk-Bræk, G.; Smidsrod, O. Alginate as immobilization material-correlation between chemical and physical properties of alginate gel beads. *Biotechnology and Bioengineering.* 1989, 33, 79-89.
42. Nussinovitch, A. *Polymer Macro- and Micro-Gel Beads: Fundamentals and Applications*. Springer Science+Business Media, LLC, 2010.
43. Sriamornsak, P.; Thirawong, N.; Korkerd, K. Swelling, erosion and release behavior of alginate-based matrix tablets. *European Journal of Pharmaceutics and Biopharmaceutics.* **2007**, 66, 435–450.
44. Kuo, C.; Ma, P. Maintaining dimensions and mechanical properties of ionically crosslinked alginate hydrogel scaffolds *in-vitro*. *Journal of Biomedical Materials Research Part A.* **2008,** 84, 4, 899-907.
45. Hodsdon, A.; Mitchell, J.; Daviesa, M.; Meliaa, C. Structure and behaviour in hydrophilic matrix sustained release dosage forms: 3. The influence of pH on the sustained-release performance and internal gel structure of sodium alginate matrices. *Journal of Controlled Release.* **1995**, 33, 143-152.
46. Omidian, H.; Park, K. Hydrogels. In *Fundamentals and Applications of Controlled Release Drug Delivery*. Siepmann, J.; Siegel, R.; Rathbone, M., Eds.; Springer Science & Business Media, 2012; pp 75-105.
47. Bender, D. A. *Nutritional Biochemistry of the Vitamins,* 2nd ed.; Cambridge University Press: UK, 2003; pp 232-323.
48. Eitenmiller, R.; Landen Jr, W; Ye, L. *Vitamin Analysis for the Health and Food Sciences*. CRC Press LLC, 1999; pp 401-506.
49. Ristila, M.; Matxain, J. M.; Strid, A.; Eriksson, L. A. pH-Dependent Electronic and Spectroscopic Properties of Pyridoxine (Vitamin B6). *Journal of Physical Chemistry*

B. **2006**, 110, 16774-16780.
50. Dos Santos, T.; Da Costa, D.; Pita, S.; Semaan, F. Potentiometric and conductimetric studies of chemical equilibria for pyridoxine hydrochloride in aqueous solutions: simple experimental determination of pka values and analytical applications to pharmaceutical analysis. *Ecletica Quimica.* **2010**, 35, 4, 81-86.
51. Lunn, A. K.; Morton, R. A. Ultra-violet Absorption Spectra of Pyridoxine and Related Compounds. *Analyst*. **1952**, 77, 718-731.
52. Combs, G. *The Vitamins: Fundamental Aspects in Nutrition and Health*, 4th ed.; Elsevier Inc.: USA, 2012.
53. Madziva, H.; Kailasapathy, K.; Phillips, M. Alginate-pectin microcapsules as a potential for folic acid delivery in foods. *Journal of Microencapsulation.* **2005,** 22, 4, 343-351.
54. Matias, R.; Ribeiro, P. R. S.; Sarraguca, M. C. Lupes, J. A. A UV spectrophotometric method for the determination of folic acid in pharmaceutical tablets and dissolution tests. *Analytical Methods*. **2014**, 6, 3065-3071.
55. Cooper, B. A. Physiology of Absorption of Monoglutamyl Folates From the Gastrointestinal Tract. In *Folic Acid: Biochemistry and Physiology in Relation to the Human Nutrition Requirements: Proceedings of a Workshop on Human Folate Requirements, Washington, D.C., June 2-3, 1975.* National Academy of Sciences, 1977; p. 195.
56. Poe, M. Acidic dissociation constants of folic acid, dihydrofolic acid, and methotrexate. *The Journal of Biological Chemistry*. **1977**, 252, 11, 3724-3728.
57. Greogry, J. Chemical and Nutritional Aspects of Folate Research. In *Advancs In Food & Nutrition Research*. Kinsella, J. E., Ed.; Academic Press Inc., 1989; pp 2-80.
58. Alborzi, S.; Lim, L.; Kakuda, Y. Release of folic acid from sodium alginate-pectin-poly(ethylene oxide) electrospun fibers under *in-vitro* conditions. *LWT - Food Science and Technology.* **2014**, 59, 383-388.
59. Bajpai, S.; Tankhiwale, R. Investigation of dynamic release of vitamin B2 from calcium alginate/chitosan multilayered beads: Part II. *Reactive & Functional Polymers.* **2006**, 66, 1565–1574.
60. Xu, Y.; Zhan, C.; Fan, L.; Wang, L.; Zheng, H. Preparation of dual crosslinked alginate–chitosan blend gel beads and *in-vitro* controlled release in oral site-specific drug delivery system. *International Journal of Pharmaceutics*. **2007**, 336, 329–337.
61. Yanga, J.; Chena, J.; Pana, D.; Wanc, Y.; Wanga, Z. pH-sensitive interpenetrating network hydrogels based on chitosan derivatives and alginate for oral drug delivery. *Carbohydrate Polymers.* **2013,** 91, 1, 719–725.
62. Čalijaa, B.; Cekićb, N.; Savića, S.; Daniels. R.; Markovićd, B.; Milića, J. pH-sensitive microparticles for oral drug delivery based on alginate/oligochitosan/Eudragit L100-55 "sandwich" polyelectrolyte complex. *Colloids Surf B Biointerfaces*. **2013**, 110, 1, 395-402.
63. Feng, C.; Song, R.; Sun, G.; Kong, M.; Bao, Z.; Li, Y.; Cheng, X.; Cha, D.; Park, H. Immobilization of coacervate microcapsules in multilayer sodium alginate beads for efficient oral anticancer drug delivery. *Biomacromolecules.* **2014**, 15, 3, 985-996.
64. Yegin, B.; Moulari, B.; Durlu-Kandilci, N.; Korkusuz, P.; Pellequer, Y.; Lamprecht, A. Sulindac loaded alginate beads for a mucoprotective and controlled drug release. *Journal of Microencapsulation*. **2007**, 24, 371–382.

65. Rastogi, R.; Sultana, Y.; Aqil, M.; Ali, A.; Kumar, S.; Chuttani, K.; Mishra, A. K. Alginate microspheres of isoniazid for oral sustained drug delivery. *International Journal of Pharmaceutics*. **2007**, 334, 71–77.
66. Soni, M. L.; Kumar, M.; Namdeo, K. P. Sodium alginate microspheres for extending drug release: formulation and *in-vitro* evaluation. *International Journal of Drug Delivery.* **2010**, 2, 1, 64-68.
67. Mandal, S.; Kumar, S.; Krishnamoorthy, B.; Basu, S. Development and evaluation of calcium alginate beads prepared by sequential and simultaneous methods. *Brazilian Journal of Pharmaceutical Sciences*. **2010**, 46, 4, 785-793.
68. Singh, M. P.; Alam, G.; Patel, R.; Kumar, U.; Singh, A. *In-vitro* evaluation of polymeric beads of riboflavin formulated at different cross-linking time. *Der Pharmacia Lettre*. **2010**, 2, 4, 164-171.
69. Anifantaki, E.; Touloupakis, E.; Ghanotakis, D. F. Allinase immobilization in calcium alginate beads and layered double hydroxides matrices. *Journal of Food Biochemistry*. **2012**, 36, 1, 12–20.
70. Jelvehgari, M.; Mobaraki, V.; Montazam, S. H. Algino-Pectinate of Piroxicam for Colon-Specific Drug Delivery Via Oral route. *Jundishapur Journal of Natural Pharmaceutical Products*. **2014**, 9, 4, e16576.
71. Doi, N.; Nitta, S.; Kusari, M.; Takahashi, N. Preparation of sustained-release pharmaceuticals containing nifedipine. *Japanese Kokai Tokkyo Koho*. **1985**, 60, 255, 719.
72. Hwang, S.; Han, Y.; Choy, J. Intercalation of Functional Organic Molecules with Pharmaceutical, Cosmeceutical and Nutraceutical Functions into Layered Double Hydroxides and Zinc Basic Salts. *Bulletin of Korean Chemical Society.* **2001,** 22, 9, 1019-1022.
73. Choy, J.; Son, Y. Intercalation of Vitamer into LDH and Their Controlled Release Properties. *Bulletin of Korean Chemical Society.* **2004,** 25, 1, 122-126.
74. Gasser, M. S. Inorganic layered double hydroxides as ascorbic acid (vitamin C) delivery system—Intercalation and their controlled release properties. *Colloids and Surfaces B: Biointerfaces.* **2009**, 73, 1, 103–109.
75. Gao, X.; Lei, L.; O'Hare, D.; Xie, J.; Gao, P.; Chang, T. Intercalation and controlled release properties of vitamin C intercalated layered double hydroxide. *Journal of Solid State Chemistry.* **2013***,* 203, 174–180.
76. Gao, X.; Chen, L.; Xie, J.; Yin, Y.; Chang, T.; Duan, Y.; Jiang, N. *In-vitro* controlled release of vitamin C from Ca/Al layered double hydroxide drug delivery system. *Materials Science and Engineering C.* **2014**, 39, 56–60.
77. Qin, L.; Wang, S.; Zhang, R.; Zhu, R.; Sun, X.; Yao, S. Two different approaches to synthesizing Mg–Al-layered double hydroxides as folic acid carriers. *Journal of Physics and Chemistry of Solids.* **2008,** 69, 2779–2784.
78. Xiao, R.; Wang, W.; Pan, L.; Zhu, R.; Yu, Y.; Li, H.; Liu, H.; Wang, S. A sustained folic acid release system based on ternary magnesium/ zinc/aluminum layered double hydroxides. *Journal of Materials Science*. **2011**, 46, 8, 2635–2643.
79. Bashi, A.; Haddawi, S.; Mezaal, M. Layered Double Hydroxides Nanohybrid Intercalation with Folic Acid Used as Delivery System and their Controlled Release Properties. *Journal for Science and Engineering*. **2013**, 38, 7, 1663–1680.
80. Qin, L.; Wang, W.; You, S.; Dong, J.; Zhou, Y.; Wang, J. *In-vitro* antioxidant activity

and *in-vivo* antifatigue effect of layered double hydroxide nanoparticles as delivery vehicles for folic acid. *International Journal of Nanomedicine.* **2014,** 9, 5701–5710.
81. Kim, T.; Oh, J. Dual nutraceutical nanohybrids of folic acid and calcium containing layered double hydroxides. *Journal of Solid State Chemistry*. **2016**, 233, 125–132.
82. Silion, M.; Hritcu, D.; Lisa, G.; Popa, M. New hybrid materials based on layered double hydroxides and antioxidant compounds: Preparation, characterization and release kinetic studies. *Journal of Porous Materials*. **2012**, 19, 3, 267-276.
83. Kong, C.; Jin, L.; Wei, M.; Duan, X. Antioxidant drugs intercalated into layered double hydroxide: Structure and *in-vitro* release. *Applied Clay Science*. **2010**, 49, 3, 324–329.
84. Kovanda, F.; Maryskova, Z.; Kovar, P. Intercalation of paracetamol into the hydrotalcite-like host. *Journal of Solid State Chemistry.* **2011**, 184, 12, 3329–3335.
85. Silion, M.; Hritcu, D.; Jaba, I.; Tamba, B.; Ionescu, D.; Mungiu, O.; Popa, I. *In-vitro* and in vivo behavior of ketoprofen intercalated into layered double hydroxides. *Journal of Materials Science: Materials in Medicine*. **2010**, 21, 11, 3009–3018.
86. Caoa, F.; Wanga, Y.; Pinga, G.; Liao, Z. Zn–Al–NO3-layered double hydroxides with intercalated diclofenac for ocular delivery. *International Journal of Pharmaceutics*. **2011**, 404, 1-2, 250–256.
87. Minagawa, K.; Berber, M.; Hafez, I.; Mori, T.; Tanaka, M. Target delivery and controlled release of the chemopreventive drug sulindac by using an advanced layered double hydroxide nanomatrix formulation system. *Journal of Materials Science: Materials in Medicine*. **2012**, 23, 4, 973–981.
88. Chakraborty, M.; Dasgupta, S.; Soundrapandian, C.; Chakraborty, J.; Ghosh, S.; Mitra, M.; Basu, D. Methotrexate intercalated ZnAl-layered double hydroxide. *Journal of Solid State Chemistry*. **2011,** 184, 9, 2439–2445.
89. Chakraborty, J.; Roychowdhury, S.; Sengupta, S.; Ghosh, S. Mg–Al layered double hydroxide–methotrexate nanohybrid drug delivery system: Evaluation of efficacy. *Materials Science and Engineering C*. **2013**, 33, 4, 2168–2174.
90. Chakraborty, M.; Dasgupta, S.; Sengupta, S.; Chakraborty, J.; Ghosh, S.; Ghosh, J.; Mitra, M.; Mishra, A.; Mandal, T.; Basu, D. A facile synthetic strategy for Mg–Al layered double hydroxide material as nanocarrier for methotrexate. *Ceramics International.* **2012**, 38, 2, 941–949.
91. Chakraborty, M.; Dasgupta, S.; Bose, P.; Misra, A.; Mandal, T.; Mitra, M.; Chakraborty, J.; Basu, D. Layered double hydroxide: Inorganic organic conjugate nanocarrier for methotrexate. *Journal of Physics and Chemistry of Solids*. **2011**, 72, 6, 779–783.
92. Qin, L.; Wang, M.; Zhu, R.; You, S.; Zhou, P.; Wang, S. The *in-vitro* sustained release profile and antitumor effect of etoposide-layered double hydroxide nanohybrids. *International Journal of Nanomedicine*. **2013**, 8, 2053-2064.
93. Li, L.; Gu, W.; Chen, J.; Chen, W.; Xu, Z. Co-delivery of siRNAs and anti-cancer drugs using layered double hydroxide nanoparticles. *Biomaterials.* **2014,** 35, 10, 3331-3339.
94. Barahuie, F.; Hussein, M.; Arulselvan, P.; Fakurazi, S.; Zulkarnain, Z. Drug delivery system for an anticancer agent, chlorogenate-Zn/Al-layered double hydroxide nanohybrid synthesized using direct co-precipitation and ion exchange methods. *Journal of Solid State Chemistry*. **2004**, 217, 31-41.

95. Barahuie, F.; Hussein, M.; Abd Gani, S.; Fakurazi,S.; Zainal, Z. Synthesis of protocatechuic acid–zinc/aluminium–layered double hydroxide nanocomposite as an anticancer nanodelivery system. *Journal of Solid State Chemistry*. **2015**, 221, 21–31.
96. Al Ali, S.; Al-Qubaisi, M.; Hussein, M.; Ismail, M.; Zainal, Z.; Hakim, M. Comparative study of Mg/Al- and Zn/Al-layered double hydroxide-perindopril erbumine nanocomposites for inhibition of angiotensin-converting enzyme. *International Journal of Nanomedicine*. **2012**, 7, 4251–4262.
97. Perioli, L.; Mutascio, P.; Pagano, C. Influence of the Nanocomposite MgAl-HTlc on Gastric Absorption of Drugs: *In-Vitro* and *Ex-Vivo* Studies. *Pharmaceutical Research*. **2013**, 30, 1, 156-166.
98. Tu, J.; Shen, Y.; Mahalingam, R.; Jasti, B.; Li, X. Polymers in Oral Modified Release Systems. In *Oral Controlled Release Formulation Design and Drug Delivery: Theory to Practice.* Wen, H.; Park, K., Eds.; John Wiley & Sons Inc, 2010; pp 71-88.
99. Arco, M.; Fernandez, A.; Martin, C.; Rives, V. Solubility and release of fenbufen intercalated in Mg, Al and Mg, Al, Fe layered double hydroxides (LDH): The effect of Eudragits S 100 covering. *Journal of Solid State Chemistry*. **2010**, 183, 12, 3002–3009.
100. Pan, D.; Zhang, H.; Zhang, T.; Duan, X. A novel organic–inorganic microhybrids containing anticancer agent doxifluridine and layered double hydroxides: Structure and controlled release properties. *Chemical Engineering Science.* **2010**, 65, 12, 3762–3771
101. Kim, T.; Lee, J.; Choi, S.; Oh, J. Polymer Coated CaAl-Layered Double Hydroxide Nanomaterials for Potential Calcium Supplement. *International Journal of Molecular Science*. **2014**, 15, 12, 22563-22579.
102. Kankala, R.; Kuthati, Y.; Sie, H.; Shih, H.; Lue, S.; Kankala, S.; Jeng, C.; Deng, J.; Weng, C.; Liu, C.; Lee, C. Multi-laminated metal hydroxide nanocontainers for oral-specific delivery for bioavailability improvement and treatment of inflammatory paw edema in mice. *Journal of Colloid and Interface Science.* **2015**, 458, 217–228.
103. Barkhordari, S.; Yadollahi, M.; Namazi, H. pH sensitive nanocomposite hydrogel beads based on carboxymethyl cellulose/layered double hydroxide as drug delivery systems. *Journal of Polymer Research.* **2014**, 21, 454.
104. Ribeiroa, L.; Alcântaraa, A.; Dardera, M.; Arandaa, P.; Araújo-Moreirab, F.; Ruiz-Hitzkya, E. Pectin-coated chitosan–LDH bionanocomposite beads as potential systems for colon-targeted drug delivery. *International Journal of Pharmaceutics*. **2014**, 463, 1–9.
105. Stevanovic, M.; Radulovic, A.; Jordovic, B.; Uskokovic, D. Poly(DL-lactide-co-glycolide) Nanospheres for the Sustained Release of Folic Acid. *Journal of Biomedical Nanotechnology*. **2008**, 4, 3, 1-10.
106. Joshi, G.; Patel, H.; Bajaj , H.; Jasra, R. Intercalation and controlled release of vitamin B6 from montmorillonite–vitamin B6 hybrid. *Colloid and Polymer Science*. **2009**, 287, 9, 1071-1076.
107. Skoog, D. A.; West, D. M. *Principles of instrumental analysis*, 2nd ed.; Saunder's college: Philadelphia, 1980.
108. Waseda, Y.; Matsubara, E.; Shinoda; K. *X-Ray Diffraction Crystallography: Introduction, examples and solved problems*. Springer-Verlag Berlin Heidelberg,

2011.
109. Bruker Corporation: How Does XRF Work? https://www.bruker.com/products/x-ray-diffraction-and-elemental-analysis/handheld-xrf/how-xrf-works.html (accessed March 1st, 2016)
110. Alford, T. L.; Feldman, L. C.; Mayer, J. W. *Fundamentals of Nanoscale Film Analysis*. Springer Science + Business Media, Inc: New York, 2007; pp 129-149.
111. University of Illinois: Development of X-ray Crystallography. https://publish.illinois.edu/x-raycrystallography/2014/12/18/introduction/ (accessed March 1st, 2016)
112. Atkins, P.; Paula, J. *Atkins' Physical Chemistry,* 8th ed.; Oxford University Press: Great Britain, 2006.
113. Birkbeck College, University of London: Choice of X-ray Target. http://pd.chem.ucl.ac.uk/pdnn/inst1/xrays.htm (accessed March 1st, 2016).
114. Lassner, E.; Schubert, W. *Tungsten: Properties, Chemistry, Technology of the Element, Alloys, and Chemical Compounds*. Springer Science+Business Media: New York, 1999; p. 4.
115. Fultz, B.; Howe, J. Diffraction and the X-Ray Powder Diffractometer. In *Transmission Electron Microscopy and Diffractometry of Materials;* Springer-Verlag Berlin Heidelberg, 2013; pp 1-59.
116. Suryanarayana, C.; Norton, M. G. *X-Ray Diffraction: A Practical Approach.* Springer Science+Business Media: New York, 1998.
117. Pavia, D. L.; Lampman, G. M.; Kriz, G. S.; Vyvyan, J. A. Ultraviolet Spectroscopy. In *Introduction to Spectroscopy*, 4th ed.; Cengage Learning: Canada, 2009; pp 381-417.
118. Förster, H. UV/VIS Spectroscopy. In *Molecular Sieves - Science and Technology;* Karge, H. G.; Weitkamp, J. Eds.; Springer-Verlag Berlin Heidelberg, 2004; pp 337–426.
119. Perkampus, H. *UV-VIS Spectroscopy and Its Applications.* Springer-Verlag Berlin Heidelberg, 1992; pp 1-24.
120. Stuart, B. H. *Infrared Spectroscopy: Fundamentals and Applications.* John Wiley & Sons Ltd: England, 2004; pp 1-44.
121. Larkin, P. *Infrared and Raman Spectroscopy; Principles and Spectral Interpretation.* Elsevier: USA, 2011; pp 1-54.
122. Jaggi, N.; Vij, D. R. Fourier Transform Infrared Spectroscopy. In *Handbook of Applied Solid State Spectroscopy.* Vij, D.R., Ed.; Springer Science+Business Media LLC: USA, 2006; pp 411-450.
123. Rouquerol, J.; Rouquerol, F.; Llewellyn, P.; Maurin, G.; Sing, K. *Adsorption by Powders and Porous Solids: Principles, Methodology and Applications.* Academic Press: UK, 1999.
124. Carberry, J. *Chemical and Catalytic Reaction Engineering*. Dover Publications Inc.: New York, 2001; pp 357-456.
125. Masel, R. *Principles of Adsorption and Reaction on Solid Surfaces.* John Wiley & Sons Inc.: USA, 1996; pp 108-234.
126. Gregg, S.; Sing, K. *Adsorption, Surface Area and Porosity*, 2nd ed.; Academic Press: New York, 1976.
127. Balbuena, P.; Lastoskie, C.; Gubbins, K.; Quirke, N. Theoretical Interpretation and

Classification of Adsorption Isotherms for Simple Fluids. In *Fundamentals of Absorption.* Suzuki, M., Ed.; Kodansha Ltd: Tokyo, 1993; p. 27.
128. Gubbins, K. E. Hysteresis Phenomena in Mesoporous Materials. Dissertation, Universität Leipzig, Leipzig, Germany, 2009.
129. Thommes, M. Physical Adsorption Characterization of Nanoporous Materials. *Chemie Ingenieur Technik*. **2010,** 82, 1059–1073.
130. Sing, K.; Williams, R. Physisorption Hysteresis Loops and the Characterization of Nanoporous Materials. *Adsorption Science and Technology*. **2004**, 22, 773-782.
131. Particle Analytical: Brunauer, Emmett and Teller (BET) Theory. http://particle.dk/methods-analytical-laboratory/surface-area-bet/surface-area-bet-theory/ (accessed March 2nd, 2016).
132. Baron, A. R. Physical Methods in Chemistry and Nano Science: BET Surface Area Analysis of Nanoparticles. http://cnx.org/contents/uieDnVBC@21.1:9cBY4EHy@1/BET-Surface-Area-Analysis-of-N (accessed March 11th, 2016).
133. Lowell, S.; Shields, J. E. *Powder Surface Area and Porosity*, 2nd ed.; Chapman and Hall Ltd: London, 1984; pp 14-29.
134. Sing, K. The use of nitrogen adsorption for the characterization of porous materials. *Colloids and Surfaces A: Physicochemical and Engineering Aspects*. **2001**, 187–188, 3–9.
135. Sing, K. Adsorption methods for the characterization of porous materials. *Advances in Colloid and Interface Science*. **1998**, 76-77, 3-11.
136. Foraida, Z.; Ramadan, A. Zn-Al And Mg-Al Layered Double Hydroxides As Nanostructured Carriers For Vitamins. M. Sc. Thesis, The American University in Cairo, Cairo, Egypt, 2012.
137. Cho, A. R.; Chun, Y. G.; Kim, B. K.; Park, D. J. Preparation of alginate-$CaCl_2$ microspheres as resveratrol carriers. Journal of Materials Science. 2014, 49, 4612-4619.
138. Why run dissolution tests in Biorelevant media?. http://biorelevant.com/biorelevant-media/dissolution-tests/ (accessed March 11th, 2016).
139. Cavani, F.; Trifirò, F.; Vaccari, A. Hydrotalcite-type anionic clays: preparation, properties and applications. *Catalysis Today.* **1991**, 11, 2, 173-301.
140. Miyata, S.; The Syntheses of Hydrotalcite-Like Compounds and Their Structures and Physico-Chemical Properties I: The Systems Mg^{2+}-Al^{3+}-NO_3^-, Mg^{2+}-Al^{3+}-Cl^-, Mg^{2+}-Al^{3+}-ClO_4^-, Ni^{2+}-Al^{3+}-Cl^- and Zn^{2+}-Al^{3+}-Cl^-. *Clays and Clay Minerals.* **1975,** 23, 369-375.
141. Kloprogge, J.T.; Hickey, L.; Frost, R.L. The effect of varying synthesis conditions on zinc chromium hydrotalcite: a spectroscopic study. *Materials Chemistry and Physics*. **2005**, 89, 1, 99-109.
142. Kloprogge, J. T.; Hickey, L.; Frost, R. L. The effects of synthesis pH and hydrothermal treatment on the formation of zinc aluminum hydrotalcites. *Journal of Solid State Chemistry.* **2004**, 177, 4047–4057.
143. Seftel, E.; Popovici, E.; Mertens, M.; De Witte, K.; Tendeloo, G.; Cool, P.; Vansant, E. F. Zn–Al layered double hydroxides: Synthesis, characterization and photocatalytic application. *Microporous and Mesoporous Materials.* **2008**, 113, 296–304.

144. Velu, S.; Ramkumar, V.; Narayanan, A.; Swamy, C. S. Effect of interlayer anions on the physicochemical properties of zinc–aluminium hydrotalcite-like compounds. *Journal Of Materials Science.* **1997**, 32, 957-964.
145. Kannan, S.; Swamy, C. S. Synthesis and physicochemical characterization of cobalt aluminium hydrotalcite. *Journal Of Materials Science Letters.* **1992**, 11, 1585-1587.
146. Cocheci, L.; Barvinschi, P.; Pode, R.; Popovici. E.; Seftel. E. M. Structural Characterization of Some Mg/Zn-Al Type Hydrotalcites Prepared for Chromate Sorption from Wastewater. *Chemical Bulletin of "Politehnica" University of Timisoara*. **2010,** 55, 40-45.
147. Mandal, S.; Mayadevi, S. Adsorption of fluoride ions by Zn–Al layered double hydroxides. *Applied Clay Science*. **2008**, 40, 54–62.
148. Li, F.; Jiang, X.; Evans, D. G.; Duan, X. Structure and Basicity of Mesoporous Materials from Mg/Al/In Layered Double Hydroxides Prepared by Separate Nucleation and Aging Steps Method. *Journal of Porous Materials*. **2005**, 12, 55–63.
149. Mandal, S.; Patil, V. S.; Mayadevi, S. Alginate and hydrotalcite-like anionic clay composite systems: Synthesis, characterization and application studies. *Microporous and Mesoporous Materials*. **2012**, 158, 241–246.
150. Srivastava, M.; Rani, P.; Singh, N. P.; Yadav, R. A. Experimental and theoretical studies of vibrational spectrum and molecular structure and related properties of pyridoxine (vitamin B6). *Spectrochimica Acta Part A: Molecular and Biomolecular Spectroscopy.* **2014**, 120, 274–286.
151. Marques, S.; Bueno, W. Infrared Spectra of Inorganic Hydrogen Bond Complexes of Pyridoxine. *Spectroscopy Letters: An International Journal for Rapid Communication.* **1996**, 29, 8, 1523-1530.
152. Nakayama, H.; Wada, N.; Tsuhako, M. Intercalation of amino acids and peptides into Mg–Al layered double hydroxide by reconstruction method. *International Journal of Pharmaceutics*. **2004**, 269, 469–478.
153. Choy, J.; Junga, J.; Oh, J.; Parka, M.; Jeongb, J.; Kangb, Y.; Han, O. Layered double hydroxide as an efficient drug reservoir for folate derivatives. *Biomaterials*. **2004**, 25, 3059–3064.
154. Peretz, S.; Anghel, D. F.; Vasilescu, E.; Florea-Spiroiu, M.; Stoian, C.; Zgherea, G. Synthesis, characterization and adsorption properties of alginate porous beads. *Polymer Bulletin*. **2015**, 72, 3169–3182.
155. Daemi, H.; Barikani, M. Synthesis and characterization of calcium alginate nanoparticles, sodium homopolymannuronate salt and its calcium nanoparticles. *Scientia Iranica F.* **2012**, 19, 6, 2023-2028.
156. Sarmento, B.; Ferreira, D.; Veiga, F.; Ribeiro, A. Characterization of insulin-loaded alginate nanoparticles produced by ionotropic pre-gelation through DSC and FTIR studies. *Carbohydrate Polymers*. **2006**, 66, 1-7.
157. Haraguchi, K. Synthesis and properties of soft nanocomposite materials with novel organic/inorganic network structures. *Polymer Journal.* 2011, 43, 223–241.
158. Haraguchi, K.; Takehisa, T. Nanocomposite hydrogels: a unique organic–inorganic network structure with extraordinary mechanical, optical, and swelling/de-swelling properties. *Advanced Materials.* **2002**, 14, 1120–1124.
159. Haraguchi, K.; Li, H. J.; Matsuda, K.; Takehisa, T.; Elliott, E. Mechanism of forming organic/inorganic network structures during *in-situ* free-radical

polymerization in PNIPA-clay nanocomposite hydrogels. *Macromolecules.* **2005**, 38, 3482–3490.
160. Haraguchi, K.; Takehisa, T.; Fan, S. Effects of clay content on the properties of nanocomposite hydrogels composed of poly(*N*-isopropylacrylamide) and clay. *Macromolecules.* **2002***,* 35, 10162–1017.
161. Pongjanyaku, T.; Rongthong, T. Enhanced entrapment efficiency and modulated drug release of alginate beads loaded with drug–clay intercalated complexes as microreservoirs. *Carbohydrate Polymers*. **2010**, 81, 409–419.
162. Parello, M. L.; Rojas, R.; Giacomelli, C. E. Dissolution kinetics and mechanism of Mg–Al layered double hydroxides: A simple approach to describe drug release in acid media. *Journal of Colloid and Interface Science.* 2010, 351, 134–139.
163. Rojas, R.; Jimenez-Kairuz, A. F.; Manzo, R. H.; Giacomellia, C. E. Release kinetics from LDH-drug hybrids: Effect of layers stacking and drug solubility and polarity. *Colloids and Surfaces A: Physicochemical and Engineering Aspects.* **2014**, 463, 37–43.
164. Khan, S. B.; Alamry, K. A.; Alyahyawi, N. A.; Asiri, A. M.; Arshad, M. N.; Marwani, H. M. Nanohybrid Based on Antibiotic Encapsulated Layered Double Hydroxide as a Drug Delivery System. *Applied Biochemistry and Biotechnology.* **2015**, 175, 412–1428.
165. Rojas, R.; Palena, M. C.; Jimenez-Kairuz, A. F.; Manzo, R. H.; Giacomelli, C. E. Modeling drug release from a layered double hydroxide–ibuprofen complex. *Applied Clay Science.* **2012**, 62–63, 15–20.
166. Ambrogi, V.; Perioli, L.; Ciarnelli, V.; Nocchetti, M.; Rossi, C. Effect of gliclazide immobilization into layered double hydroxide on drug release. *European Journal of Pharmaceutics and Biopharmaceutics.* **2009**, 73, 285–291.
167. Ambrogi, V.; Fardella, G.; Grandolini, G.; Perioli, L. Intercalation compounds of hydrotalcite-like anionic clays with antiinflammatory agents — I. Intercalation and *in-vitro* release of ibuprofen. *International Journal of Pharmaceutics*. 2001, 220, 23–32.
168. Depan, D.; Singh, R. P. Preparation and Characterization of Novel Hybrid of Bio-Assisted Mineralized Zn-Al Layered Double Hydroxides Using Chitosan As a Template. *Journal of Applied Polymer Science*. **2010**, 115, 3636–3644.
169. You, J.; Park, S. B.; Park, H. Y.; Haam, S.; Chung, C. H.; Kim, W. S. Preparation Of Regular Sized Ca-Alginate Microspheres Using Membrane Emulsification Method. *Journal of Microencapsulation*. **2001**, 18, 4, 521-532.
170. Lee, W.; Chen. Y. C. Effect of Bentonite on the Physical Properties and Drug-Release Behavior of Poly(AA-co-PEGMEA)/Bentonite Nanocomposite Hydrogels for Mucoadhesive. *Journal of Applied Polymer Science.* **2004**, 91, 2934–2941.

Appendix 1: **Calibration Curves**

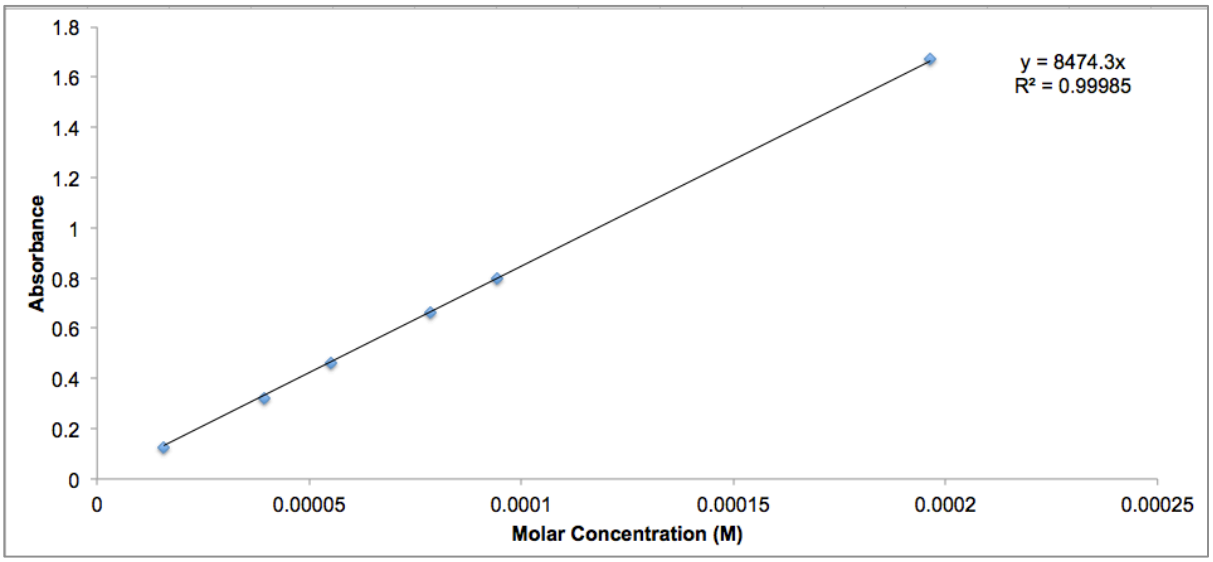

Figure A1- 1. The calibration curve of vitamin B6 standard solutions comprising 2.5 M HCl and phosphate buffer (pH 6.8), for the determination of the loading percentage of B6-LDH (λ_{max} = 290 nm).

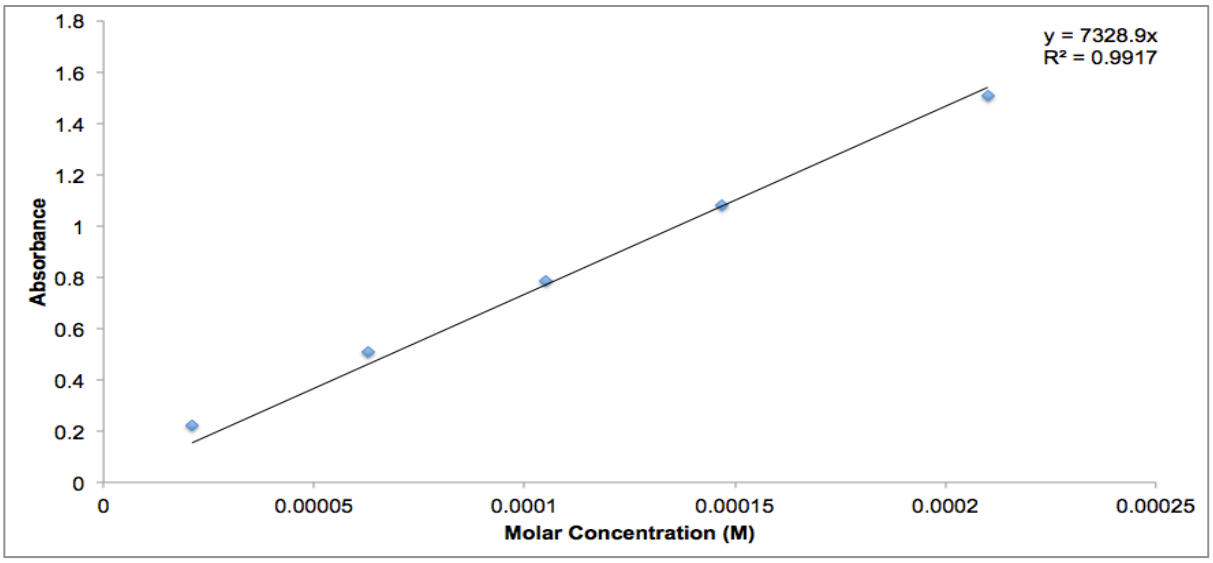

Figure A1- 2. The calibration curve of vitamin B6 in 5% calcium chloride solution (λ_{max} = 307 nm).

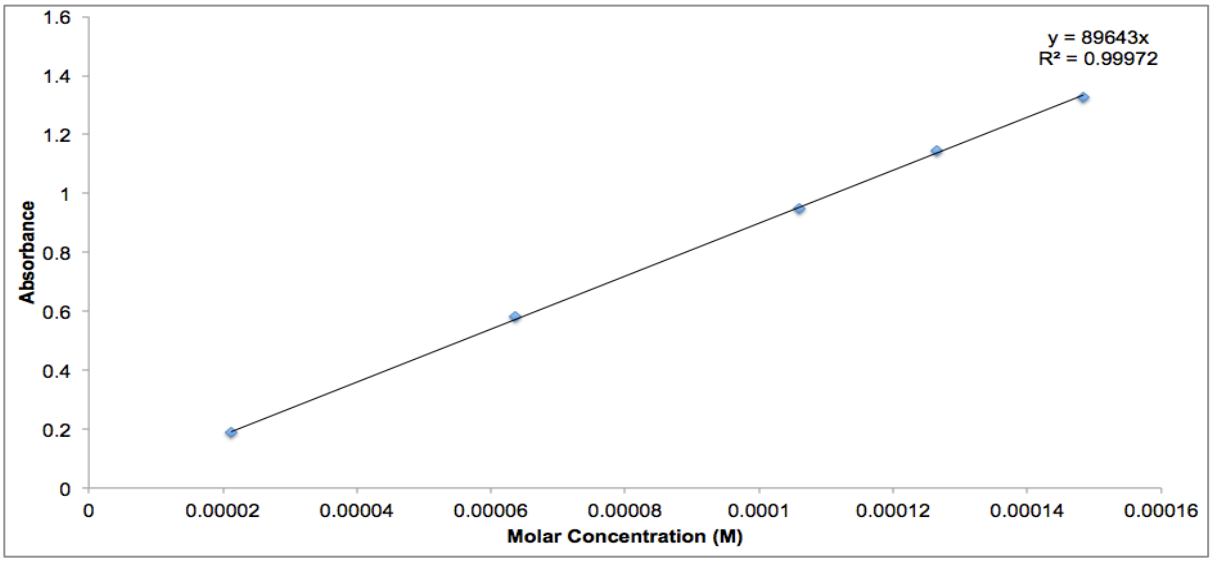

Figure A1- 3. The calibration curve of vitamin B6 in Biorelevant Simulated Gastric Fluid (BioSGF) of pH 1.6 (λ_{max} = 290 nm).

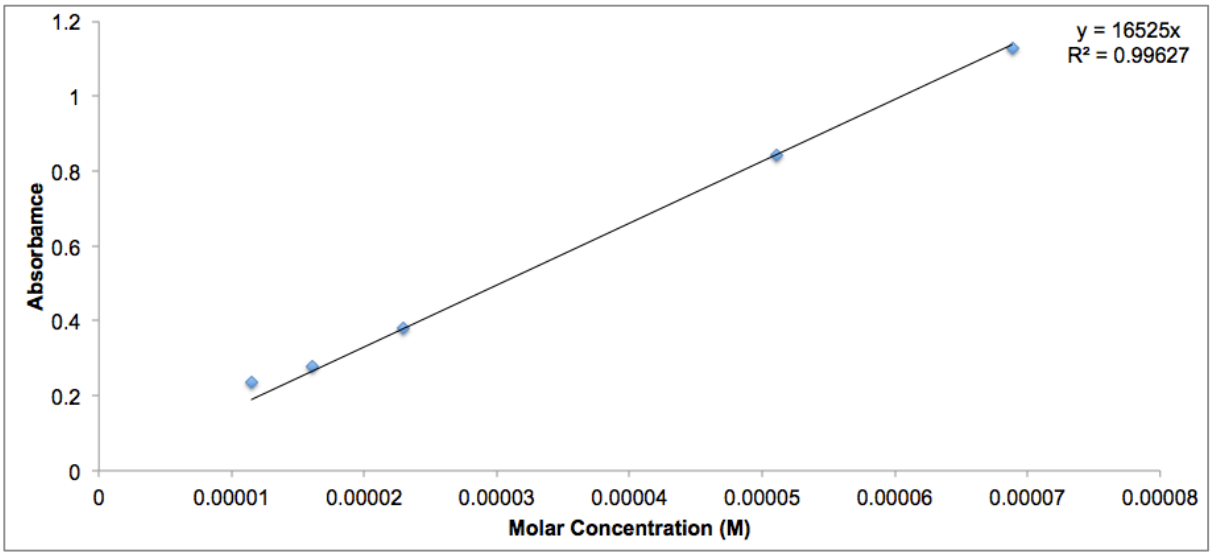

Figure A1- 4. The calibration curve of vitamin B6 in Biorelevant Simulated Intestinal Fluid (BioSIF) of pH 6.5 (λ_{max} = 220 nm).

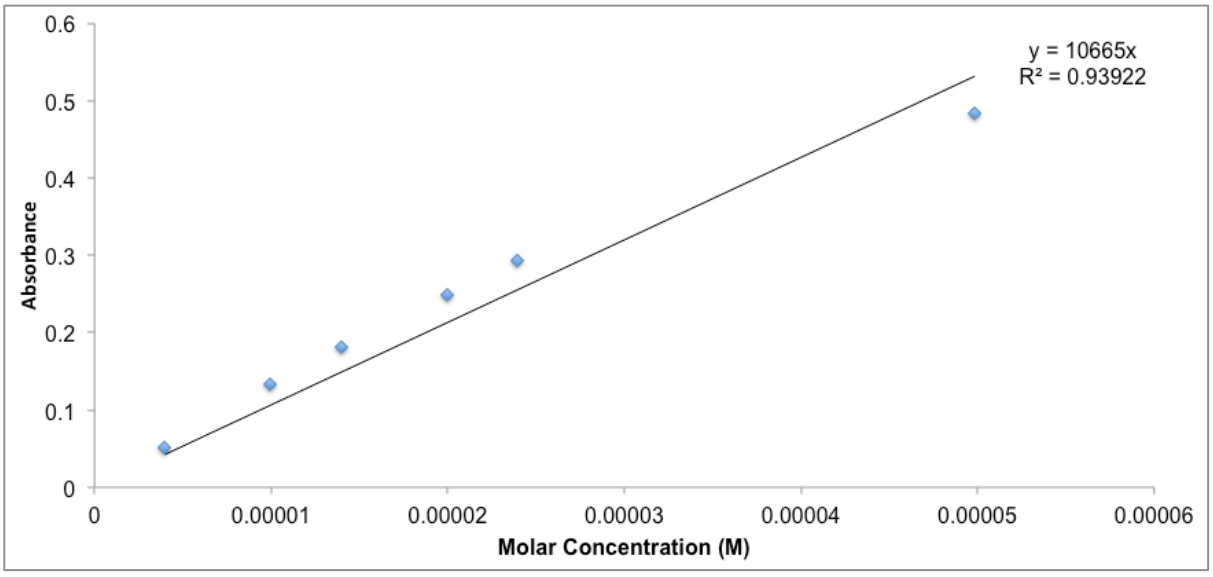

Figure A1- 5. The calibration curve of folic acid standard solutions comprising 2.5 M HCl and phosphate buffer (pH 6.8), for the determination of the loading percentage of Fa-LDH (λ_{max} = 300 nm).

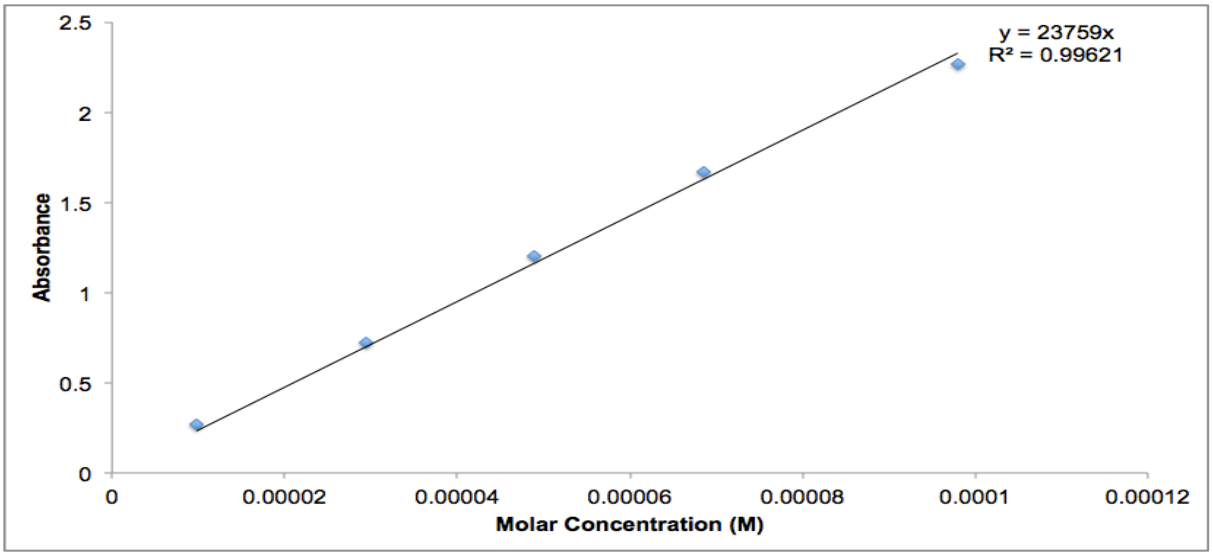

Figure A1- 6. The calibration curve of folic acid in 5% calcium chloride solution (λ_{max} = 256 nm).

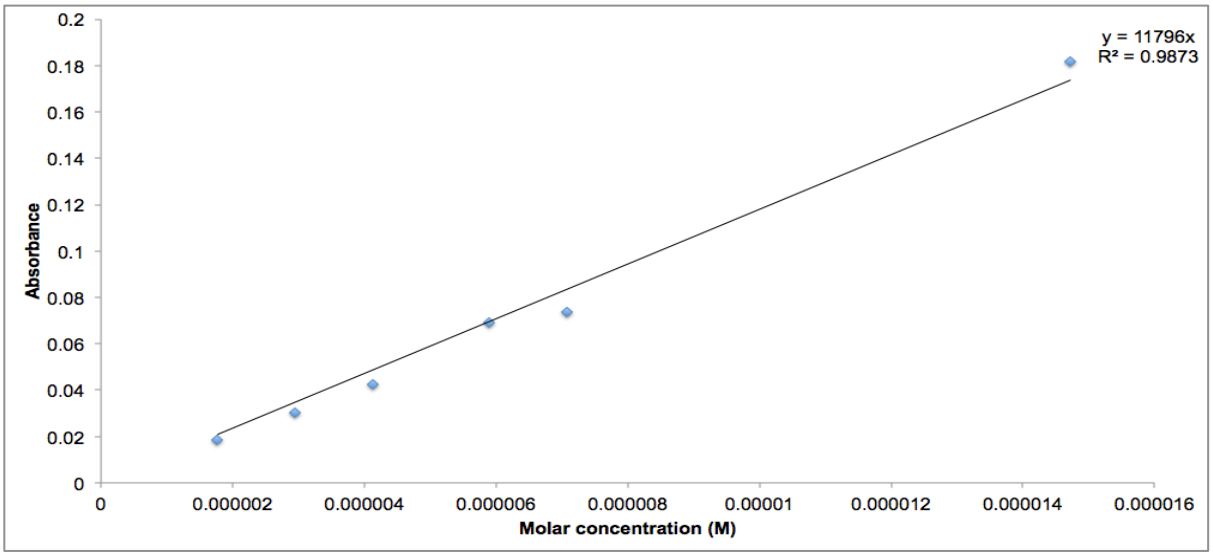

Figure A1- 7. The calibration curve of folic acid in Biorelevant Simulated Gastric Fluid (BioSGF) of pH 1.6 (λ_{max} = 300 nm).

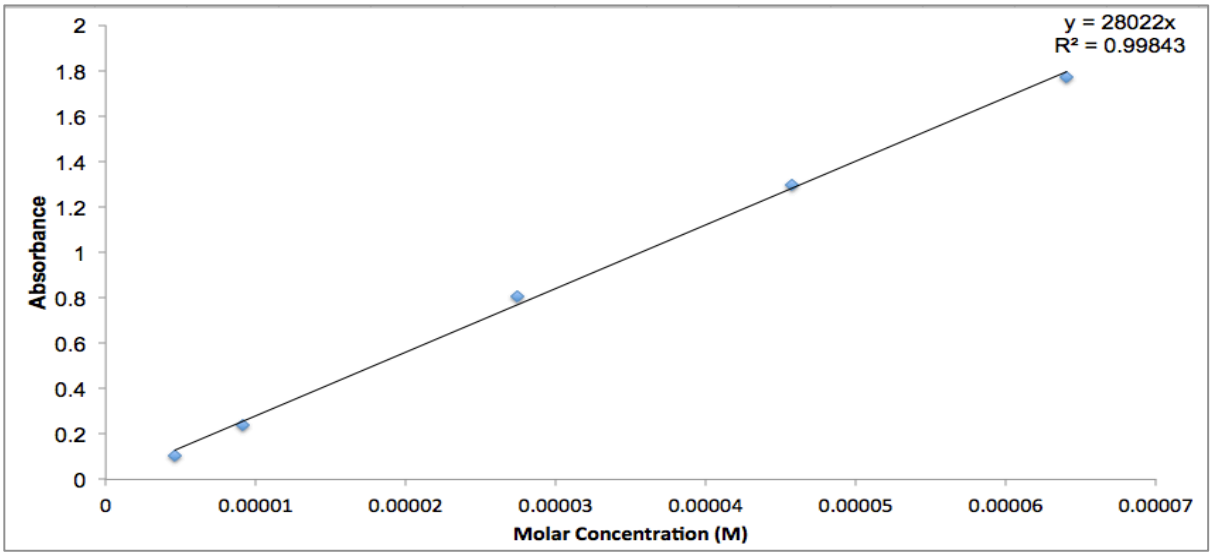

Figure A1- 8. The calibration curve of folic acid in Biorelevant Simulated Intestinal Fluid (BioSIF) of pH 6.5 (λ_{max} = 280 nm)

Appendix 2: The FTIR Spectra of the Vitamin-Loaded Composites

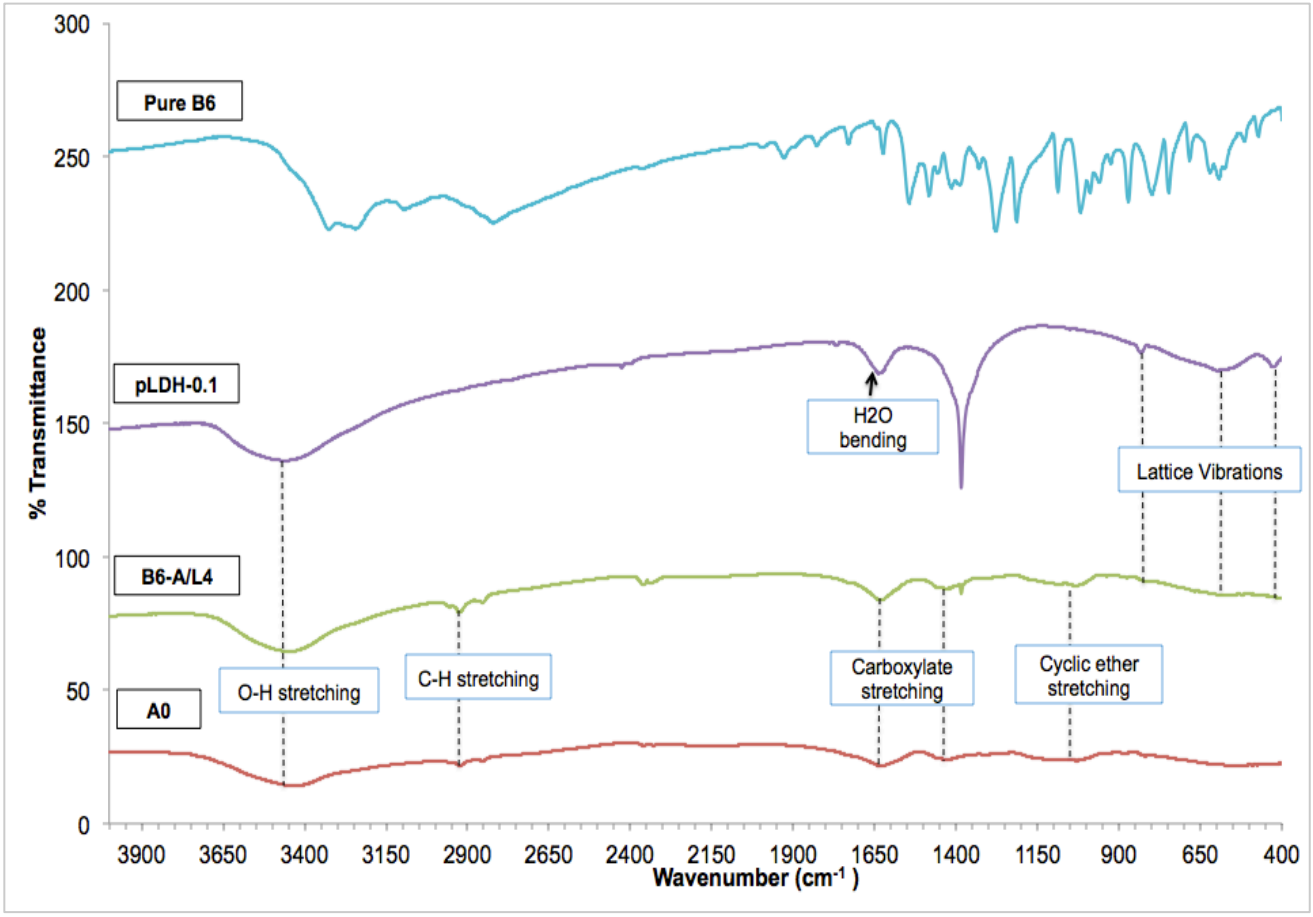

Figure A2-1. FTIR spectra of pure vitamin B6, pristine LDH (pLDH-0.1), B6-loaded composite beads with alginate:LDH ratio of 4:1 (B6-A/L4), and plain calcium alginate beads (A0).

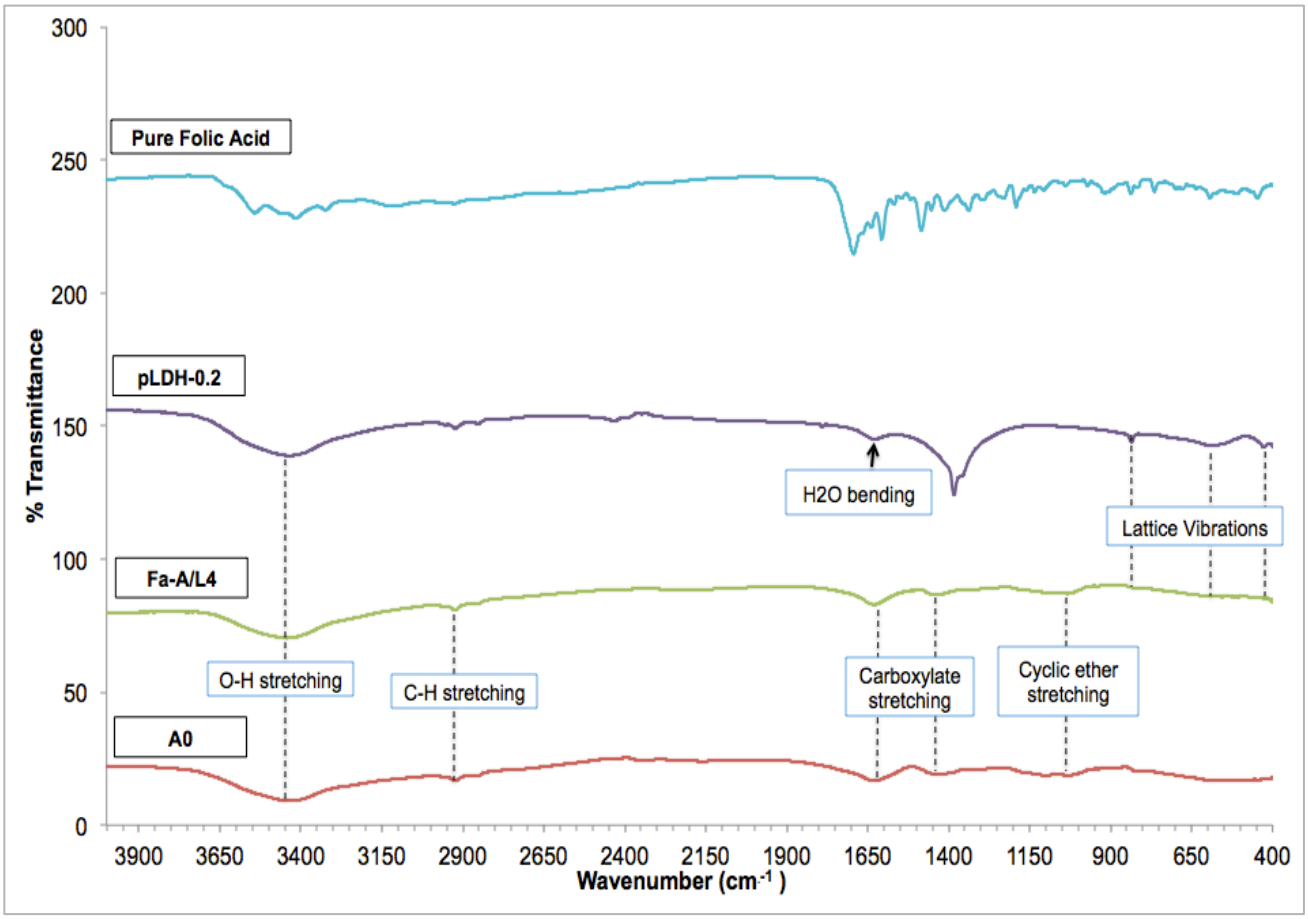

Figure A2-2. FTIR spectra of pure folic acid, pristine LDH (pLDH-0.2), Folic acid-loaded composite beads with alginate:LDH ratio of 4:1 (Fa-A/L4), and plain calcium alginate beads (A0).